State of the art of fuel micro-mechanical modelling: From atomic scale to engineering laws in fuel performance codes

Bruno Michel, Michael Welland, Nana Ofori-Opoku, Laurent Vanbrutzel, Katalin Kulacsy, Michael Tonks, Pierre-Guy Vincent, Fabienne Ribeiro, Andreï Jelea, Giovanni Pastore, et al.

State of the art of fuel micro-mechanical modelling: from atomic scale to engineering laws in fuel performance codes

Bruno Michel[1], Michael Welland[2], Nana Ofori-Opoku[2], Laurent Vanbrutzel[3], Katalin Kulacsy[7], Michael R. Tonks[4], Pierre-Guy Vincent[5], Fabienne Ribeiro[5], Andrei Jelea[5], Giovanni Pastore[6], David A. Anderson[8], Jean-marie Gatt[1], Ronan Madec[9], Jean-Paul Crocombette[10]

[1] Commissariat à l'Energie Atomique et aux Energies Alternatives, DES, IRESNE, DEC, SESC, Cadarache F-13108, Saint-Paul-Lez-Durance, France

[2] Canadian Nuclear Laboratories, Chalk River, ON, K0J 1J0, Canada

[3] Commissariat à l'Energie Atomique et aux Energies Alternatives, DES, ISAS, DPC, SCCME, Université Paris-Saclay, F-91191, Gif-sur-Yvette, France

[4] University of Florida, Gainesville, FL 32611

[5] Institut de Radioprotection et de Sûreté Nucléaire, PSN-RES/SEMIA/LSMA, B.P. 3, Cadarache 13115 Saint-Paul-lez-Durance Cedex, France.

[6] Newcleo S.r.l., Via Galliano 27, 10129 Torino, Italy

[7] Centre for Energy Research, Konkoly-Thege Miklós út 29-33, 1121 Budapest, Hungary

[8] Materials Science and Technology Division, Los Alamos National Laboratory, Los Alamos, NM 87545, USA

[9] CEA, DAM, DIF, F-91297 Arpajon, France
Université Paris-Saclay, CEA, Laboratoire Matière en Conditions Extrêmes, F-91680 Bruyères-le-Châtel, France

[10] Commissariat à l'Energie Atomique et aux Energies Alternatives, DES, ISAS, DMN, SRMP, Université Paris-Saclay, F-91191, Gif-sur-Yvette, France

Abstract

This paper presents the state-of-the-art knowledge about the micro-mechanical modelling of the fuel behavior under irradiation with normal and off normal operating conditions. Modelling of fundamental processes can provide key insights in the behavior of the material. Such models target specific phenomena due to the limits of computational resources and scope of theory, necessitating a multiscale approach. This work follows a multiscale paradigm building up in spatio-temporal scale. The micro-mechanical modelling studied addresses all the loading conditions encountered in the reactor with elasticity, plasticity, creep and fracture behavior.

Atomistic-scale modelling review reveals mechanisms and physical parameters for elasticity of fresh and irradiated fuel, rupture, dislocation gliding and internal stresses induced by pressurized bubble with fission gases. Simulation techniques proposed at this scale are Density Functional Theory, Molecular Dynamic with empirical potential, Dislocation Dynamics and Phase Field Crystal methodology.

At a higher scale, micro-mechanical models are available for the viscoplastic behavior of the material as a continuum from a single crystal to polycrystal systems and the interplay with irradiation and porosity. Crystal plasticity models, homogenisation techniques and FE or FFT full field mechanical simulations give a complete set of tools to achieve the upscaling process from the basic properties up to the engineering mechanical law needed in the fuel performance code.

This multi-scale modelling can also address the questions related to fuel rupture properties in order to provide physical basis to the empirical description of the fuel fragmentation process under different types of loading conditions. For this, low scale experiments coupled with micro-mechanical modelling are the keys for the multi-scale characterization of the input parameters of smeared crack models used in fuel performance codes.

Acronym list

AFM	Atomic Force Microscope
CRSS	Critical Resolved Shear Stress
DD	Dislocation Dynamics method
DFT	Density Functional Theory
DFT+U	Density Functional Theory (***DFT***), adding a Hubbard ***U*** correction
DPC	Displacement Per Cation
EBSD	Electron Back Scattered Diffraction
FE or **FEM**	Finite Element Method
FFT	Fast Fourier Transform
FGR	Fission Gas Release
GGA	Generalized Gradient Approximation
GND	Geometrical Necessary Dislocation
GTN	Gurson-Tvergaard-Needleman model
HBS	High-Burnup Structure
HRTEM	High-Resolution Transmission Electron Microscopy
HSE	Heyd-Scuseria-Ernzerhof hybrid functional
LDA	Local density Approximation
LHR	Linear Heat Rate
LOCA	Loss-Of-Coolant Accident
LWR	Light-Water Reactors
MD	Molecular Dynamics method
MOOSE	Multiphysics Object-Oriented Simulation Environnement
MOX	Mixed Oxide fuel, usually referring to mixture of PuO_2 and UO_2
PBEO	Perdew-Burke-Ernzerhof hybrid functional
PCMI	Pellet-Cladding Mechanical Interaction
PF	Phase Field model
PFC	Phase Field Crystal model
RIA	Reactivity Insertion Accident
SEM	Scanning Electron Microscopy
SMTB-Q	Second-Moment Tight-Binding - Charge Equilibration
SQS	Special Quasi-random Structure
XRD	X-ray powder Diffraction

1 Introduction

Most present-day light-water reactors (LWRs) use fuel pins that consist of a hermetically sealed tube of some zirconium alloy filled with cylindrical UO_2 pellets. The pellets are produced by pressing and sintering and have a granular structure with typical grain sizes of a few tens of microns. Most of a fuel pin's service time is spent in approximately steady-state operation conditions with periods when the power changes due to start-up or load follow (Condition I). During this time, the fuel pellet typically densifies as the as-fabricated porosity is partly removed by an early in-reactor re-sintering process and swells as fission products accumulate in it. Since about 30% of fission products are noble gases, which are practically insoluble in the solid matrix, these segregate in spherical-shaped intra-granular and lenticular-shaped inter-granular bubbles, building up pressure in these bubbles and contributing significantly to swelling. A minor part of the gases finds its way to the pin free volume, increasing the internal pressure of the pin. While swelling proceeds, the cladding creeps down due to the overpressure exerted onto it by the coolant, until it comes into contact with the fuel pellet and pellet-cladding mechanical interaction (PCMI) is established. From then onwards the contact pressure between the swelling pellet and the cladding causes a gradual outward creep of the cladding. In addition to all these processes, the periphery of the fuel pellets re-crystallises at high-burnup into the high-burnup structure (HBS), consisting of small, sub-micron-sized grains, with fission gases gathered into micron-sized, over-pressurised intergranular pores. The processes being slow and smooth from the mechanical point of view, the fuel pellet mainly experiences elastic deformation with fragile rupture at begin of life and a slow stress relaxation process induced by a-thermal irradiation creep with possibly some thermal creep at high ratings.

During anticipated operational occurrences (Condition II) the rating may change rather fast, e.g. it can increase in a situation when PCMI is already established. In such a case, the thermal expansion of the fuel being higher than that of the cladding, consequently the contact pressure increases and leads to tensile stresses in the cladding. The maximal stress reached in the cladding during the power transient will depend on the creep behavior of the cladding, with a stress relaxation process under strain-controlled loading, but also on the thermal creep of the pellet with an accommodation process of the fuel volume expansion.

Design basis accidents (Conditions III-IV) typically taken into consideration are loss-of-coolant accident (LOCA) and reactivity insertion accident (RIA), both of which cause a fast rise in temperature in different parts of the fuel pellets. Increasing gas pressure in the fission gas bubbles may then cause crack initiation and lead to increased gas release or even to the fragmentation of the pellet. Indeed, experimental evidence suggests that gas venting from the grain boundaries may also occur – even in the presence of a population of predominantly isolated gas bubbles – by a mechanism of grain boundary separation due to microcracking. This is also true for Conditions II and III events as shown mainly for Condition II in (Carroll et al. 1969, Hastings et al. 1986, Walker et al. 1988). Such contribution is thought to be responsible for the high FGR observed in transient tests, which is characterized by a rapid kinetics (burst release) that cannot be explained as purely diffusion-controlled (Rothwell 1962, Notley and MacEwan 1966, Carroll et al. 1969, Hastings et al. 1986, Une and Kashibe 1990, Nakamura et al. 1999). However, the current knowledge of the relevant physical processes is limited and accordingly, empirical models of burst release are used (Hering 1982, Koo et al. 1999, Van Uffelen et al. 2008, Barani et al. 2017). Obtaining an improved understanding of the grain boundary separation micromechanics is essential for physics-based modelling of FGR during transients.

If the cladding fails, the hot fuel fragments may be dispersed in the primary coolant vaporizing the coolant and causing pressure pulses in the primary circuit. The fracture properties of the fuel are therefore of paramount importance in the process. The impact of the pellet fragmentation on fuel relocation and ejection under a LOCA is discussed in international research programs and is included in safety approach for some countries. Safety criteria for RIA vary. In some countries, an empirical fuel enthalpy limit is prescribed to avoid pellet fragmentation, which is difficult to formulate for high-burnup fuel due to the dependence of the amount of the gas in bubbles on power history. Some countries prescribe that cladding integrity be maintained, therefore fuel plastic deformation also plays an important role in the process, as it decreases cladding hoop stress.

This paper aims to present the state-of-the-art knowledge about the micro-mechanical modelling of the above-mentioned processes: elastic, plastic and creep deformation of the fuel on one hand and fracture properties on the other hand. It adds to existing reviews of multi-scale modeling of nuclear fuel (Stan 2009, Veschunov 2015, Tonks 2017) or of materials in general (Becquart 2019) by investigating the micro-mechanical fuel performance. It covers all length scales in some detail, whereas existing reviews are either more general and does not explore micro-mechanics in the depth aimed for in this review or primarily targets other fuel performance properties, such as fission gas evolution and thermal conductivity.

Modelling of fundamental processes can provide key insights into the behavior of the material. Such models target specific phenomena due to the limits of computational resources and scope of theory, necessitating a multiscale approach. This work proposes a first global picture for the methods and physical data enabling this multiscale description. Sec. 2 discusses atomistic-scale modelling and reveals mechanisms at their most basic level which may be common to both viscoplastic behavior and fracture. Sec 3 describes the viscoplastic behavior of the material as a continuum from a single crystal to polycrystal systems and the interplay with irradiation and porosity. Sec. 4 considers fracture by first establishing the event criteria then discussing the effects of intergranular bubbles focussing elastic stresses, forming fracture pathways and finally the macroscale behavior.

2 Lower-length-scale modelling

The main idea developed in this section is to have a multi-scale micro-mechanical model with physically based material parameters, themselves derived from small scales simulation. The objective is not to avoid experiments, but to proposed advanced simulation tools in order to have a complete understanding of each intrinsic physical parameter. One general question to address regarding the computation of physical properties with low-length-scale simulation approaches, ordered in this paper by length scales, concerns the time scale evolution. For micromechanics of fuel the main time-scales to consider are related to the physics underlying elastic or inelastic strains accommodation mechanisms. The mechanical properties discussed in this paper can be separated in three types of behavior with elasticity, rupture and viscoplasticity. For fuel mechanical evaluation, there are significant strain rate effects only for viscoplasticity. It means that the question of time scale is not an issue for elasticity or rupture, but has to be considered for the mechanisms controlling dislocation mobility leading to creep strains. The characteristic time scales for dislocation gliding, addressed in this paper, depends on the temperature and stress. The range is very large with quasi instantaneous gliding at low temperature or high stress level ([1.e2 , 1.e3] m/s), or very slow mobility under intermediate temperatures and low stress level ([1.e-6 , 1.e-1] m/s).

For molecular dynamics simulations using empirical potentials, the reliability of the results depends strongly on the accuracy of these interatomic potentials. Concerning mechanical properties of UO_2 and MOX several assessments have been published (Cooper 2014, Balboa 2017). The results presented herein either use the most reliable potential up-to-date for the studied properties or consider comparison of several potentials in their study.

The section starts first with un-irradiated fuel with crystal elastic constant in 2.1, rupture properties in 2.2 and physical parameters controlling viscoplastic behavior induced by dislocation gliding in 2.3. Then irradiated fuel is considered in section 2.4 with a quantitative assessment of the density of some irradiation defect in service and the corresponding evolution of the elastic properties. In section 2.5 the mechanical characteristics of the pressurized bubbles induced by gaseous fission products are addressed. Finally, the section 2.6 is not directly focused on some specific physical properties but proposes a new modelling formalism to enable a more direct scale transfer between the atomic scale and the continuum scale discussed in sections 3 and 4 for viscoplasticity and rupture respectively.

2.1 Single crystal elastic properties (DFT)

Atomic scale simulation techniques based on density functional theory (DFT) have been used to calculate elastic constants of UO_2, but, due to computation cost and the structural complexity of dislcoations, grain bouanderies and fracture surfaces, they have not been and are not envisioned to be directly applied to any of the more complex mechanical properties or processes. Instead, the main role of DFT within micro-mechanical fuel modelling is to provide data on elastic constants and properties related to thermodynamics and diffusion to longer length and time scale methods within a multi-scale simulation framework. In particular, the elastic constants of pristine UO_2 have been extensively studied by density functional theory (DFT) calculations, see Table 1 and references therein. The simplest measure of the elastic properties is the bulk modulus of the crystal, which is typically calculated by fitting an appropriate equation of state to data points obtained by isotropic expansion and contraction of the UO_2 unit cell at 0 K. These results are often compared to experimental data taken around room temperature. In early studies exploring various DFT exchange-correlation functionals for UO_2, such as the local density approximation (LDA), the generalized gradient approximation (GGA), LDA or GGA with an added Hubbard U term (DFT+U) and hybrids, comparison of the predicted bulk modulus to available experimental data served as a measure of the accuracy of the computational methodology. The DFT+U and hybrid approaches are invoked to better describe the strongly correlated U 5f electrons, which results in the correct insulating band structure, as opposed to the metallic character predicted by standard LDA or GGA. The improved description of the correlated electrons also impacts bonding and refines the accuracy of the predicted bulk modulus. Table 1 shows that predictions of the bulk modulus available in the literature roughly fall within a 10% range of experimental data points, except for standard LDA calculations, which deviate by almost 20% from experimental data. LDA based calculations tend to overpredict the bulk modulus, while GGA attempts to correct this issue and for UO_2 that leads to a slight underestimation of the bulk modulus. Addition of a Hubbard U term to LDA or GGA tends to slightly reduce the bulk modulus, which retains or somewhat increases the underestimation of the bulk modulus for GGA based calculations, while the predictions are improved and agree very well with experimental data for LDA based Hubbard U calculations. The GGA+U calculations due to Dorado et al. (Dorado 2009, Dorado 2013) deviate from the general trend described above by predicting the bulk modulus to be slightly higher than the experimental data. This deviation may be caused by the challenge of avoiding meta-stable electronic

states in UO_2 described by hybrids and the Hubbard U methodology (Dorado 2009). Dorado et al. (Dorado 2009, Dorado 2013) carefully addressed this issue, but other studies may either have ignored this issue or used a different methodology to control it. Available hybrid calculations based on the HSE (Heyd 2003) and PBE0 (Carlo 1999) formulations provide very accurate predictions of the bulk modulus. Keeping the spread in values discussed above in mind, the best results for the bulk modulus are obtained for GGA+U in the paramagnetic state (Dorado 2013), and for hybrid calculations.

	B (GPa)	C_{11} (GPa)	C_{12} (GPa)	C_{44} (GPa)
Experimental data				
(Idiri 2004)	207			
(Fritz 1976)	208.9	389.3	118.7	59.7
(Benedict 1986)	207			
(Wachtman 1965)	213	396	121	64
Computational data GGA+U				
(Yu 2009)	195.4			
(Geng 2007)	180.68			
(Sanati 2011)	192.2	345.7	115.5	63.4
(Dorado 2013) (AFM)	222	401	132	94
(Dorado 2013) (FM)	227	409	136	96
(Dorado 2013)(PM)	212	385	125	68
(Thompson 2011)	188			
(Gupta 2007)	209			
(Dorado 2009)	187			
(Vazhappilly 2020)	199.6	378.3	110.3	63.7
(Thompson 2014)	188			
(Devey 2011)	197			
(Tian 2012)	192			
Computational data GGA				
(Geng 2007)	203.53			
(Freyss 2015)	194			
(Sanati 2011)	198.8	367.0	114.7	62.9
(Thompson 2011)	188			
(Gupta 2007)	188			
Computational data LDA+U				
(Geng 2007)	208.32			
(Dudarev 1998)	173			
(Wang 2013)	222.4	389.3	138.9	71.3
(Wang 2013) (SO)		395.9	134.0	89.5
(Sanati 2011)	220.6	380.9	140.4	63.2
(Sanati 2011) (SO)	220.3	419.1	120.9	62.0
(Andersson 2009)	218			
(Gryaznov 2009)	196			
Computational data LDA				
(Geng 2007)	239.99			

(Crocombette 2001)	252			
(Sanati 2011)	240.3	432.5	144.2	85.2
Hybrids				
(Prodan 2006) (PBE0)	219			
(Prodan 2006) (HSE)	218			
(Jollet 2009) (PBE0)	199			
Others				
(Petit 2010) (SIC)	219			

Table 1: Experimental and DFT calculated values for the bulk modulus and elastic constants (given in Voigt's notation) of UO_2. The calculated values are grouped based on the computational methodology (GGA+U, GGA, LDA+U, LDA, hybrids and other methods (SIC, self-interaction-correction)). Most calculations used an AFM ordering of magnetic moments. In cases where other or multiple orderings were investigated, this is indicated by the corresponding acronyms. Similarly, most calculations do not include spin-orbit coupling, but cases that do are labelled by the SO acronym. Finally, the hybrid calculations include two sub-methods denoted by the corresponding acronyms.

The full elastic response of UO_2 is described by the elasticity tensor, which for a cubic material like UO_2 reduces to C_{11}, C_{12} and C_{44}. The elastic constants are typically calculated by slightly transforming the unit cell and mapping the energy of the distorted cell onto a constitutive equation that expresses the resulting change in energy or stress in terms of the elastic constants. At high temperature UO_2 is a paramagnet and below about 31 K it is a non-colinear antiferromagnet (AFM) (Frazer 1966). However, most DFT studies assume a simple AFM arrangement with the spins aligned on (110) planes to approximate the more complex non-colinear arrangement, which is also assumed to represent the high-temperature paramagnetic state. The (110) AFM assumption implies that the cubic symmetry, observed in experiments for both the low and high-temperature cases, is broken in the calculations. Despite this fact, most studies only report the three cubic elastic constants. DFT calculated elastic constants from the literature are compared to available experimental data in Table 1. The performance of the different computational approaches, as compared to experimental data, follows the same trends as for the bulk modulus. Both LDA+U and GGA+U calculations capture the elastic properties well. Despite that the full elasticity tensor has not been calculated based on any hybrid functional, it is expected that the accurate prediction of the bulk modulus is extended to the remaining elastic constants as well. Engineering analysis sometimes uses elastic moduli such as the shear modulus, Poisson ratio and Young's modulus. These may be derived from C_{11}, C_{12} and C_{44} and will not be further discussed here.

The review above established that the single crystal elastic properties of fresh UO_2 are captured reasonably well by several DFT methodologies, in particular those accounting for strong correlations of U 5f electrons. With GGA+U and hybrid functionals at the top of ranking, though, there is a spread between calculations using nominally the same approach that should be be kept in mind in the context of this conclusion. However, there are limited applications beyond this basic reference case. As an example of existing studies in this area, (Dorado, 2013) investigated the change in bulk modulus as function of the PuO_2 content in mixed oxide fuels (MOX). This study used the special quasi-random structures (SQS) to describe the mixture of UO_2 and PuO_2 and calculated the bulk modulus as function of composition. The results suggested an almost linear dependence of the bulk modulus between the two end points. A similar approach was used in the same study to model the paramagnetic spin state of UO_2 (Dorado 2013), which is relevant for high temperature applications. The bulk modulus and elastic constants were slightly

reduced in the paramagnetic state compared to the AFM state typically assumed in DFT studies. The impact of chemistry was also investigated for UO_2 doped with La and Dy in Ref. (Vazhappilly 2020), again showing a close to linear relation of the bulk modulus between the two endpoints.

The bulk modulus of UO_2 is known to have a significant temperature dependence, with a softening at high temperatures (Hutchings 1987). The 0 K predictions obtained from DFT calculations can safely be extrapolated to room temperature, which enables the comparison to experimental data in Table 1.

In summary, DFT calculations have been shown to accurately reproduce the elastic constants of UO_2 as compared to room temperature experimental data. The best agreement with experiments is obtained by methods that are designed to capture the strongly correlated nature of the U 5f electrons, with GGA+U in the paramagnetic state (Dorado 2013) and hybrid functionals (Prodan 2006, Jollet 2009) providing the best accuracy. The next step would be to use the same methods to start exploring the impact of changes in composition, defect concentration, temperature, etc., all of which could improve nuclear fuel performance predictions by informing constitutive models at the single crystal level. For example, the impact of chemistry, point defects, fission gases and temperature has received none or very limited attention from the DFT community, which is, of course, a consequence of the high computational expense associated with those studies. These cases are highly relevant for nuclear fuel performance and future DFT studies could contribute to improved models for the elastic response at the single crystal level by incorporating the impact of some of the variables mentioned above. Concerning the high-temperature softening of elastic properties, it has only been investigated using semi-empirical potentials (Cooper 2014). UO_2 is also known to exhibit a complex temperature dependence of the elastic constants at low temperature (Brandt 1968), with the elastic constants softening and even diverging as the Néel temperature is approached. This is related to the complex electronic and magnetic structure of UO_2. This behavior is not yet fully understood and, certainly, there has been no attempt to capture it by DFT calculations.

2.2 Intra- and inter-granular rupture properties

Nuclear fuels in water nuclear reactors undergo high temperature and radiation, which occasion the formation of a large variety of defects and fission gas accumulation. Subsequently, these defects will cause high local stresses, which alter the thermo-physical properties of the fuel and can induce crack initiation. Therefore, to ensure the stability and the durability of the nuclear reactor core, a solid knowledge of the mechanical properties of the fuel is needed.

Since most of this defect creation occurs at the atomic scale, simulations at that length scale can bring a complementary insight on the mechanisms involve in fracture behavior. Among all the methods available, molecular dynamics (MD) simulation using empirical potentials has been the most used to model crack initiation and propagation at the atomic scale. This method computes the trajectory of each particle of a system large enough to embrace the process zone at a crack-tip and allows the exact description of the plastic deformation such as dislocation, dislocation interaction with defects, cavity formation, etc.

To date, all the MD simulations investigating fracture behavior in UO_2 or $(U,Pu)O_2$ single or polycrystal were carried out using uniaxial tensile loading techniques. This method consists of applying a uniform extension along one axis with a constant strain rate while stress relaxation is applied onto the two other axis. This method is equivalent to a uniaxial tensile stress loading since during the simulation only one

component of the stress tensor is non-zero and the other components fluctuate around zero with a negligible amplitude. During these simulations, the stress-strain curves are calculated and the time evolution of the structural configuration are recorded to follow crack initiation and propagation.

In bulk UO_2, Zhang et al. (Zhang 2012) and Fossati et al. (Fossati 2013) observed that prior to crack propagation, a phase transition occurs at the crack-tip from fluorite structure (space group $Fm\bar{3}m$) to either a PbO_2 scrutinyite-like structure (space group $Pbcn$) or a rutile-like structure (space group P_{42}/mnm) according to the crystallographic direction of the uniaxial loading. Subsequently, crack propagates at the incoherent interface between both structures. An illustration of this propagation behavior is depicted in Figure 1. As the crack advances, new surfaces are created and stress is released, which leads to a reverse phase transformation into the fluorite structure. This metastable transition renders the experimental observation of this behavior impossible to observe. Nevertheless, DFT calculations shows that stress-induced phase transformation exists in UO_2 (Desai 2009, Zhang, 2012, Fossati 2013, Tian 2019).

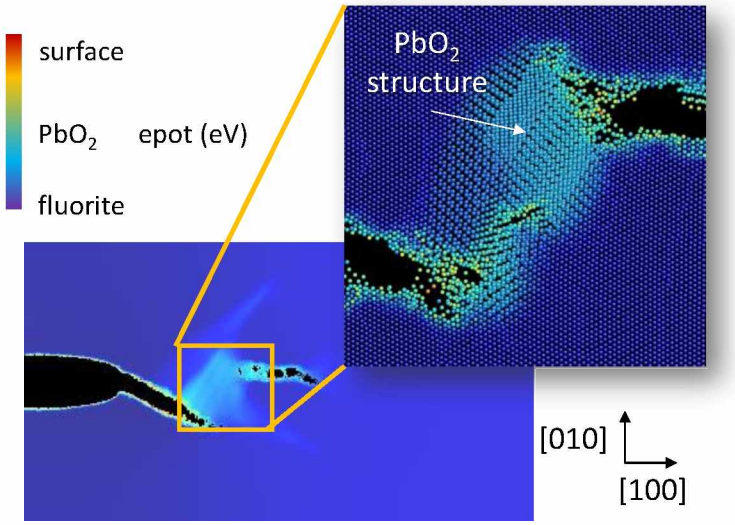

Figure 1: Crack propagation simulation snapshot showing a local phase transition ahead of the crack front. The loading is a uniaxial tensile strain applied along the [010] axis. The atoms are colour coded according to their potential energy. The secondary phase (PbO_2 structure) is denoted by light blue, whereas the bulk structure (fluorite) is in dark blue, and the atoms at the crack surface are in orange/red. The encapsulated picture on the right is a zoom of the area including both fluorite structure and secondary phase. The printed axes show the crystallographic directions in the initial fluorite structure.

However, Balboa et al. (Balboa 2017) show in $(U,Pu)O_2$ solid solution that this crack propagation behavior is greatly dependent on the empirical potential used. In their simulations they assessed three empirical potentials and observed that for one of them, crack under tensile loading along the [111] crystallographic direction propagates simply with a cleavage-like behavior; it opens straight with steady velocity into the fluorite structure. Conversely, with the two other empirical potentials, phase transition is observed prior to crack propagation as displayed in Figure *2*.

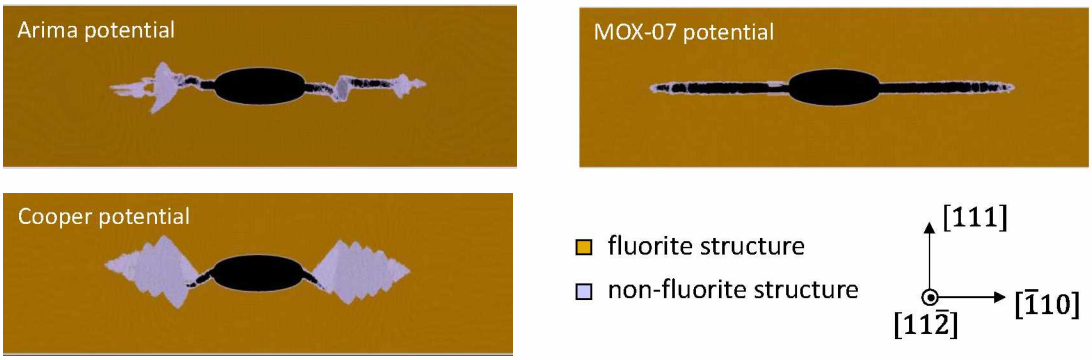

Figure 2: Snapshots during crack propagation in (U,Pu)O_2 system with 25 at.% of plutonium at 300 K simulated with Arima (Arima 2005), Cooper (Cooper 2014), and MOX-07 (Potashnikov 2011) potentials. The tensile load is applied along the [111] crystallographic direction in the fluorite structure. The atoms coloured in gold correspond to the initial fluorite-structure and the atoms coloured in grey correspond to the PbO_2 scrutinyite-like structure.

In polycrystal UO_2, first simulations by Desai et al. (Desai 2008, Millett 2008, Desai 2009) also show phase transformation before nanocrack formation along the grain boundaries, which ultimately results in intergranular fracture. MD simulations of the propagation of pre-existing nanocrack along a grain boundary also display phase transformation ahead of the crack front (Zhang 2013). More recently, Tian et al. (Tian 2019) demonstrated that this behavior, like in the bulk (U,Pu)O_2, depends on the empirical potential used. With more accurate empirical potential fitted on DFT calculations reproducing the transition pressures between the different phases better, they found brittle intergranular fracture without phase transformation in polycrystalline UO_2 under tensile loading.

Furthermore, MD simulations of grain boundary decohesion have been carried out by Bourasseau et al. (Bourasseau 2019) on several symmetrical tilt grain boundaries. They show that the cleavage energy decreases as the misorientation angle between the two grain boundaries increases.

All these studies show that if phase transition can theoretically appear in UO_2, it also occurs for a transition pressure that could be higher than the critical stress required for the crack to initiate or propagate. It is therefore crucial to choose empirical potentials that can reproduce best this thermodynamics property to study mechanical behavior. Furthermore, only uniaxial loading resulting to only one strain or stress state has been investigated to date. Simulations with multiaxial loading could in the future bring broader knowledge of the fuel crack initiation and propagation.

2.3 Material parameter of the dislocation gliding law in UO_2

2.3.1 Thermally activated dislocation glide mobility with atomistic simulation

Plasticity of UO_2 at the atomic scale was studied with a variable load empirical potential (SMTB-Q (Sattonnay 2013)), which is a good compromise between computation time and adaptability to locally non-stoichiometric environments. Experimentally, plasticity in UO_2 is induced by the gliding of dislocations with Burgers vector b=½<110> in {100} crystallographic planes.

<u>Dislocation core structures</u>

The structure and energy of generalized stacking faults was first studied. Stacking faults is introduced in simulation by adding to the vector of the box perpendicular to the stacking plane a component in this plane. The added fault energy as a function of the fault vector is shown in Figure *3* for the {100} plane (γ surface). Only one minimum energy (stable fault) is observed on the fault surface for a displacement of ½<100> (1.23 J/m²), too high for a possible dissociation. No stable fault is observed in planes {110} and {111}.

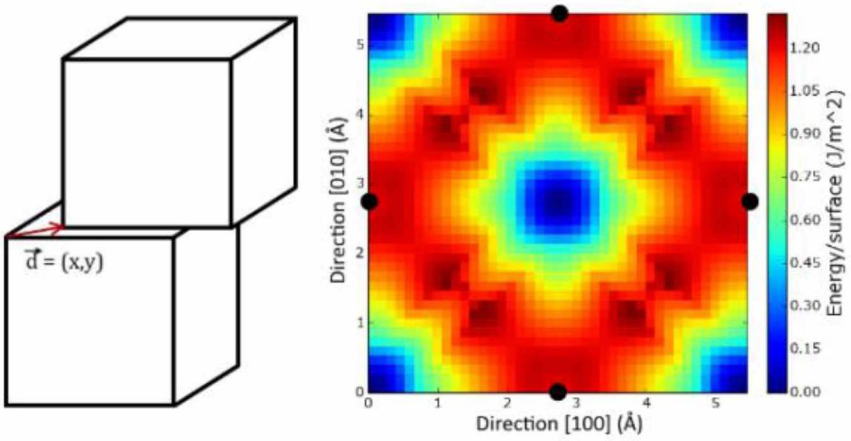

Figure 3: Sketch of a stacking fault (left) and generalized stacking fault energy {100 (right)}. The black point is the identified stable fault.

The energies of a few points on the 3 surfaces γ are shown in Table *2* and compared to those obtained with the Morelon potential (fixed charges potential (Morelon 2003)). In both cases the minimum fault energy which an unstable saddle neck point, is observed for an shift of ¼<110>{100}.

	SMTB-Q	Morelon
¼<110>{100}	**1.20**	**0.76**
½<100>{100}	1.23	0.89
¼<110>{110}	1.49	1.32
½<100>{110}	2.54	1.66
¼<110>{111}	2.35	0.85
⅙<211>{111}	2.20	0.96

Table 2: Energies of generalized stacking faults in UO_2 (J/m²).

In a second step, screw and edge dislocation dipoles gliding in the {100}, {110} and {111} planes with the same Burgers vector ½<110> were created and the core structures were stabilized in molecular dynamics at 1000 K for 20 ps under tri-periodic conditions. The line energies were calculated by integrating the energy on a cylinder around the dislocation and adjusted with the following model (no interaction between dislocations):

$$E(r) = E^{core} + \frac{\mu b^2}{4\pi} ln\left(\frac{r}{r_c}\right)$$

where E^{core}, the linear energy of the dislocation core, which depends on the choice of cut-off radius r_c (r_c = 4 nm here) is the only fitted parameter. b is the norm of the Burgers vector of the dislocation and μ

the shear modulus (depending on the dislocation). Table *3* shows the dislocation core energies compared to those calculated with the Morelon potential.

r_c= 4 nm	SMTB-Q	Morelon
½<110>{100}	3.90	3.94
½<110>{110}	4.46	4.34
½<110>{111}	4.40	4.00
½<110>vis	3.84	3.10

Table 3: Energies of dislocation cores in UO_2 (nJ/m).

The order of the core energies is the same for both potentials and corroborates the experimental results (observation of edge or mixed dislocations gliding according to {100}). But the core structures are different. For example, screw cores show an alternating displacement of oxygen atoms in the same atomic column (Figure *4* left), as well as an alternating charge of uranium atoms (Figure *4* right). The periodicity of the crystal in the direction of the line is then doubled in the core which is a quite uncommon feature.

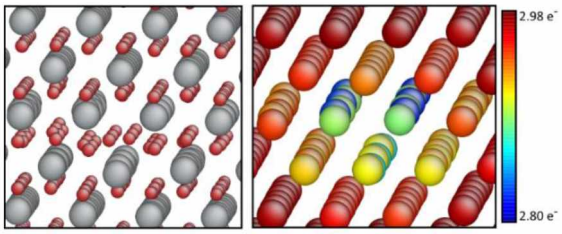

Figure 4: Structure of the core of a screw dislocation (left : oxygen and uranium atoms are in red and grey respectively; right : charge of uranium atoms.

<u>Shear displacements of straight dislocations and pairs of kinks</u>

Shear calculations were performed with boxes containing a straight dislocation in molecular statics. The induced shears are projected on the {100}, {110} and {111} planes for edge and screw dislocations of these three families of slip planes. The deformations were performed with a 0.1% increment and relaxations are made between each increment. These calculations show that the dislocations glide in the {100} plane at a critical stress of 1.4 GPa for the screw component and 3.9 GPa for the edge component. In addition, the screw dislocations glide with oxygen deficiency, meaning that an oxygen atom is left behind when the dislocation starts to move. In the other planes, no slip is observed for the edge dislocations and the critical stresses remain higher for the screws. Thus, the main gliding plane is {100}, and this glide is limited by the edge character of the dislocations with a Peierls stress at τ_P = 3.9 GPa. These results are in agreement with experimental observations of Yust (Yust 1969).

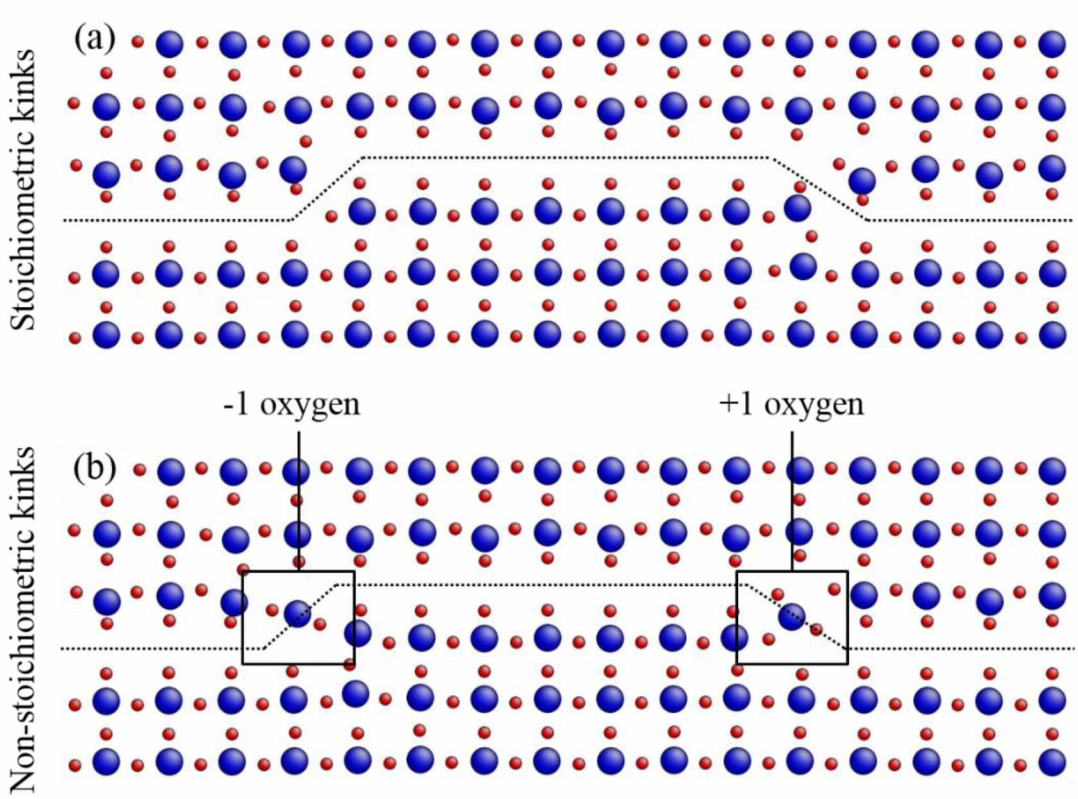

Figure 5: Relaxed atomic structure of a kink pair on a ½<110>{100} edge dislocation: (a) Stoichiometric kink pair and (b) non-stoichiometric kink pair. Uranium atoms are represented as big blue spheres and oxygen atoms as smaller red spheres.

At non-zero temperature and stress below τ_P, the dislocations glide by forming steps, called pairs of kinks. Their structure was studied in the main gliding system, i.e., kinks with a screw character on edge dislocations ½<110>{100}. Kinks of height b are considered, of different widths (equal to half the line length) and having two possible structures: the pairs can be stoichiometric or non-stoichiometric. For the second pair, the first kink has an oxygen interstitial and the second kink has an oxygen gap. The most stable configurations of these two types of pairs were deduced from energy minimization calculations based on different initial configurations of kinks. The lower energy structures for these two pairs are shown in Figure 5. Their formation energies are shown in Figure 6 as a function of their width. The non-stoichiometric pairs are more stable with a formation energy of about 2 eV for the pair.

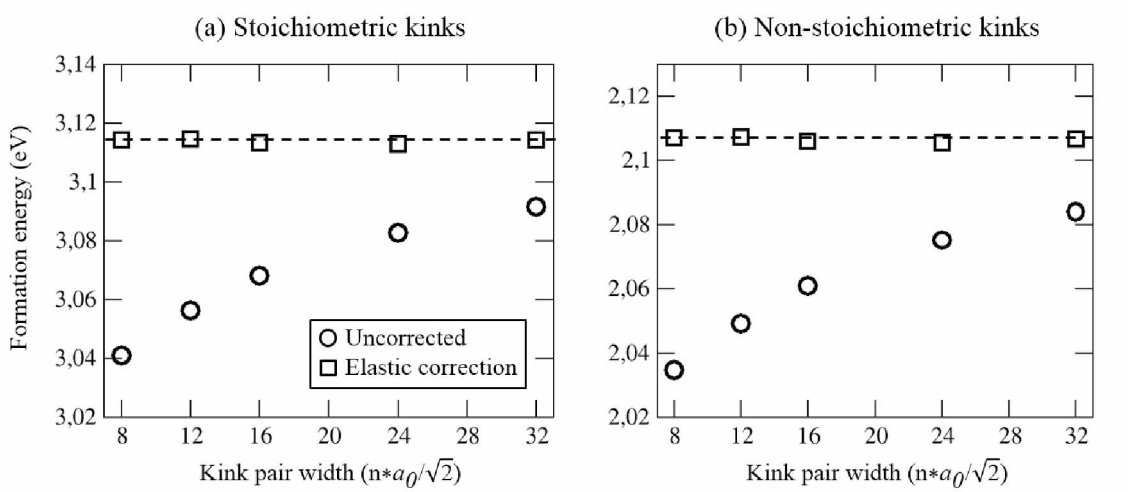

Figure 6: Kink pair formation energies as a function of their width for (a) the two stoichiometric kinks and (b) the two non-stoichiometric kinks on the ½<110>{100} edge dislocation shown on Figure 5. The uncorrected energies, as well as their corrected values considering their elastic interaction are drawn.

It must be stressed that the calculated energies include an elastic interaction term between steps, and therefore vary according to the width of the step. They must be corrected to obtain the energy of formation of isolated steps. This interaction energy, which must be subtracted from the raw energies, is written:

$$E^{interaction} = -\alpha \frac{b^2 h^2}{4\pi w}$$

With b the Burgers vector norm, w the distance between two offsets and h their height. α is the line tension (in GPa) calculated in anisotropic linear elasticity theory. Moreover, this interaction must be summed to take into account the images at the periodic limits. The corrected energies are shown on the right panel of Figure 6. One can see that they no longer vary with the width of the offset pair. The formation energy of a non-stoichiometric isolated double step (the most stable) is then 2.1 eV.

The main gliding system was therefore identified with its Peierls stress and the pairs of steps that can form in it. These data were used to establish a thermally activated gliding model of dislocations in UO_2, which determines as a function of temperature, the speed of dislocations of the main gliding system {100} and the evolution of the critical stress.

Thermally activated slip of the kink pairs

To study the thermally activated dislocation slip in {100} planes, the elastic interaction model between dislocations (Koizumi 1993) was used. This model allows us to determine the critical enthalpy $\Delta H^*(\tau)$ of germination of a double step at the external stress τ. $\Delta H^*(\tau)$ is the enthalpy necessary to obtain a seed of a step which will decrease the energy of the system upon expansion. The model is based on the Peierls potential V_P and the formation energy of a double kink $2H_k$ =2.1 eV. The Peierls potential is assumed to be sinusoidal and adjusted to reproduce the calculated critical stress τ_P=3.9 GPa.

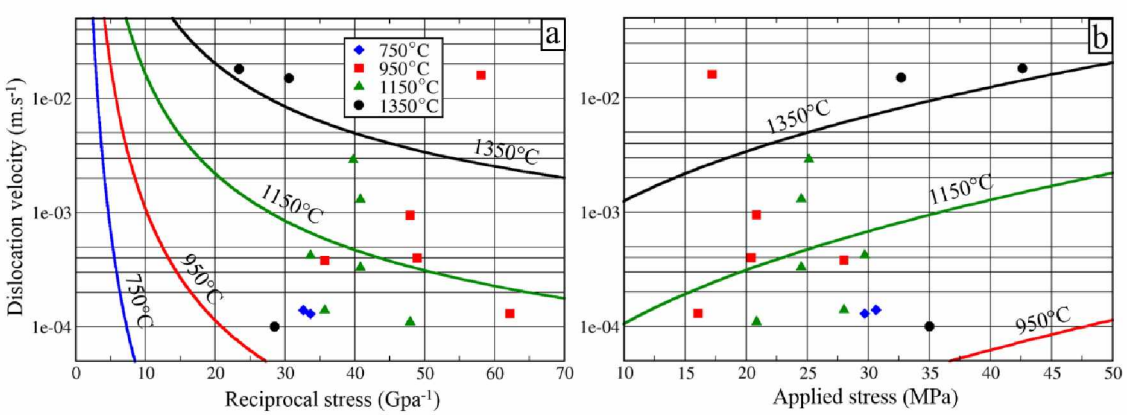

Figure 7: Dislocation velocities at 750°C, 950°C, 1150°C and 1350°C as a function of the inverse of the shear stress (left) and the shear stress (right). Drawn lines are velocities calculated with Eq. (11) and experimental data points are extracted from Yust and MacHargue (Yust 1969 – fig. 22).

The velocity law of dislocations can then be deduced, considering that a dislocation makes a jump from a Peierls valley when a pair of critical kinks succeeds to germinate on the dislocation line. The speed law v(T,τ) of dislocations is then :

$$v(T,\tau) = a.N.\beta(T).Z(T,\tau).exp\left(\frac{-\Delta H^*(\tau)}{k_B T}\right)$$

The exponential term is the probability of having a critical germ on the line at temperature T, a is the distance between two Peierls valleys, N is the number of germination sites and β(T) is the migration frequency of a kink. It is expressed with the Debye frequency ν_D and the migration energy E_m of the kinks:

$$\beta(T) = \nu_D \exp\left(\frac{-E_m}{k_B T}\right)$$

The migration barrier (E_m) was calculated at zero temperature by the Nudge Elastic Band method. It is 0.6 eV and is therefore not negligible compared to the energy of formation of a double step ($2H_K$ = 2.1 eV). Z(T,τ) is the Zeldovitch factor characterizing the probability that a critical seed will contract instead of expanding. It can be deduced from the elastic interaction model.

The dislocation velocities are shown in Figure 7 as a function of the inverse of the stress at different temperatures and are compared to the experimental velocities (Yust 1969). The calculated velocities are in agreement with the experimental data at 1150°C and 1350°C and are lower than these at low temperatures.

To obtain the critical stress τ* of dislocation slip as a function of temperature, one simply has to invert Orowan's law $\dot{\varepsilon} = \rho b v(T,\tau^*)$, by setting the strain rate $\dot{\varepsilon}$ to the experimental value of Yust et al. $\dot{\varepsilon}$ =0.0025 $m.s^{-1}$. The evolution of the critical stress obtained is shown in Figure *8*.

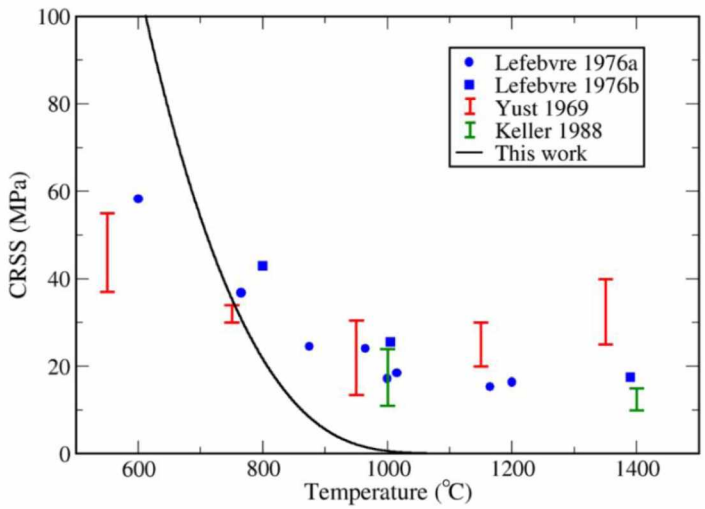

Figure 8: Evolution of the critical resolved shear stress with temperature for non-stoichiometric kinks ($2H_k$=2.1eV) in the experimental range of temperatures. Experimental values from Lefebvre (Lefebvre 1976), Yust & MacHargue (Yust 1969), and Keller et al. (Keller 1988) are also reported.

Our model is in good agreement with experimental data below 900°C. The thermally activated slip thus allows us to explain the evolution of the critical stress at low temperature. Conversely, above 900°C, the experimental critical stress becomes athermal, and our model is no longer applicable.

Conclusions

A model has been proposed for the thermally activated motion of dislocations at intermediate temperatures which gives the dislocation velocities and the evolution of the critical resolved shear stress (CRSS) with temperature. It required important prior calculations (generalized stacking faults and core structures calculations, main glide system and critical stress for straight dislocations at 0 K, kink pairs nature and formation and migration energies) with a complex potential (2nd moment tight-binding formalism and charge equilibration scheme). All calculations are done at 0 K and thermally dependent phenomena are derived from the thermal activation energy. Indeed calculations at 0 K avoid a bias introduced by the deformation rate in molecular dynamics shear tests at finite temperature and allow the derivation of dislocation mobility laws valid in the thermally activated regime. It gives CRSS values comparable to experimental results on stoichiometric UO_2 single crystals. It shows that the experimental CRSS decrease can be explained by a thermally activated glide in {100} planes of the ½<110> edge dislocation up to the transition to an athermal regime at 900°C.

2.3.2 Forest hardening interaction matrix calculated by Dislocation Dynamics simulations

In order to study the hardening induced by dislocations, the interaction strengths between UO_2 slip systems were caculated using MobiDiC Dislocation Dynamics (DD) code by Portelette and co-workers (Portelette 2020).

A model simulation was designed for each type of interaction between two given slip systems. One slip system was subject to the mechanical loading and its mobile dislocations accommodate an imposed strain rate. The other one (with a null Schmid factor) was made of a random population of obstacle dislocations. So only one type of reaction was obtained (junction or colinear interaction (Madec 2003), dipolar

interaction was not accounted). The interactions were simulated without lattice resistance so the caculated interaction coefficients a_{ij} can be used only close to the athermal regime. In this regime, the generalized forest model proposed by Franciosi (Franciosi et al. 1980) provides the critical resolved shear stress τ_c^i for each slip system:

$$\tau_c^i = \mu\, b\, (a_{ij}\, \rho^j)^{1/2}$$

as a function of an isotropic shear modulus μ, the Burgers vector magnitude b and the stored dislocation densities ρ^j. However, three different sets of coefficients were computed for three different sets of anisotropic elastic constants at three different temperatures using the Bacon-Scattergood approximation (see (Madec 2017) for details). Here mean values of coefficients are given because the effective Poisson coefficient ν_{BS} was not far from 1/3 for all the slip modes or the temperatures considered so the effect on coefficient values is limited.

Using the crystallographic symmetries, only 33 different interactions were obtained (taking into account the asymmetry of some of the interactions) as shown by the interaction matrix in Table *4*. Value of the strengthening coefficients $\alpha_i = a_i^{1/2}$ (easier to compare with scalar forest model parameter α) are given in Table *5* and the expected hierarchy of coefficients was obtained with very strong colinear interactions (i.e., annihilation of dislocations of different slip panes as a consequence associated with the greatest energy gain) and very weak Hirth junctions (when energy gain during reaction is marginal) and in between for other sessile and glissile junctions. In the case of UO_2 some of the Hirth junctions are so weak that very few junction events occur and the weakest coefficient is mainly a crossed state coefficient (Madec 2002) i.e. due to the effect of dislocation attractions in absence of reaction.

To have a complete set of coefficients (i.e. also with the diagonal and other dipolar terms terms), it is interesting to check the link between these coefficient values and the mean strength of dislocation forest by slip mode studied using DD simulations by Amodeo (Amodeo 2014). Indeed UO_2 and MgO share the same crystallography but in case of MgO only slip mode I and II are taken into account. Mean value of interaction between slip mode I in MgO $\alpha_{\mathrm{I}} = 0.28$ was found stronger than interaction between mode II $\alpha_{\mathrm{II}} = 0.24$. Taking into account the axis used by Amodeo so a slip system activation $\alpha_{\mathrm{I}} = (2\alpha_2+\alpha_1+\alpha_0)/4$ and $\alpha_{\mathrm{II}} = (2\alpha_4+\alpha_3+\alpha_0)/4$, so one can derive values for α_0' = 0.31 and α_1 = 0.11. Agreement with the only available DD evaluation for α_0' = 0.35 (see (Devincre 2007)) is not too bad, while for the few available DD evaluations lead to α_1 = 0.08-0.095 so are also close to the obtained value.

In terms of mean interaction intensity and in addition to the stronger interaction among mode I in comparison with mode II, the interaction among mode III is even stronger than among mode I or II because some slip systems in mode III share the same Burgers vector so are subject to colinear interaction. Cross interaction between slip modes are also stronger than interaction among mode I or II for the same reason so activation of mode I or mode II alone is a priori more favourable. This is in only partially in agreement with experimental data on the subject because simultaneous activation of mode I and II evidences exist and also some suspicions of mode III activation and in general only in presence of mode I or II. However, very few observations are fully in the athermal regime because thermal activation operates up to quite high temperature even for mode I (see Portelette 2018 and 2020 for more details)

		I						II						III											
		A1	A2	B3	B4	C5	C6	A1	B2	C3	D4	E5	F6	C1	D1	A2	B2	A3	C3	B4	D4	B5	C5	A6	D6
I	A1	a_0	a_1	a_2	a_2	a_2	a_2	a_5	a_6	a_7	a_7	a_7	a_7	a_{13}	a_{13}	a_{14}	a_{14}	a_{15}	a_{16}	a_{15}	a_{16}	a_{15}	a_{16}	a_{15}	a_{16}
	A2	a_1	a_0	a_2	a_2	a_2	a_2	a_6	a_5	a_7	a_7	a_7	a_7	a_{14}	a_{14}	a_{13}	a_{13}	a_{16}	a_{15}	a_{16}	a_{15}	a_{16}	a_{15}	a_{16}	a_{15}
	B3	a_2	a_2	a_0	a_1	a_2	a_2	a_7	a_7	a_5	a_6	a_7	a_7	a_{16}	a_{15}	a_{16}	a_{15}	a_{13}	a_{13}	a_{14}	a_{14}	a_{15}	a_{16}	a_{16}	a_{15}
	B4	a_2	a_2	a_1	a_0	a_2	a_2	a_7	a_7	a_6	a_5	a_7	a_7	a_{15}	a_{16}	a_{15}	a_{16}	a_{14}	a_{14}	a_{13}	a_{13}	a_{16}	a_{15}	a_{15}	a_{16}
	C5	a_2	a_2	a_2	a_2	a_0	a_1	a_7	a_7	a_7	a_7	a_5	a_6	a_{16}	a_{15}	a_{15}	a_{16}	a_{15}	a_{16}	a_{16}	a_{15}	a_{13}	a_{13}	a_{14}	a_{14}
	C6	a_2	a_2	a_2	a_2	a_1	a_0	a_7	a_7	a_7	a_7	a_6	a_5	a_{15}	a_{16}	a_{16}	a_{15}	a_{16}	a_{15}	a_{15}	a_{16}	a_{14}	a_{14}	a_{13}	a_{13}
II	A1	a_5^*	a_6^*	a_7^*	a_7^*	a_7^*	a_7^*	a_0	a_3	a_4	a_4	a_4	a_4	a_{17}	a_{17}	a_{18}	a_{18}	a_{19}	a_{20}	a_{19}	a_{20}	a_{19}	a_{20}	a_{19}	a_{20}
	B2	a_6^*	a_5^*	a_7^*	a_7^*	a_7^*	a_7^*	a_3	a_0	a_4	a_4	a_4	a_4	a_{18}	a_{18}	a_{17}	a_{17}	a_{20}	a_{19}	a_{20}	a_{19}	a_{20}	a_{19}	a_{20}	a_{19}
	C3	a_7^*	a_7^*	a_5^*	a_6^*	a_7^*	a_7^*	a_4	a_4	a_0	a_3	a_4	a_4	a_{20}	a_{19}	a_{20}	a_{19}	a_{17}	a_{17}	a_{18}	a_{18}	a_{19}	a_{20}	a_{20}	a_{19}
	D4	a_7^*	a_7^*	a_6^*	a_5	a_7^*	a_7^*	a_4	a_4	a_3	a_0	a_4	a_4	a_{19}	a_{20}	a_{19}	a_{20}	a_{18}	a_{18}	a_{17}	a_{17}	a_{20}	a_{19}	a_{19}	a_{20}
	E5	a_7^*	a_7^*	a_7^*	a_7^*	a_5^*	a_6^*	a_4	a_4	a_4	a_4	a_0	a_3	a_{20}	a_{19}	a_{19}	a_{20}	a_{19}	a_{20}	a_{20}	a_{19}	a_{17}	a_{17}	a_{18}	a_{18}
	F6	a_7^*	a_7^*	a_7^*	a_7^*	a_6^*	a_5^*	a_4	a_4	a_4	a_4	a_3	a_0	a_{19}	a_{20}	a_{20}	a_{19}	a_{20}	a_{19}	a_{19}	a_{20}	a_{18}	a_{18}	a_{17}	a_{17}
III	C1	$a_{13}^*a_{14}^*a_{16}^*a_{15}^*a_{16}^*a_{15}^*$						$a_{17}^*a_{18}^*a_{20}^*a_{19}^*a_{20}^*a_{19}^*$						a_0	a_8	a_9	a_9	a_{10}	a_{11}	a_{12}	a_{10}^*	a_{10}	a_{11}	a_{12}	a_{10}^*
	D1	$a_{13}^*a_{14}^*a_{15}^*a_{16}^*a_{15}^*a_{16}^*$						$a_{17}^*a_{18}^*a_{19}^*a_{20}^*a_{19}^*a_{20}^*$						a_8	a_0	a_9	a_9	a_{12}	a_{10}^*	a_{10}	a_{11}	a_{12}	a_{10}^*	a_{10}	a_{11}
	A2	$a_{14}^*a_{13}^*a_{16}^*a_{15}^*a_{15}^*a_{16}^*$						$a_{18}^*a_{17}^*a_{20}^*a_{19}^*a_{19}^*a_{20}^*$						a_9	a_9	a_0	a_8	a_{11}	a_{10}	a_{10}^*	a_{12}	a_{10}^*	a_{12}	a_{11}	a_{10}
	B2	$a_{14}^*a_{13}^*a_{15}^*a_{16}^*a_{16}^*a_{15}^*$						$a_{18}^*a_{17}^*a_{19}^*a_{20}^*a_{20}^*a_{19}^*$						a_9	a_9	a_8	a_0	a_{10}^*	a_{12}	a_{11}	a_{10}	a_{11}	a_{10}	a_{10}^*	a_{12}
	A3	$a_{15}^*a_{16}^*a_{13}^*a_{14}^*a_{15}^*a_{16}^*$						$a_{19}^*a_{20}^*a_{17}^*a_{18}^*a_{19}^*a_{20}^*$						a_{10}^*	a_{12}	a_{11}	a_{10}	a_0	a_8	a_9	a_9	a_{12}	a_{10}^*	a_{11}	a_{10}
	C3	$a_{16}^*a_{15}^*a_{13}^*a_{14}^*a_{16}^*a_{15}^*$						$a_{20}^*a_{19}^*a_{17}^*a_{18}^*a_{20}^*a_{19}^*$						a_{11}	a_{10}	a_{10}^*	a_{12}	a_8	a_0	a_9	a_9	a_{10}	a_{11}	a_{10}^*	a_{12}
	B4	$a_{15}^*a_{16}^*a_{14}^*a_{13}^*a_{16}^*a_{15}^*$						$a_{19}^*a_{20}^*a_{18}^*a_{17}^*a_{20}^*a_{19}^*$						a_{12}	a_{10}^*	a_{10}	a_{11}	a_9	a_9	a_0	a_8	a_{11}	a_{10}	a_{12}	a_{10}^*
	D4	$a_{16}^*a_{15}^*a_{14}^*a_{13}^*a_{15}^*a_{16}^*$						$a_{20}^*a_{19}^*a_{18}^*a_{17}^*a_{19}^*a_{20}^*$						a_{10}	a_{11}	a_{12}	a_{10}^*	a_9	a_9	a_8	a_0	a_{10}^*	a_{12}	a_{10}	a_{11}
	B5	$a_{15}^*a_{16}^*a_{15}^*a_{16}^*a_{13}^*a_{14}^*$						$a_{19}^*a_{20}^*a_{19}^*a_{20}^*a_{17}^*a_{18}^*$						a_{10}^*	a_{12}	a_{10}	a_{11}	a_{12}	a_{10}^*	a_{11}	a_{10}	a_0	a_8	a_9	a_9
	C5	$a_{16}^*a_{15}^*a_{16}^*a_{15}^*a_{13}^*a_{14}^*$						$a_{20}^*a_{19}^*a_{20}^*a_{19}^*a_{17}^*a_{18}^*$						a_{11}	a_{10}	a_{12}	a_{10}^*	a_{10}	a_{11}	a_{10}^*	a_{12}	a_8	a_0	a_9	a_9
	A6	$a_{15}^*a_{16}^*a_{16}^*a_{15}^*a_{14}^*a_{13}^*$						$a_{19}^*a_{20}^*a_{20}^*a_{19}^*a_{18}^*a_{17}^*$						a_{12}	a_{10}^*	a_{11}	a_{10}	a_{11}	a_{10}	a_{12}	a_{10}^*	a_9	a_9	a_0	a_8
	D6	$a_{16}^*a_{15}^*a_{15}^*a_{16}^*a_{14}^*a_{13}^*$						$a_{20}^*a_{19}^*a_{19}^*a_{20}^*a_{18}^*a_{17}^*$						a_{10}	a_{11}	a_{10}^*	a_{12}	a_{10}^*	a_{12}	a_{10}	a_{11}	a_9	a_9	a_8	a_0

Table 4 : Interaction matrix for UO_2. Each line represents a mobile system, each column a forest system (see the adapted Schmid and Boas notation given in *Table 6*). The pairs of coefficients a_i/a_i^* are related to an asymmetrical reaction i.e. the coefficient values differ when the role -mobile or forest- of the systems are permuted.

α_i	mobile & forest slip systems	Interaction	*value*	α_i	mobile & forest slip systems	Interaction	value
α_0'	A_I1, A_I1	$self$	-	α_{13}	$A_I1, C_{III}1$	$colinear^{55°}_{I/III}$	*0.78±0.05*
α_1	A_I1, A_I2	$dipole_{I/I}$	-	α_{13}*	$C_{III}1, A_I1$	$colinear^{55°}_{III/I}$	*0.75±0.05*
α_2	A_I1, B_I3	$glissile^{II}_{I/I}$	*0.35±0.03*	α_{14}	$A_I1, A_{III}2$	$Hirth_{I/III}$	*0.10±0.01*
α_3	$A_{II}1, B_{II}2$	$Hirth_{II/II}$	*0.15±0.02*	α_{14}*	$A_{III}2, A_I1$	$Hirth_{III/I}$	*0.12±0.01*
α_4	$A_{II}1, C_{II}3$	$sessile^{\{112\}}_{II/II}$	*0.25±0.03*	α_{15}	$A_I1, A_{III}3$	$glissile^{III}_{I/IIIa}$	*0.40±0.04*
α_5	$A_I1, A_{II}1$	$colinear^{90°}_{I/II}$	*0.82±0.05*	α_{15}*	$A_{III}3, A_I1$	$glissile^{III}_{III/Ia}$	*0.36±0.03*
α_5*	$A_{II}1, A_I1$	$colinear^{90°}_{II/I}$	*0.86±0.06*	α_{16}	$A_I1, C_{III}3$	$glissile^{III}_{I/IIIb}$	*0.33±0.04*
α_6	$A_I1, B_{II}2$	$Hirth_{I/II}$	*0.10±0.02*	α_{16}*	$C_{III}3, A_I1$	$glissile^{III}_{III/Ib}$	*0.27±0.03*
α_6*	$B_{II}2, A_I1$	$Hirth_{II/I}$	*0.14±0.02*	α_{17}	$A_{II}1, C_{III}1$	$colinear^{35°}_{II/III}$	*0.65±0.04*
α_7	$A_I1, C_{II}3$	$glissile^{I}_{I/II}$	*0.41±0.06*	α_{17}*	$C_{III}1, A_{II}1$	$colinear^{35°}_{III/II}$	*0.62±0.04*
α_7*	$C_{II}3, A_I1$	$glissile^{I}_{II/I}$	*0.40±0.05*	α_{18}	$A_{II}1, A_{III}2$	$Hirth^{\{012\}}_{II/III}$	*0.16±0.02*
α_8	$C_{III}1, D_{III}1$	$colinear^{70°}_{III/III}$	*0.78±0.05*	α_{18}*	$A_{III}2, A_{II}1$	$Hirth^{\{012\}}_{III/II}$	*0.14±0.01*
α_9	$C_{III}1, A_{III}2$	$Hirth_{III/III}$	*0.16±0.01*	α_{19}	$A_{II}1, A_{III}3$	$sessile^{\{113\}}_{II/III}$	*0.31±0.04*
α_{10}	$C_{III}1, A_{III}3$	$glissile^{III}_{III/III}$	*0.30±0.04*	α_{19}*	$A_{III}3, A_{II}1$	$sessile^{\{113\}}_{III/II}$	*0.32±0.04*
α_{10}*	$A_{III}3, C_{III}1$	$glissile^{III}_{III/III}$	*0.32±0.03*	α_{20}	$A_{II}1, C_{III}3$	$glissile^{III}_{II/III}$	*0.31±0.05*
α_{11}	$C_{III}1, C_{III}3$	$dipole_{III/III}$	-	α_{20}*	$C_{III}3, A_{II}1$	$glissile^{III}_{III/II}$	*0.27±0.04*
α_{12}	$C_{III}1, B_{III}4$	$glissile^{I,L}_{III/III}$	*0.38±0.05*				

Table 5 : Strengthening coefficient in UO_2. A couple of mobile versus forest systems is given, interactions are labelled as self, dipole, glissile, Hirth, colinear and sessile. Self and dipole account respectively for self (without distinction between slip modes) and dipolar interactions when interacting Burgers vectors differ. Glissile, Hirth, colinear and sessile refer to the different types of junction. Dipoles and junctions are labeled using intersecting modes, as subscript, and specific property, as junction plane or reaction orientation, as superscript. Glissile refers to junctions lying in fluorite crystallographic slip plane. Sessile is for a/2<110> junctions not lying in fluorite crystallographic slip plane. Hirth refers for weaker sessile junctions with a a<100> Burgers vectors. Colinear is for colinear interaction and is labelled using the angle between cross slip planes, as superscript. Value is the mean value obtained using the simulations with the elastic constants at 1373 K, 1600 K and 1973 K.

2.4 Impact of irradiation defects on elastic properties

2.4.1 Defect evolution with dose

Two main types of irradiation effects inducing microstructural and crystal deffects are generally represented in fuel models with: atom cascades consecutive to the fission spikes and gaseous fission products migration in the parent material. The first one is the consequence of a balistic transmission of the kinetic energy of the fission products and will be named “dose” in the present section. Urania faces significant doses during their lifetimes in reactors. These irradiations significantly modify their initial physical properties leading to drastic industrial concerns, whether for a safe and efficient use in reactors.

It is known for a long time that UO_2 nuclear fuel shows progressive transformations towards a rim structure during irradiation exposure. This rim structure is characterized by a fine grain subdivision and a high proportion of pores. Prior to the formation of the rim structure, XRD measurements exhibit a first peak of lattice expansion – contraction. The swelling was attributed to the contribution of point defects and/or fission products produced by irradiation while contraction was associated to point defect transformation into unfaulted loops, which releases strain. However, these scenarios are largely inferred from independent pieces of information, but yet no direct evidence supports this rationale although it is widely adopted in mesoscale codes.

Some years ago (Chartier 2005, Crocombette 2006) a simulation methodology was proposed at the atomic scale which allows to provide the material microstructure evolution as a function of irradiation dose. It consists in a continuous accumulation of interstitial-vacancy pairs performed via molecular dynamics simulations.

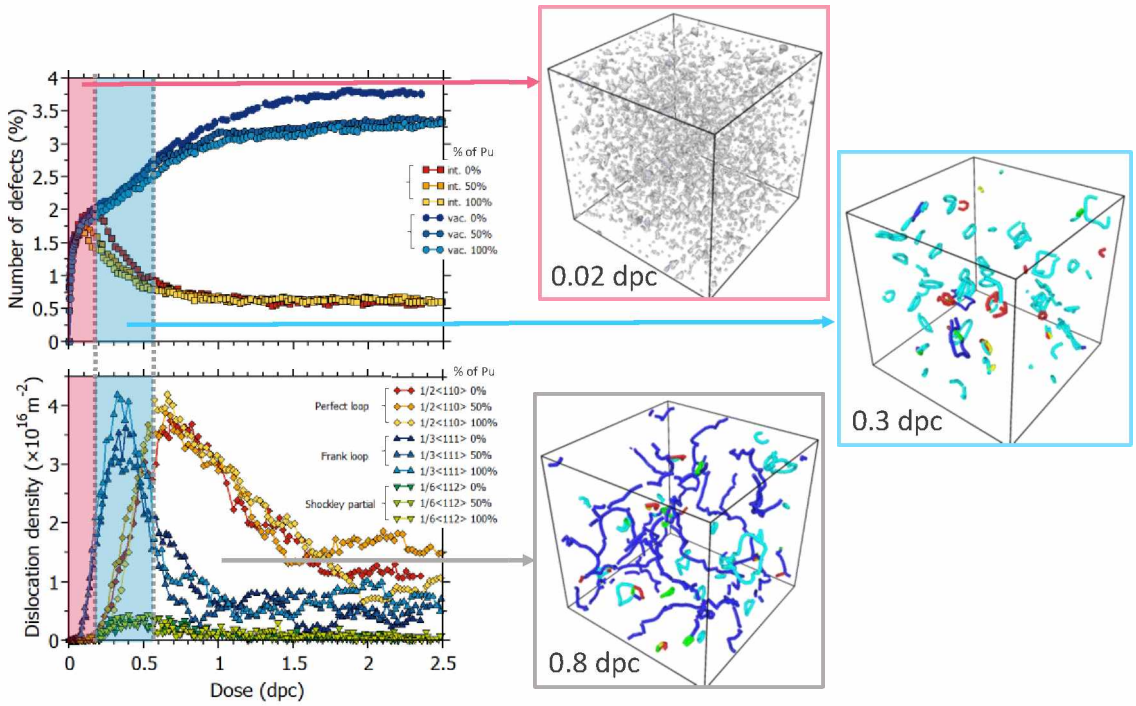

Figure 9: Evolution of the number of point defects and dislocation density as a function of dose expressed in dpc (displacement per cation) for $U_{1-x}Pu_xO_2$ at 300 K. Three snapshots of the simulation box are also displayed to illustrate the damage. In these figures the grey dots at 0.02 dpc represent the track of the point defects. For clarity only the dislocation lines are represented in the figure at 0.3 and 0.8 dpc (dark blue: perfect loop, cyan: Frank loops, green: Shockley partials).

With this method, it is possible to correlate some effect of the UO_2 irradiation-induced damage evolution with some lattice expansion-contraction via simulated XRD analysis (Chartier 2016). This methodology was extended to the case of MOX fuel ($UPuO_2$) (Balboa 2018) and showed that nucleation and growth of dislocations for both materials follow a five stages process (see Figure *9*):

- (1) point defects are first created by irradiation (Figure *9* at 0.02 dpc),

- (2) subsequently they aggregate into clusters,

- (3) from which nucleate Frank loops (Figure *9* at 0.3 dpc),
- (4) which transform into unfaulted loops via Shockley that in turn grow, and
- (5) finally reorganize into forest dislocations (Figure *9* at 0.8 dpc).

Analysis of simulated XRD from these simulated-damaged systems shows that part of the lattice expansion could be related to stages (1) to (3) with a significant contribution of Frank loops, while the onset of lattice contraction starts with stage (4), *i.e.*, when unfaulted loops nucleate and form a perfect dislocation network. However, it is worth noticing that the contribution of fission products were not taking into account in theses simulations and certainly plays a significant role in the lattice expansion-contraction processes.

Following this structural analysing, the evolution of the mechanical properties with irradiation dose was investigated.

2.4.2 Elastic properties as a function of dose

The elastic moduli are computed for several irradiated configurations described above. The evolution of the bulk modulus, the maximum shear modulus, and the Poisson's ratio as a function of dose expressed in displacement per cation (dpc) are displayed in Figure *10*. Three compounds with different Pu content are presented in each graph to help the comparison between the different materials. Also, highlights in pink and blue are systematically added to represent the evolution of the microstructure as described above.

The evolution of these moduli with irradiation dose is approximately the same. A stiff decrease of the moduli is observed within the first 0.2 dpc followed by a slight decrease and a plateau at higher doses. The drop of the bulk modulus calculated for the full range of doses studied herein is about 13%. For the shear modulus, the decrease is homogeneous for all the cases at about 17.5%.

In all the cases the Pu content does not have an influence on the main behavior only the absolute values change. This indicates that the mechanical elastic properties depend strongly on the nature of the defect rather than the chemical species. Moreover, the significant decrease of the moduli seems directly correlated with the isolated point defects and the Frank loop density and not so much with the perfect dislocation density.

The behavior of the Poisson's ratio is more complex, but it seems also that both isolated point defects and Frank dislocations influence the Poisson effect more than the perfect dislocation.

This indicates that isolated point defects play a major role in the degradation of the mechanical elastic properties as in the lattice swelling effect, which appear at low irradiation doses. However, more simulations studying particular defect type and temperature effect are still needed to confirm this result.

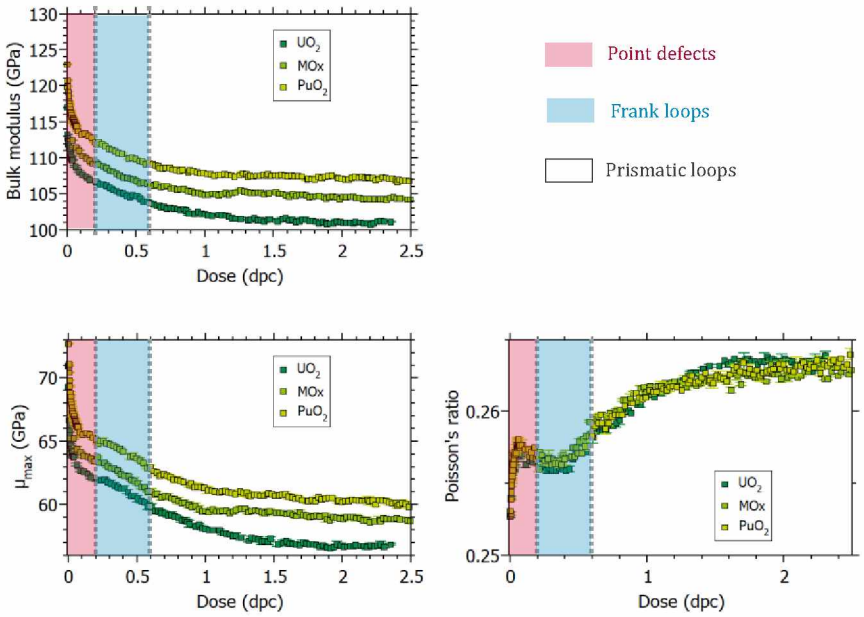

Figure 10 : Evolution of the bulk modulus, the maximum shear modulus, and the Poisson's ration as a function of dose in UO_2, $U_{0.5}Pu_{0.5}O_2$, and PuO_2 at 300 K. The colour band (pink, blue, and white) corresponds to the dominant defects present at the dose.

2.5 Fission gas pressure in bubbles and intragranular bubble/matrix interface characteristics

The micromechanical models used to describe the elastic and plastic behavior of irradiated UO_2 rely on the knowledge of fission gas bubble characteristics (in particular, size and pressure). Thus, molecular dynamics and Monte Carlo methods, using semi-empirical interatomic potentials, were employed in order to characterize the intragranular bubbles (Geng et al, JAC, 2008, Chartier et al, PRB, 2010, Liu et al, JNM, 2015) and to quantify their impact and that of nanoporosities on fuel elastic properties (Jelea et al, JNM, 2011). The calculations on the impact of nanoporosities on the UO_2 elastic properties showed an excellent agreement with experimental results available in the literature as well as with conventional micromechanics (homogenization) approaches (*Figure 11*). They demonstrated on the one hand the ability of molecular dynamics to establish a relationship between atomic and mesoscopic scales. On the other hand, this work highlighted the importance of surface/interface effects of nanoporosities (gas-free bubbles) that should be taken into account in micro and macro-mechanical models. This type of behavior is classic in the field of nanomaterials and is directly attributable to the size of the intragranular bubbles. This study was extended to the thermal properties of UO_2 (Colbert et al, JAP, 2014) by developing an original analytical model, based on geometrical approaches and on the kinetic model, to take explicitly into account the surface porosity effect. The results are also in perfect agreement with the classical homogenization approaches, but with the presence of an additional term due to the interface effects.

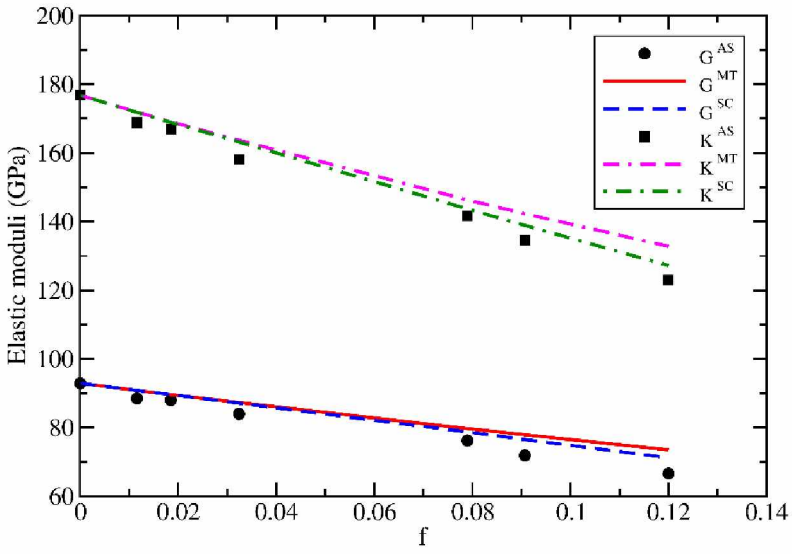

Figure 11 : Variation of the bulk modulus K and shear modulus G versus porosity f at 0 K: the atomistic simulation results (AS) are compared with the Mori-Tanaka (MT) and self-consistent (SC) predictions.

The isothermal adsorption of xenon in nanoporous UO_2 system was also studied using a Grand Canonical Monte Carlo approach. The structural analysis showed that the adsorbed xenon has a high density and does not exhibit a well-defined crystalline structure but a glassy state, in agreement with other results from the literature (Murphy et al, PRB, 2012). Other studies (Jelea et al, JNM, 2014), dealing with effects of temperature, showed that it had no significant impact on the pressure or swelling of intragranular bubbles. Thus, the hypothesis of a gas swelling of the fuel driven by an increase in pressure in the bubbles during a temperature transient can be excluded. In fact, the temperature does not drastically modify the stress field around the bubble but could allow relaxation processes to be activated (emission of dislocations or migration of vacancies) and possibly accelerate the diffusion of gaseous species to the bubbles, which can ultimately induce fuel swelling (Colbert et al, JPCM, 2014).

In order to better characterize the UO_2/xenon interfaces, the behavior of different flat UO_2 surfaces, and their interactions with xenon was studied and compared (*Figure 12*). This study showed that the surface relaxation was driven by electrostatic effects (Arayro et al, JPCM, 2015) and that the UO_2/xenon interface has a non-negligible impact on the xenon pressure in the bubble (Arayro et al, JPC, 2018).

All of these works establish that, in order to accurately model the effects of bubble on macroscopic thermomechanical fuel properties, the porosity distribution must be taken into account as well as the total pore fraction. More generally, it was proved that atomic approaches were consistent with micro-mechanical approaches, that they could provide the latter either in terms of numerical data (interface sizes, stress values in the bubbles and matrix) or in terms of physical phenomena to be considered (taking into account surface effects). In addition, they highlighted the ability of these approaches to directly develop macroscopic behavioral laws that take into account the fine microstructure of materials (thermal conductivity law). Nevertheless, electrostatic interactions play a major role in surface effects, and the results obtained here should be confirmed using variable charge potentials such that the SMTB-Q (Sattonnay et al, J. Phys: Condens Matter, 2013).

Important work remains to be done on the characterization of the interface mechanical properties in order to bring together micro-mechanical and atomistic models and to generate coherent combustible behavior laws. In addition, the kinetic aspects, that probably play a very important role in the behavior of nanometric bubbles, should be elucidated.

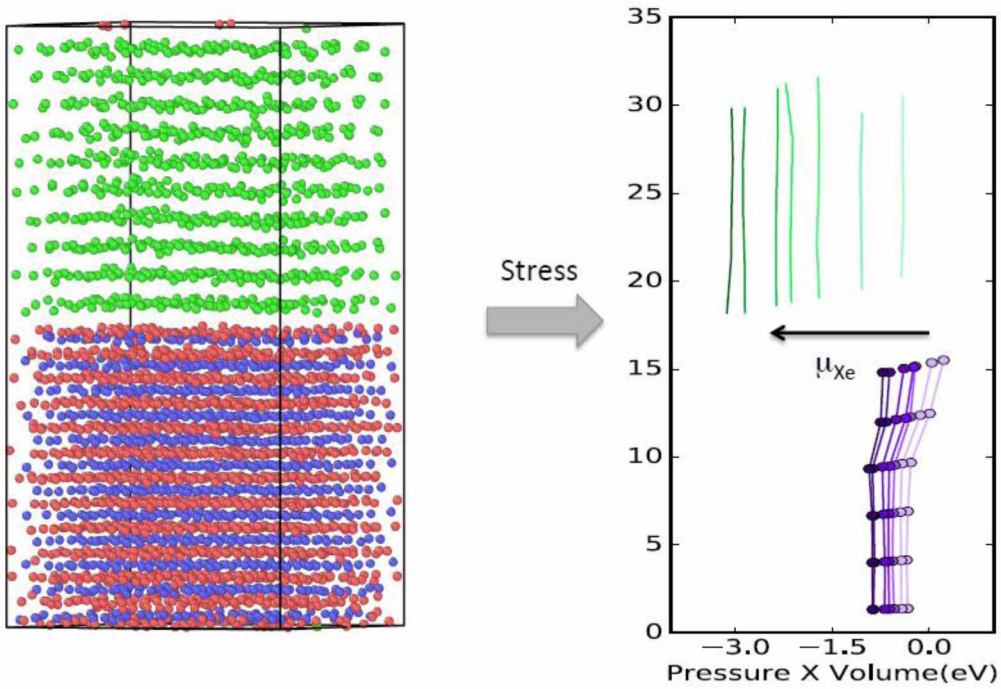

Figure 12 : Adsorption of Xe (in green) on a (100) UO_2 surface (in blue and red) and associated stresses according to the chemical potential of Xe.

2.6 Mechanics of defect generation and fracture

This section describes a relatively new modelling formalism, the phase-field crystal (PFC) methodology, which is of interest as it reproduces many mechanical phenomena in a single continuum equation. The physics and mechanisms of interest here are; defect generation, deformation, plasticity, and fracture. The PFC model is a spatially atomic-level method but with diffusive time-scale dynamics. The system is described by a continuum-scale energy functional sensitive to the periodicity of an atomic density probability distribution ρ. This gives rise to a multitude of self-consistent microstructurally relevant physical features such as multiple phases and crystal orientations, topological defects and elasto-plastic behavior. The prevailing energy functional is formulated as follows (Elder 2002, Elder 2004, Elder 2007, Greenwood 2010),

$$F[\rho] = \int_V (f_{ideal} + f_{excess} + f_{external})dV \quad (1)$$

$$f_{ideal} = \rho \ln\frac{\rho}{\rho_o} - \delta\rho \quad (2)$$

$$f_{excess} = -\frac{1}{2}\delta\rho \int dV' C(V,V';\tau)\,\delta\rho(V') \quad (3)$$

where f_{ideal} is the ideal free energy which defines the uniform phases, often expanded to a polynomial of fourth order, $\delta\rho = \rho - \rho_o$ with ρ_o being some reference constant density and f_{excess} is the excess energy density that stabilizes periodic structures, i.e. crystals. The final term, $f_{external}$ sets an external energy term and can be a source term for mechanical strain and response, magnetism, radiation damage, athermal kinetics, and other externally applied conditions

The terms f_{ideal} and f_{excess} constitute the thermodynamic portion of the free energy functional. The type of structure realized is determined by the construction of the two-point correlation function, $C(V, V'; \tau)$ with τ being a temperature parameter. Note that in the initial and simple descriptions of the PFC model, the correlation function is expanded in gradients. The model evolves using dissipative dynamics of conserved systems,

$$\frac{\partial \rho}{\partial t} = M\nabla^2 \frac{\delta F}{\delta \rho} \tag{4}$$

where M the mobility which establishes the evolution rate and time scale.

While the formalism was well established to address defect structure and motion (Elder 2004, Berry 2008), the first work to quantitatively establish the stability of dislocation defects and their dynamics leading to plastic flow was Berry et al. (Berry 2012, Berry 2014). In these works, they ascertained the various formulations of the PFC model formulations ability to stabilize different dislocation structures, and their reactions, followed by direct application to the mechanical response of a nano-polycrystalline sample. Furthering this work, Kong et al. (Kong 2018), modelled the explicit defect reactions and dynamics that take place in crystalline systems, particularly highlighting the grain deformation mechanism through which defects migrate. Using a 2D system, they have studied the migration of dislocations and strain-driven nucleation and deformation. What became evident in their study is the deformation mechanism accompanying the migration and eventual annihilation process leading to the ''nucleation'' of subgrains structures with accommodating orientation relationships.

Material failure by way of crack formation and fracture has begun to be addressed by this formalism. While other methods have been used to study fracture, none fully capture the underlying crystallographic features except molecular dynamics which does not capture the diffusive dynamics involved in the process. Hu et al. (Hu 2016) investigated crack propagation under shear stress and different grain orientations showing an atomically sharp crack and its changing path as shown in Figure 13a. It was shown that larger orientations allowing the crack to assume a more serrated path through the grain attributed to void nucleation ahead of the crack changing the preferred cleavage direction. The criticality of the crack progression was considered as functions of the critical strain required to extend and grow cracks as well as the anisotropic nature of the applied tensile load leading to a so-called branched structures (Yingjun 2016). Specifically of note is the emergence of the branched structure when the different strain energies approach a critical value, Figure 13b.

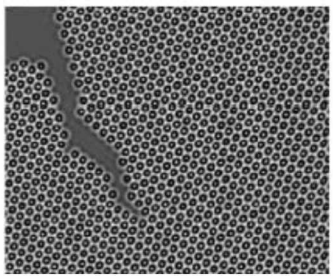

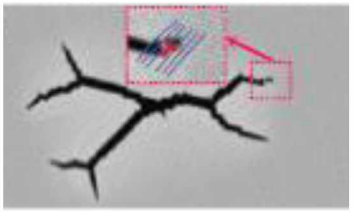

Figure 13: Phase-field crystal predictions of crack propagation showing a) changing path due to void nucleation ahead of the crack (Hu 2016), and b) branching under applied strain (Yingjun 2016).

The phase-field crystal methodology has proven to be a robust formalism from which defect generation and dynamics, elastic response, plastic flow and crack propagation naturally emerge. There are ongoing efforts to make this a truly mesoscale theory through coarse-graining methods, so-called amplitude expansions (Yeon 2010, Ofori-Opoku-Stolle 2013), while still describing multiple phases, orientations, and defects (Provatas 2007, Salvalaglio 2017, Salvalaglio 2019). The method can also treat multiple phases and components, and a host of different crystallographic structures (Ofori-Opoku-Fallah 2013, Smith 2017, Alster 2017) in an equally self-consistent manner. Progress has also been made in including a vapour phase to the formalism (Schwalbach 2013, Kocher 2015).

3 Viscoplastic behavior

The viscoplastic behavior of the fuel pellet plays a key role on the cladding tube integrity during nominal and accidental reactor operations (Michel et al. 2008, Michel et al. 2013). The temperature range to consider for viscoplastic behavior under normal and transient operating conditions is approximately between 1100°C and 1800°C. Considering these temperatures and the strain rate under a power transient loading (around $10^{-4}\ s^{-1}$) it has been established that viscoplastic behavior in UO_2 is mainly governed by dislocation motion (Frost&Ashby 1982) and is then called dislocation creep. To have a multiscale understanding of the viscoplastic behavior the present section first focuses on single crystal creep tests and models in 3.1, then the effect of porosities is analysed in 3.2 and 3.3, and finally polycrystalline and porous microstructures are discussed in 3.4 and 3.5 .

3.1 Single crystal viscoplastic behavior from dislocation motion

Thermally activated dislocation gliding mechanism can be investigated with single crystal experimental compression tests as proposed by several authors. The three different dislocation slip modes of UO_2 usually referenced in the literature are ½<110>{100}, ½<110>{110} and ½<110>{111} (Rapperport&Huntress 1960, Keller et al. 1988). Those systems are also observed in other fluorite materials as *e.g.* CaF_2 (Evans et al. 1966, Keig&Coble 1968), BaF_2 (Liu&Li 1964) and ThO_2 (Edington&Klein 1866, Gilbert 1965). In the following the extended Schmid and Boas notation proposed in (Portelette et al. 2018) is used, the ½<110>{100} and ½<110>{110} slip systems will be referred to as I and II respectively while the ½<110>{111} is referenced as III. Slip directions, planes and systems are given in Table 6.

Burgers vectors labeled with a number following Schmid and Boas

1 [011]	2 $[01\bar{1}]$	3 [101]	4 $[10\bar{1}]$	5 $[1\bar{1}0]$	6 [110]

{100} slip planes labeled with a letter and I index

A_I (100)	B_I (010)	C_I (001)

{110} slip planes labeled with a letter and II index

A_{II} $(01\bar{1})$	B_{II} (011)	C_{II} $(10\bar{1})$	D_{II} (101)	E_{II} (110)	F_{II} $(1\bar{1}0)$

{111} slip planes labeled with a letter following Schmid and Boas and III index

A_{III} $(1\bar{1}\bar{1})$	B_{III} (111)	C_{III} $(11\bar{1})$	D_{III} $(1\bar{1}1)$

Available planes for each Burgers vector (one I plane, one II plane and two III planes)

Burgers vectors	I slip system	II slip system	III slip systems
1	A_I1	$A_{II}1$	$C_{III}1$, $D_{III}1$
2	A_I2	$B_{II}2$	$A_{III}2$, $B_{III}2$
3	B_I3	$C_{II}3$	$A_{III}3$, $C_{III}3$
4	B_I4	$D_{II}4$	$B_{III}4$, $D_{III}4$
5	C_I5	$E_{II}5$	$B_{III}5$, $C_{III}5$
6	C_I6	$F_{II}6$	$A_{III}6$, $D_{III}6$

Table 6 : Slip directions, planes and systems in UO_2.

Single crystal viscoplastic behavior has also been investigated at low temperature through SEM in situ micro-pillar tests as proposed in reference (Frazer&Hosemann 2019).

Dislocation mobility law

As proposed in (Portelette et al. 2018), dislocation mobility can be described with an Arrhenius function that depends on both resolved shear stress and temperature, equation (5).

$$v^{\alpha} = \nu_D b \exp\left(-\frac{\Delta H_0^i}{k_b T}\right)\left(\cosh\left(\frac{\tau^{\alpha}}{\tau_0^i}\right) - 1\right) \quad (5)$$

Where $\nu_D = 4.94 \times 10^{13} s^{-1}$ is the Debye frequency, b is the Burgers magnitude, k_b the boltzman constant, T the temperature, ΔH_0^i is the dislocation glide activation energy and τ_0^i a critical shear stress. Here, *i* refers respectively to {100}, {110} or {111} modes. For *i*={100}, $\alpha \in [1; 6]$, for *i*={110} $\alpha \in [7; 12]$ and for *i*={111} $\alpha \in [13; 24]$. $\nu_D = \Theta_D/(h.k_B)$ where the Debye temperature Θ_D=377 K and h the Plank constant.

Finite element modelling of crystal plasticity

In order to have an accurate assessment of the crystal rotation effect it is recommended to use a finite strain formulation. In the latter the crystal plasticity model is based on the classical multiplicative Kröner-Lee decomposition of the transformation gradient tensor $\bar{\bar{F}}$:

$$\bar{\bar{F}} = \bar{\bar{F}}^e \bar{\bar{F}}^p \tag{6}$$

where $\bar{\bar{F}}^p$ is the plastic transformation gradient and $\bar{\bar{F}}^e$ is the elastic transformation gradient. The elastic part of the behavior is based on the hyperelastic Saint-Venant Kirchhoff law in the intermediate configuration which relates the second Piola-Kirchhoff stress tensor to the Green-Lagrange strain as follows:

$$\bar{\bar{E}}^e_{GL} = \frac{1}{2}\left(\bar{\bar{F}}^{e\,T}\bar{\bar{F}}^e - \bar{\bar{I}}\right) \tag{7}$$

$$\bar{\bar{\pi}} = \bar{\bar{\bar{\bar{C}}}} : \bar{\bar{E}}^e_{GL} \tag{8}$$

where $\bar{\bar{\bar{\bar{C}}}}$ is the elastic stiffness derived from Hutching's neutron scattering data that provide single crystal elastic constants for a large range of temperature (Hutching 1987).

The plastic transformation, $\bar{\bar{L}}_p$, is derived from the transformation gradient rate as the sum of each slip system's shear rate contribution as defined in equation (9). The latter uses the non symetric Schmid tensor definition $\bar{\bar{S}}^\alpha = \vec{m}^\alpha \otimes \vec{n}^\alpha$, where $\vec{n}^\alpha$ and $\vec{m}^\alpha$ are respectively the system plane normal and the slip direction of the slip system α. N_s is the number of slip systems.

$$\bar{\bar{L}}^p = \dot{\bar{\bar{F}}}^p \bar{\bar{F}}^{p\,-1} = \sum_{\alpha=1}^{N_S} \dot{\gamma}^\alpha . \bar{\bar{S}}^\alpha = \overbrace{\sum_{\alpha=1}^{6} \dot{\gamma}^\alpha . \bar{\bar{S}}^\alpha}^{\{100\}} + \overbrace{\sum_{\alpha=7}^{12} \dot{\gamma}^\alpha . \bar{\bar{S}}^\alpha}^{\{110\}} + \overbrace{\sum_{\alpha=13}^{24} \dot{\gamma}^\alpha . \bar{\bar{S}}^\alpha}^{\{111\}} \tag{9}$$

The resolved shear rate $\dot{\gamma}^\alpha$ is derived from the Orowan's law (equation (10)) that relies on the dislocation velocity v^α and the mobile dislocation density ρ_m^α for the system α.

$$\dot{\gamma}^\alpha = \rho_m^\alpha b v^\alpha \tag{10}$$

In the thermally activated regime, the dislocation velocity depends on both the temperature and the resolved shear stress τ^α as defined in equation (5).

To close the system the resolved shear stress τ^α is expressed as a function of the elastic transformation $\bar{\bar{F}}^e$, the second Piola-Kirchhoff stress tensor $\bar{\bar{\pi}}$ and the Schmid tensor $\bar{\bar{S}}^\alpha$:

$$\tau^\alpha = (\bar{\bar{F}}^{e\,T}\bar{\bar{F}}^e\,\bar{\bar{\pi}}) : \bar{\bar{S}}^\alpha \tag{11}$$

In reference (Portelette et al. 2018) the previous constitutive equations have been implemented in the *MFront* integrator (Helfer 2015) within the *Cast3M* code (Cast3M) including an implicit quasi-Newton algorithm for the nonlinear mechanical equilibrium and a standard implicit Newton scheme for the local

nonlinear behavior. An illustration of the stress localization induced by crystal anisotropy is given in Figure 14.

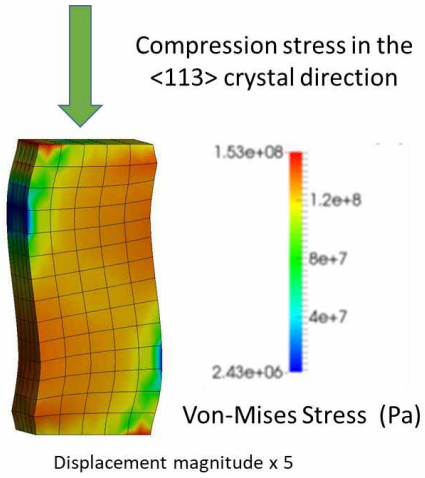

Figure 14 : Finite element result of a single crystal compression test showing stress localization in the specimen.

In reference (Portelette et al. 2018) material parameters of the gliding law (equation (5)) have been identified for the mode I and II through the Critical Resolved Shear Stress measured on single crystal compression tests. Experimental results selected for the identification are detailed in reference (Portelette et al. 2018) and the result of the fit is given in Table 7. In the latter, the mobile dislocation density ρ_m^α has to be considered as an empirical parameter of the Orowan's law (equation (10)) because the continuum mechanical plasticity model doesn't provide a balance equation for the mobile dislocation flux. In a second step, single crystal finite element simulation have been compared with experimental compression test in order to validate the plastic anisotropy and crystal rotation assessments. An illustration of the validation of the flow stress dependency on the crystal orientation is given in Figure 15 with the two slip modes I and II. In this case the plastic anisotropy is correctly assessed only when one of the two slip modes is activated. To improve the model, ½<110>{111} slip systems have been integrated based on several experimental observations. As a result, accounting for ½<110>{111} slip systems greatly improves stress predictions and lattice rotations in central part of the standard triangle but other orientations remain under debate. This suggests that ½<110>{111} slip systems may play an important role in UO_2 single crystal mechanical response and related lattice rotations. In particular, cross-slip, combined slip, and dislocation interactions appear as key processes to investigate in the future in order to better understand UO_2 single crystal mechanical properties.

	Mode I **½<110>{100}**	**Mode II** **½<110>{110}**
ρ_m^α (m^{-2})	$6.2\ 10^{12}$	$9.2\ 10^{11}$
ΔH_0^i (eV)	5.71	5.22
τ_0^i (MPa)	1.35	4.78

Table 7: Material parameters identified for the gliding laws of modes I and II.

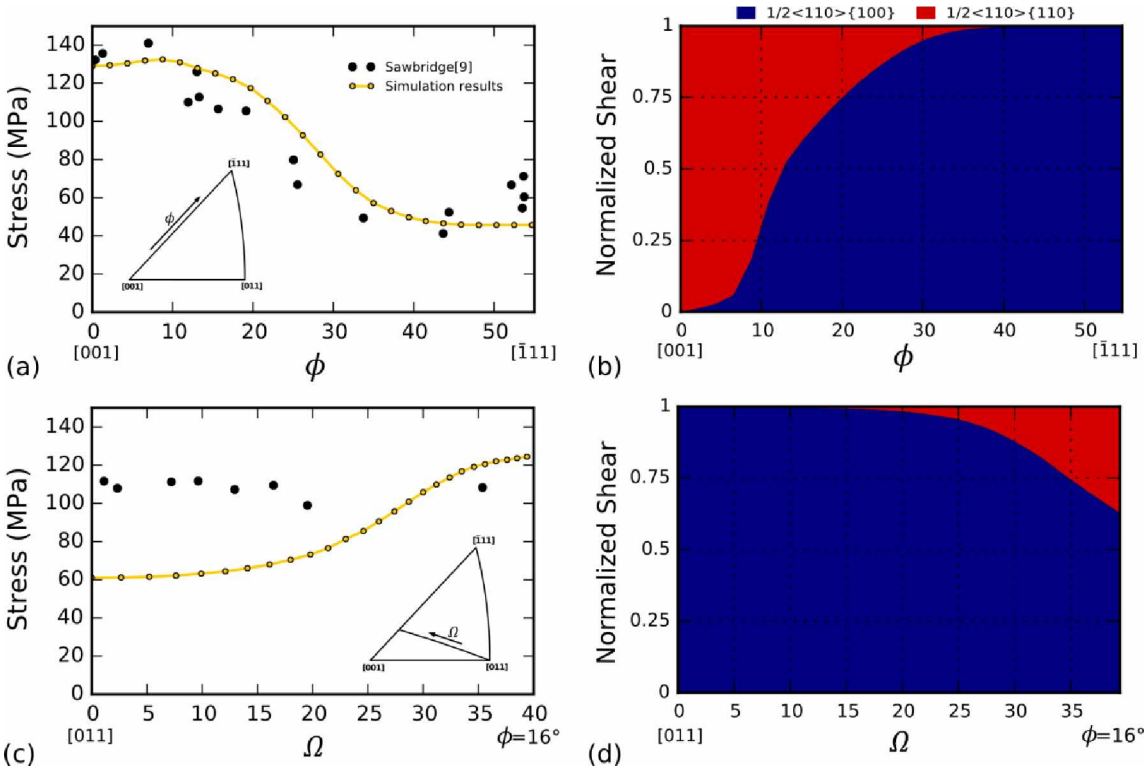

Figure 15 : Stress anisotropy. (a)-(c) flow stress at 2% strain versus ϕ and Ω orientations. (b)-(d) Computed normalized plastic shear contribution for each slip mode ($\gamma^{\{100\}}/\gamma_{tot}$ in blue and $\gamma^{\{110\}}/\gamma_{tot}$in red) versus ϕ and Ω orientations.

3.2 Elastic and plastic behavior of irradiated UO_2

To describe the effect of porosity on plastic behavior, a micro-mechanical model is derived in (Vincent, 2014a) for the effective plastic flow surface of irradiated uranium dioxide (UO_2). The microstructure of this material is simply modelled as a porous material. In the latter there are two populations of voids, or bubbles, of very different sizes subjected to internal pressures due to the presence of fission gases: the smallest bubbles are considered as intragranular and spherical in shape, whereas the largest bubbles located at the grain boundaries are considered as ellipsoidal and randomly oriented. Both types of bubbles can be subject to different pressures. During a postulated reactivity initiated accident, there is a strong increase of temperature in the fuel pellet which induces a thermal dilatation of the material and a strong increase of the pressures in the voids. A simple analytical expression of the effective plastic flow surface is obtained through a three-scale homogenization procedure (Figure 16). First, the small spherical bubbles are smeared out using a Gurson-like matrix (GTN model (Gurson, 1977), (Tvergaard, 1981), (Tvergaard, 1984)). Then, the intergranular ellipsoidal bubbles are smeared out, starting from one of the previous models derived in (Vincent, 2009a) and obtained by generalizing the limit-analysis procedure of (Gologanu, 1994) to compressible materials. A closed-form estimate of the effective plastic flow surface is derived motivated by the need of a model which can be accurate and computationally cost effective for structural calculations and parametric studies relative to the influence of bubbles on the overall response of the material. The general form of the pressure-sensitive effective plastic flow surface writes:

$$\frac{1}{\beta}\left(\frac{\Sigma_{eq}}{\sigma_o}\right)^2+\frac{1}{\alpha}\cosh\left(\frac{3}{2}\left(\frac{\Sigma_m}{\sigma_o}-\gamma\right)\right)-1=0 \tag{12}$$

where α, β, and γ are three functions of the parameters of the problem, namely the porosity of the spherical intragranular bubbles (f_b), the porosity and aspect-ratio of the oblate ellipsoidal intergranular bubbles (f_e and w), and the internal pressures of the intragranular and intergranular bubbles (p_b and p_e). Note that Σ_m is the macroscopic, or overall, hydrostatic stress and Σ_{eq} is the macroscopic von Mises stress, $\Sigma_m = 1/3\ \mathrm{tr}(\Sigma)$, $\Sigma_{eq}=\sqrt{3/2\ \Sigma_d : \Sigma_d}$, $\Sigma_d = \Sigma - \Sigma_m\ i$ is the deviatoric part of the overall stress Σ. In equation (12) σ_o denotes the overall yield stress of the unvoided matrix. The accuracy of this model is assessed by comparison with full-field numerical simulations (FFT-based method) in (Vincent, 2014b) and is presented in Section 3.5. Note that a semi-analytical model for the behavior of saturated materials containing two populations of voids of different sizes in the case of viscoplasticity is proposed in (Julien, 2011).

A poro-elastic model is proposed in (Haller, 2015), (Haller, 2016) for this material based on a single homogenization procedure and able to take into account for a size effect due to the spherical or ellipsoidal nanovoids. Indeed, molecular dynamics results of (Colbert, 2012) and (Jelea, 2011) exhibit a non-negligible surface effect on the effective elastic behavior for uranium dioxide at the intragranular bubbles scale, and especially for large surface/volume ratio of these bubbles. Thus, in (Haller, 2015), (Haller, 2016), existing micro-mechanical models ((Duan, 2005), (Brisard, 2010)) for materials with isotropic distribution of nano-sized spherical inclusions are extended to materials with two populations of pressurized bubbles, one relative to spherical bubbles and the other relative to ellipsoidal bubbles. The general framework of the so-called 'morphologically representative pattern-based approach' of (Stolz, 1991) is applied. The disturbed region around the bubbles is treated as an imperfect coherent interface (Gurtin, 1975) with a discontinuous traction vector across the interface and continuous displacement. The interface follows its own isotropic constitutive relation, different from that of the bulk, with its own surface bulk and shear moduli and surface tension. The model writes:

$$\Sigma = \left(3\ \tilde{k}\ J + 2\ \tilde{\mu}\ K\right) : E - \left(p_b\ B_b + p_e\ B_e - \gamma_b\ G_b - \gamma_e\ G_e\right) i \tag{13}$$

where E is the macroscopic strain, γ_b and γ_e are surface tensions applied on the spherical and ellipsoidal bubbles, J and K are the usual fourth-order projectors on hydrostatic and deviatoric symmetric tensors of second order. Then, $\tilde{k},\ \tilde{\mu},\ B_b, B_e, G_b, G_e$ are six functions of the parameters of the problem, namely the porosity and size of the spherical bubbles, the porosity, aspect-ratio, and size of the oblate ellipsoidal bubbles, the overall bulk and shear moduli of the unvoided matrix, the surface bulk and shear of the interfaces.

Note that the model presented above for the effective plastic flow surface does not take into account explicitly for the potential surface effects due to the nano-sized intragranular bubbles. However, the classical Gurson model for ductile porous media has been extended in (Dormieux, 2010) to incorporate the surface/interface stresses effect at the nano-scale. First, in (Dormieux, 2010), it is assumed that the strength of the interface can be described by a von Mises criterion. The q_1 and q_3 parameters entering the GTN criterion used in (Vincent, 2014a) for the first upscaling can be adjusted to recover the results of (Dormieux, 2010). The idea is to adjust these parameters so that the purely hydrostatic stress and the purely equivalent stress of (Dormieux, 2010) can be recovered with the purely hydrostatic stress and the purely equivalent stress of the classical GTN criterion. Second, concerning the surface tension γ_b, the result of (Dormieux, 2010) shows that it can be taken into account by a simple translation of the GTN yield surface along the hydrostatic axis, p_b being replaced by $p_b - 2\ \gamma_b / r_b$, where the size of the bubbles is

denoted by r_b. By doing so, the nanometric size of the intragranular bubbles and its surface effects on the yield strength can still be taken into account in the model of (Vincent, 2014a). The obtained q_1 and q_3 parameters depend on the porosity due to the intragranular bubbles and a new parameter $\Gamma = k_{int}/(r_b\,\sigma_o)$. Parameter k_{int} is the interfacial yield stress. Following an analysis of (Monchiet, 2010), this interfacial yield stress can be estimated as the thickness of the surrounding zone around the nano-bubbles with surface effects (i.e. the length of the interphase h) multiplied by the specific yield stress of the interphase $k_{int} = h\,\sigma_o^{interphase}$.
To summarize, the models presented above depend on the following *physical* parameters:

- the porosity and radius of the spherical intragranular bubbles,
- the porosity, aspect-ratio, and length of the oblate ellipsoidal intergranular bubbles,
- the internal pressures in the intra and intergranular bubbles,
- the overall yield stress of the unvoided matrix,
- the surface tensions applied on the intra and intergranular bubbles surfaces,
- the overall bulk and shear moduli of the unvoided matrix,
- the surface bulk and shear of the interfaces,
- the thickness of the surrounding zone around the intragranular nano-bubbles with surface effects (i.e. the length of the interphase),
- and the specific yield stress of the interphase.

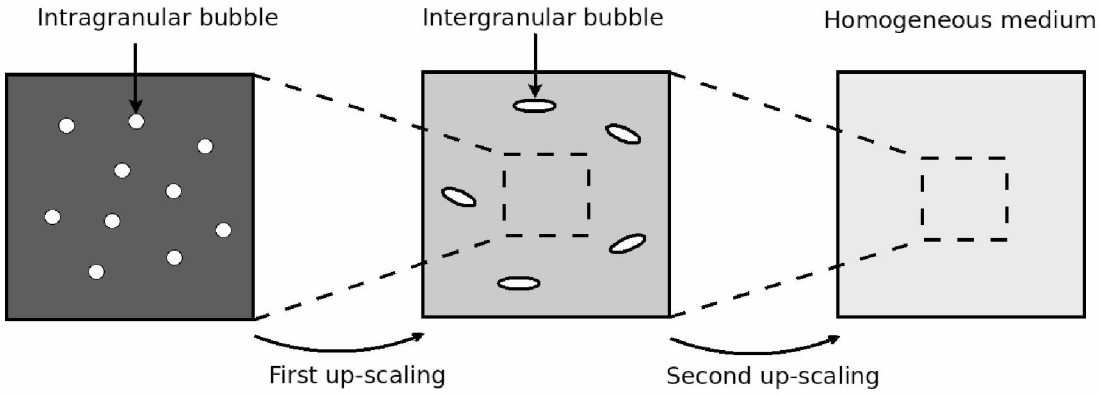

Figure 16 Homogenization procedure adopted in (Vincent, 2014a).

3.3 Bubble coalescence under thermal and pressure loadings

To assess microstructure modification induced by bubble coalescence under transient power loading, a model is proposed in (Vincent, 2009b). Coalescence of bubbles is modelled under the simultaneous action of high-pressure fission gases contained in the intra and intergranular bubbles together with hydrostatic thermal dilatation. A material with two populations of voids, small spherical voids located inside the grains and larger spheroidal voids located at the grain boundaries is considered. The ultimate stage of void growth is the coalescence of voids, which eventually lead to the formation of a macroscopic crack. Indeed, these macro-cracks formed by void coalescence can link together and induce a connected network of cracks through which fission gases may diffuse and reach the cladding. Thus, it appears that predicting void coalescence remains an important safety issue. A single grain is considered as a composite sphere: the inner core contains small spherical bubbles under pressure and the outer shell represents an interphase layer around the grain boundary that contains ellipsoidal oblate bubbles under pressure

aligned along the tangential direction (Figure 17). The inner core is modelled by a Gurson-like criterion (Gurson, 1977). The outer-shell behavior is modeled by the (Gologanu, 1994) model, which describes the effective plastic flow surface for a single oblate ellipsoidal void in a confocal ellipsoidal volume of von Mises matrix subjected to an axisymmetric strain-rate. An approximate resolution of the problem is obtained using the modified secant method (or the variational procedure of Ponte Castañeda, 1991). In the core and the outer shell, bubble coalescence is detected by Thomason-like criteria (Thomason, 1985). This composite grain model can be applied to detect transgranular versus intergranular failure. Thus, it is possible to discuss the dependence of the type of failure, transgranular versus intergranular, on the initial void volume fractions and on the applied pressures.

In addition to the *physical* parameters necessary for the model described in 3.2, the present composite grain model requires an estimate of the width of the grain boundary zone with respect to the average grain size.

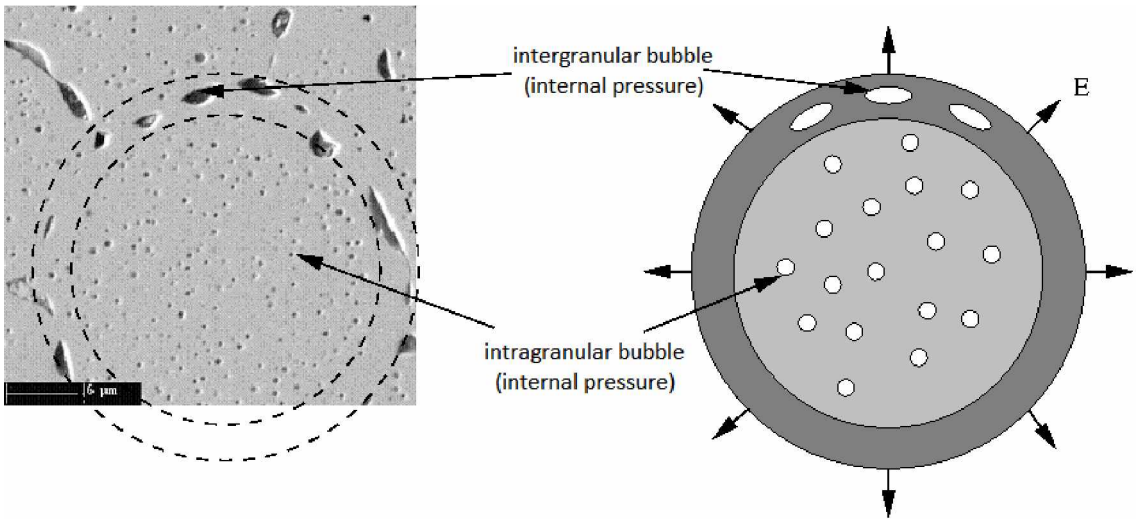

Figure 17: Idealized geometry of a grain. Illustration of the Composite Grain Model of (Vincent, 2009b).

3.4 Finite element simulation for the viscoplastic behavior of the UO_2 polycrystal

The effect of multiple grains microstructure has been investigated in the literature through micromechanics simulation based on a Representative Volume Element made of a polycrystalline microstructure (Delaire 2000, Barbe 2001, Raabe 2001, Sachtleber 2002, Aoyagi 2013, Schwartz 2013). These full field simulations have two main objectives: assess the homogenised macroscopic behavior knowing the single grain properties, and compute stress and strain heterogeneities induced by the microstructure. Homogenised properties are needed for engineering mechanical models, implemented in fuel performance codes, and can be drived from full field simulations. The latter can also be used for the interpretation of experimental results where the microstructure scale has to be understood with many details (among these situations there is for instance irradiation effects or fuel restructuration). Stress heterogeneities is also a key issue to assess microscopic fuel fragmentation or coupling effects between mechanical behavior and gaseous fission products swelling.

In reference (Portelette EMMCN 2018) a finite element approach has been proposed for UO_2 with a polycrystalline microstructure based on a Voronoi diagram. In the latter the generation of cell seeds used a random sequential algorithm with a repulsion distance in order to avoid too small edges on grain

boundaries. A periodic condition is prescribed in order to be able to use associated mechanical boundary conditions. Despite the use of a repulsion distance in the seeds generation algorithm some small edges remain. The latter have to be removed in order to avoid a prohibitive mesh refinement. In order to ensure the finite element mesh periodicity, itself needed for an easier implementation of the periodic displacement boundary conditions, a special algorithm has been developed with the Cast3M finite element code. Thanks to this algorithm each pair of nodes, of the associated periodic faces, respect the periodicity in the general case of a non-cubic volume element as shown in the Figure 18. In this algorithm, particular attention was paid to the small edges removal without losing periodicity.

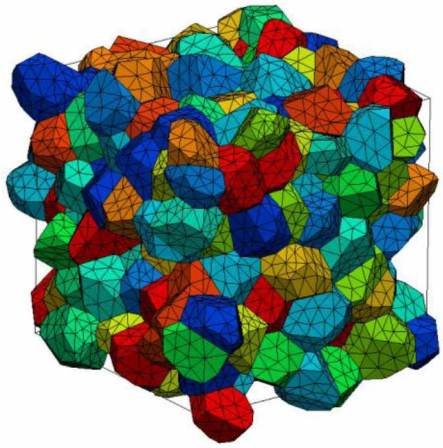

a) Cast3M finite element mesh

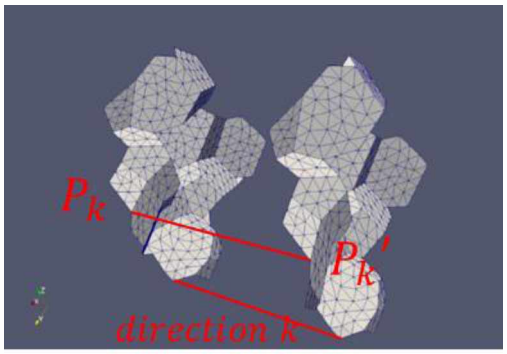

b) node periodicity of the polycrystal envelope

Figure 18 : Finite Element mesh for a periodic Voronoi diagram

Then periodic mechanical boundary conditions have been implemented with the constitutive equations (14) where PFD and PFC are two virtual nodes associated to the displacements of the periodic nodes P_k and $P_k{}'$ in each direction k. Displacements and forces of the virtual nodes are used to prescribe respectively the macroscopic strain and stress boundary conditions. The six degrees of freedom of PFD and PFC are used to address the six components of the symmetric second order tensor as given in equation (15).

$$\begin{aligned}
&\sum_{k=1}^{13} u_x(P_k') - u_x(P_k) - \left(\overrightarrow{P_kP_k'}.\vec{x}\right)u_x(PFD) - \left(\overrightarrow{P_kP_k'}.\vec{y}\right)u_x(PFC) - \left(\overrightarrow{P_kP_k'}.\vec{z}\right)u_y(PFC) = 0 \\
&\sum_{k=1}^{13} u_y(P_k') - u_y(P_k) - \left(\overrightarrow{P_kP_k'}.\vec{y}\right)u_y(PFD) - \left(\overrightarrow{P_kP_k'}.\vec{x}\right)u_x(PFC) - \left(\overrightarrow{P_kP_k'}.\vec{z}\right)u_z(PFC) = 0 \\
&\sum_{k=1}^{13} u_z(P_k') - u_z(P_k) - \left(\overrightarrow{P_kP_k'}.\vec{z}\right)u_z(PFD) - \left(\overrightarrow{P_kP_k'}.\vec{x}\right)u_y(PFC) - \left(\overrightarrow{P_kP_k'}.\vec{y}\right)u_z(PFC) = 0
\end{aligned} \qquad (14)$$

$$\begin{bmatrix} u_x(PFD) & u_x(PFC) & u_y(PFC) \\ & u_y(PFD) & u_z(PFC) \\ & & u_z(PFD) \end{bmatrix} \quad (15)$$

For mechanical computation the material behavior is defined with the single crystal law presented in section 3.1 according the local orientation of each grain. Initial grain orientation is defined with the material pole figure given by the Scanning Electron Microscope characterization. In the case of UO_2 pellets there is no material texture with a uniform distribution of the grain orientation in the pole figure. This isotropic material is obtained with equation (16) for the generation of each grain orientation.

$$\begin{aligned} \phi_1 &= F(0,2\pi) \\ \phi &= arcos(1 - 2F(0,1)) \\ \phi_2 &= F(0,2\pi) \end{aligned} \quad (16)$$

Where $F(x_1, x_2)$ is a uniform random distribution in the range $[x_1, x_2]$.

The inelastic strain incompatibility, induced by the orientation discontinuity at the grain boundary, is a result of the finite element computation where the local stresses and total strains are derived from the static equilibrium that includes the mechanical interaction between grains. Thanks to the finite strain formulation, presented in section 3.1, the crystal rotation induced by plasticity can be easily derived from the polar decomposition of the elastic transformation given in equation (17).

$$\bar{\bar{F}}^e = \bar{\bar{R}}^e \bar{\bar{U}}^e \quad (17)$$

Where $\bar{\bar{R}}^e$ and $\bar{\bar{U}}^e$ are respectively the elastic rotation and dilatation of the crystal lattice.

In order to assess the grain size effect Geometrical Necessary Dislocation and their associated hardening are computed with equations (18), (19) and (20).

$$\rho_{GND}^j = \frac{1}{b}\sqrt{\left(-\overrightarrow{grad}\gamma^j . \vec{s}^j\right)^2 + \left(\overrightarrow{grad}\gamma^j . \vec{e}^j\right)^2} \quad (18)$$

$$\tau_f^j = k_0 \mu b \sqrt{\sum_u a^{ju}\ \rho_{GND}^u} \quad (19)$$

$$v^j = v_D b \exp\left(-\frac{\Delta H_0^i}{k_b T}\right)\left(\cosh\left(\frac{\tau^j}{\tau_0^i}\right) - 1\right)\exp\left(-\frac{\tau_f^j}{\tau_0^i}\right) \quad (20)$$

Where j is the number of the gliding system, ρ_{GND}^j is the GND density, γ^j the resolved plastic shear strain, $\vec{s}^j$ and $\vec{e}^j$ are the unit vectors parallel to a screw and an edge dislocation lines respectively, τ_f^j is the

hardening resolved shear stress, a^{ju} are the coefficients of the dislocation interaction matrix and k_0 an empirical parameter.

The interaction matrix coefficients a^{ju}, used in the Taylor law (equation (19)), have been computed with Dislocation Dynamics simulation as presented in section 2.3.2. The GND hardening stress τ_f^j is introduced in the single crystal dislocation gliding law in equation (5) with a multiplicative term (see exponential function in equation (20)) which tends to reduce the dislocation velocity when the interactions increase.

In order to provide a macroscopic validation, a compression test under a uniaxial stress state has been simulated for the finite element polycrystal and compared with a compression experiment for a cylindrical fuel pellet. Simulation results and experiment/simulation comparison are illustrated in Figure 19. The latter shows that strain incompatibility at grain boundary leads to a significant stress heterogeneity which represents approximately 40% of the mean value. Experimental/computation comparison can be in a rather good agreement with the fit of only one supplementary coefficient k_0 compare to the material parameters defined with single compression tests (sec. 3.1). This coefficient k_0 is lower than one in order to reduce hardening induced by GND. At this stage the polycrystalline full field simulation can give a good assessment of the temperature and strain rate sensitivity with material parameter fitted on single crystal tests. This last aspect is the key point to enable the link with elementary mechanism at lower scales and to have a physically based model. However, the full field simulation is not yet predictive enough to explain the scatter of experimental results.

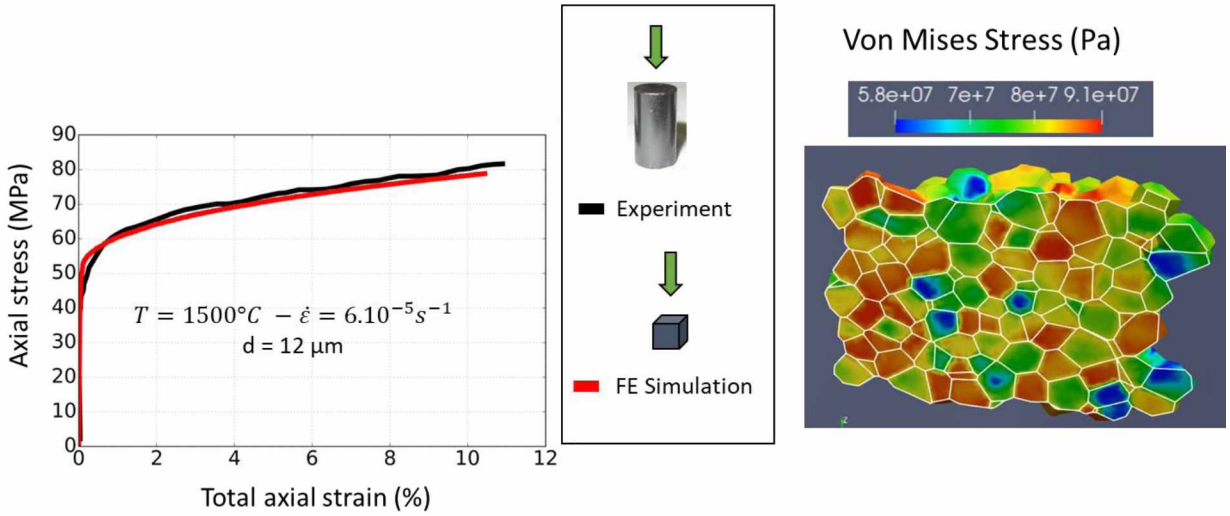

a) Stress-strain curve b) Stress heterogeneity

Figure 19 : Simulation of a compression test : Macroscopic validation

In order to analyse the validity of the stress heterogeneity assessment and to understand the physical meaning of the empirical coefficient k_0, a microscopic scale validation has been proposed. The main idea is to use the experimental measurement after a compression creep test of the crystal rotation induced by plasticity in each grain in order to compare it with simulation and then have an indirect validation of the strain and stress heterogeneities in the polycrystal. The crystal rotation induced by plasticity has been measured in reference [Ben Saada 2017] with an EBSD characterization of sub-grain boundaries as a function of the creep strain prescribed at the end of the compression test. A sub-boundary is defined as a low disorientation between regions inside the primary grain as illustrated in Figure 20a). These intra-

granular disorientations can be compared to the gradient of the elastic crystal rotation (see Figure 20b)) computed with the finite strain formulation in the polycrystal simulation.

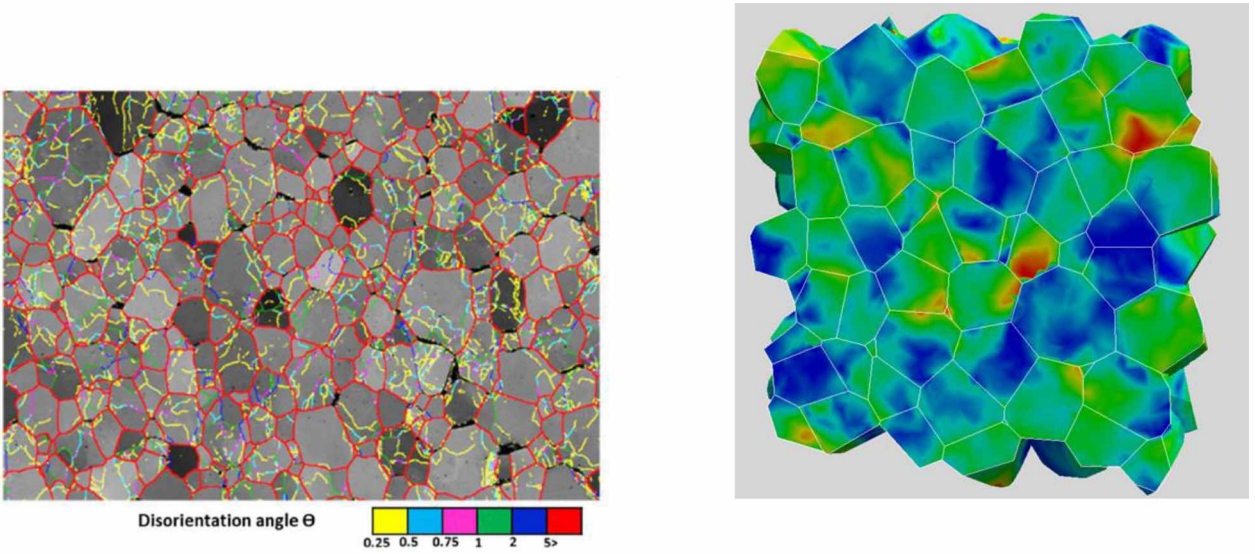

a) Sub-grain boundary measurement [Ben Saada 2017]

b) FE computation of the elastic crystal rotation inside grain [Portelette 2018]

Figure 20 : Polycrystalline full field simulation: Validation at microscopic scale

In order to have the same statistical measurement of the disorientation for 2D experiment results and 3D simulation results the normative function $\overline{\Delta\theta}_{max}(C_d)$ presented in Figure 21 has been proposed.

The first results lead us to the conclusion that the 3D simulation overestimates the experimental crystal disorientation with a ratio of approximately 2.5 as plotted in Figure 21. Then, it was concluded that the GND density is also overestimated, which is consistent with the empirical parameter $k_0 = 0.2$ needed to reduce the stress hardening induced by dislocations interaction. At this stage, it is still difficult to explain why the crystal curvature is higher in the computation than in the EBSD measurement. The main point under investigation is to complete the single crystal model with the mode III gliding systems (Sec. 3.1) which were not included in these polycrystalline computations.

$$\overline{\Delta\theta}_{max}(C_g) = \max_{(i,j)\in C_g} \Delta\theta(i,j)$$

C_g set of pixels (i,j) located inside a primary grain

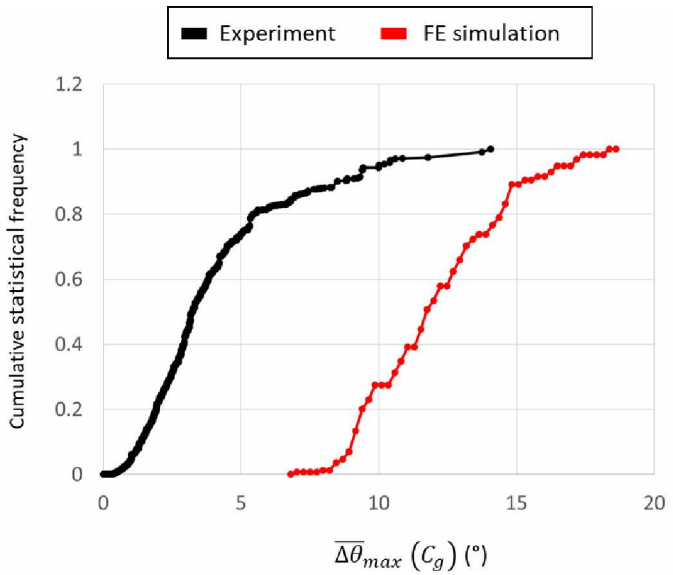

a) Statistical measurement b) Experiment/computation comparison

Figure 21 : Crystal disorientation after a compression creep test ($T = 1500°C$, $\dot{\varepsilon} = 8.10^{-5}s^{-1}$, $\varepsilon_{max} = 11\%$)

3.5 Fast Fourier Transform simulation

The Fast Fourier Transform method is a powerful tool to achieve a full field simulation of a complex microstructure such as multiple grains with intra and/or inter granular porosities. This method was originally developed by (Moulinec, 1994) to determine the local and overall responses of non-linear composites. It requires no meshing, the model geometry being described by an image composed of voxels in 3D, or pixels in 2D. In (Vincent , 2014b), FFT full-field simulations were proposed to validate a homogenized model such as the GTN-type approach presented in section 3.2. This FFT-based method is applied to voided materials with a Gurson matrix where the voids are subjected to internal pressure. Different microstructures containing a large number of spherical or ellipsoidal voids, up to 511 voids, are considered to ensure a certain level of isotropy and representativeness. Different triaxialities for the loading and different bubble pressures are considered. The agreement with the model is found to be very satisfactory. An example of typical microstructure involved in this work is shown in Figure 22, together with a comparison between FFT simulation and analytical model.

Then, in (Boittin , 2017), the specific effect of the spatial distribution of the intergranular bubbles on the effective plastic flow surface has been studied in more details. The mean size of the grains is fixed and different microstructures are generated varying the volume fractions and sizes of the intergranular bubbles. An example of typical microstructure is shown in Figure 23. The effect of the intragranular voids is still modelled through a GTN criterion in the matrix. Three particular loading conditions are successively imposed on these microstructures controlling the overall stress direction: a purely hydrostatic tension, a purely deviatoric axisymmetric loading, an intermediary axisymmetric solicitation with a high, but finite, stress triaxiality ratio. A comparison is performed with the analytical model presented in 3.2 and a correction of the porosity relative to the intergranular bubbles is introduced in this analytical model in order to take into account the specific distribution of the intergranular bubbles along the grain boundaries. On one hand, it is shown that the relative size of the bubbles has a significant influence on the effective plastic flow stress for a purely hydrostatic stress loading. On the other hand, it is observed that the relative size of the bubbles has a less important influence on the effective plastic flow stress for a purely deviatoric axisymmetric stress loading. Typical aspects of the local plastic strain field for a purely

hydrostatic loading and an axisymmetric purely deviatoric loading are shown in Figure 24. For the purely hydrostatic case, the plasticity is located along the grain boundaries. For the purely deviatoric test, some plasticity also develops inside the grains.

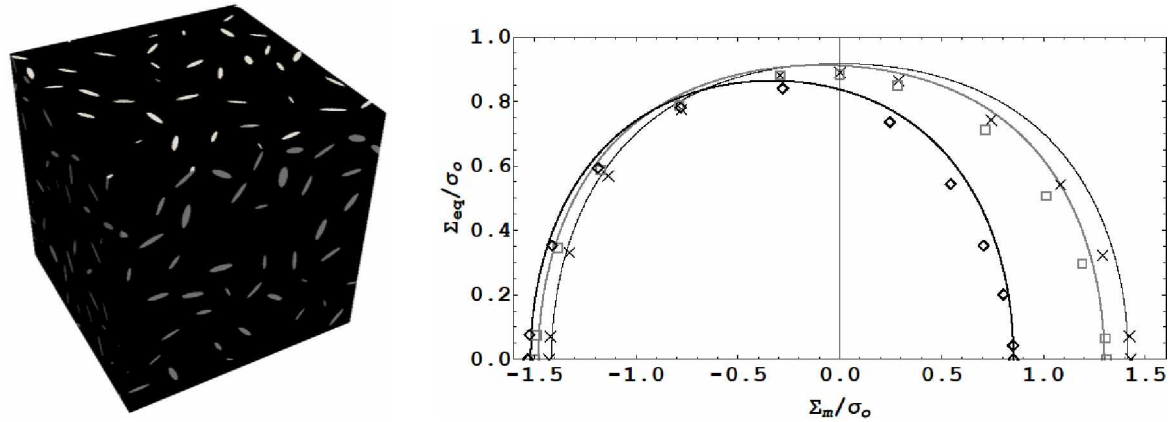

Figure 22 Left (Vincent , 2014b): example of microstructure used in the FFT-based numerical simulations of 511 randomly oriented and distributed voids (gray) in the matrix (black), porosity 4%. The image is discretized with 512x512x512 voxels. Right: effective plastic flow surface. Lines: analytical model with $f_b = 0.02, f_e = 0.04, w = 1/5, p_e = 0$. Symbols: FFT results. Thin black: $p_b = 0$, Gray: $p_b = 0.5\ \sigma_o$, Thick black: $p_b = 1.5\ \sigma_o$.

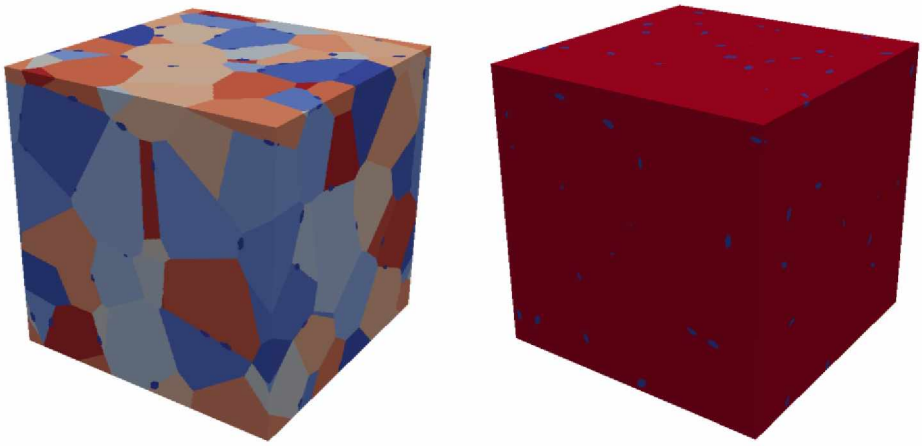

Figure 23 : Generation of microstructures in (Boittin , 2017). Left: elongated voids (dark blue) are progressively inserted between grains (each grain is assigned a distinct color). Right: corresponding two-phases microstructure with elongated voids (dark blue) in an isotropic Gurson-like matrix (red).

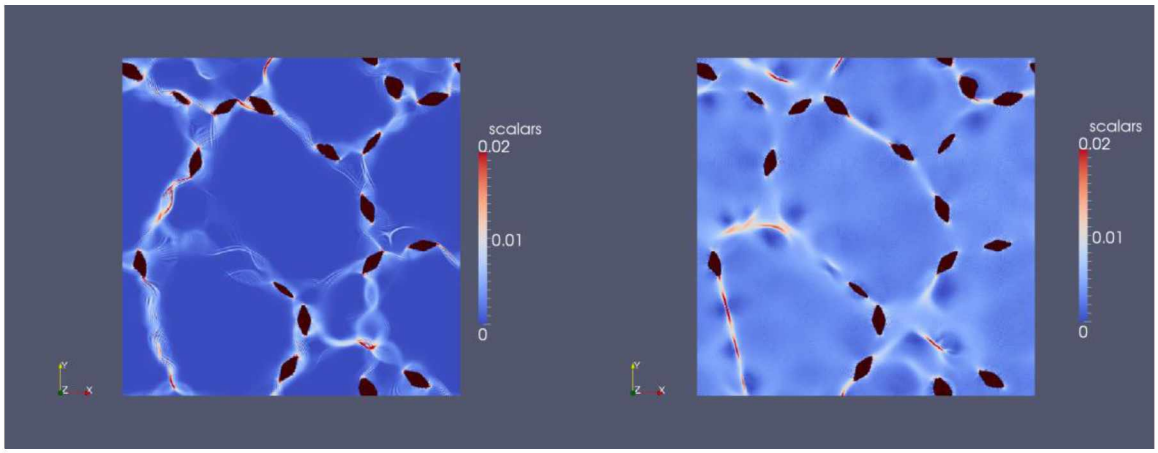

Figure 24 : Two slices of a microstructure with 21 grains from (Boittin, 2017). Cumulated plastic strain fields in the matrix. Left: purely hydrostatic overall stress. Right: purely deviatoric overall stress ($\Sigma_{33} = -2\,\Sigma_{11} = -2\,\Sigma_{22}$ and $\Sigma_{12} = \Sigma_{13} = \Sigma_{23} = 0$). Scale adapted to visualize values between 0 and 0.02.

In (Wojtacki , 2020), a new model is derived for the secondary creep of irradiated MIMAS MOX fuel at high temperature. The objective is to estimate both numerically and analytically the effect of clusters of voids due to irradiation on the overall strain rate. The microstructure is simply modeled as an isotropic matrix, weakened by randomly distributed clusters of spherical pores. The behavior of the matrix is described by two power-law viscosities corresponding to two different creep mechanisms. The local fields and overall response of such microstructures are simulated using a FFT-based method. The largest microstructure contains 13 clusters each of them gathering 1563 voids (see Figure 25). These numerical results are confronted with a new analytical model based on appropriate approximations of the effective potential for the overall response of porous materials under creep. The agreement is found to be quite satisfactory. In large Pu-rich clusters, specific porous polycrystalline microstructures can be encountered with similar sizes for pores and grains. In (Portelette , 2022), such microstructures are simulated in order to estimate the effect of the anisotropy due to the grains surrounding the pores on the overall viscoplastic behavior. Two distinct shapes of pores (spherical and polyhedral) and two relative sizes of the voids with respect to the grains are considered. A crystal plasticity model developed by (Portelette , 2018) for UO_2 is used to describe the local deformation of the grains with dislocation glide mechanisms and adjusted to fit with existing experimental results on MOX fuel. FFT-based full-field simulations are performed varying the temperature, strain rate, porosity, pore shape, relative size of pores with respect to grains, and stress triaxiality. It appears that the effect of the relative size of pores remains small for microstructures with spherical voids, thus indicating a minor effect of the crystallinity and the anisotropy of the grains on the overall viscoplastic response. The effect of the relative size of pores is more pronounced for microstructures with polyhedral voids and increases with stress triaxiality. It is observed that the behavior of the microstructures with polyhedral voids tends to the behavior of the microstructures with spherical voids when the relative size of pores with respect to the size of grains increases. Moreover, it is observed that the results obtained in the case of polyhedral voids when the size of voids is equal to the size of grains can be estimated from the case of spherical voids by multiplying the porosity by a constant $q \approx 1.3$. Thus, multiplying the porosity by q in the analytical model of (Wojtacki , 2020) leads to an estimate when the pores are polyhedral with a size close to the size of grains.

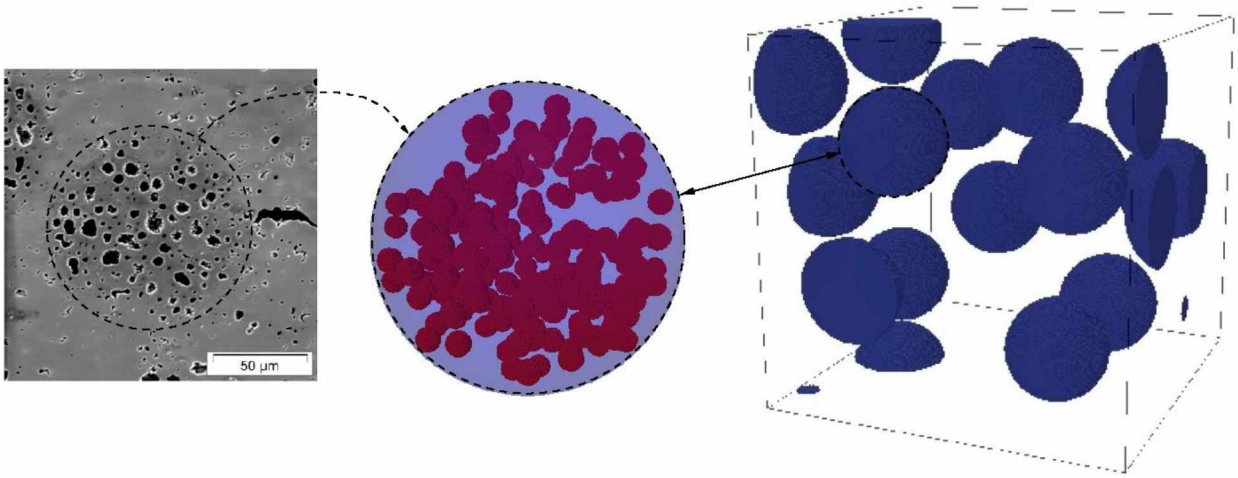

Figure 25 : Example of microstructure used in the FFT-based simulations of (Wojtacki , 2018): irradiation bubbles in the Pu-rich clusters for a MIMAS MOX fuel.

4 Crack initiation and rupture

During the first power increase, fuel pellets fracture into several pieces (primary cracks) because of stresses resulting from the thermal gradients and consequent expansion. Under transient conditions, sudden temperature increases can induce a secondary crack pattern on the external part of the pellet. These cracks have a direct impact on the circumferential stresses transmitted to the clad under the mechanical interaction with the pellet. Moreover, under accident conditions (LOCA, RIA), an over fragmentation of the pellet can be observed. The fragments size is one of the key parameters involved in the management of the accident.

During reactor operation, it can be expected that the fracture strength of the fuel will decrease due to the generation of dislocation loops and fission products, fission gas bubble formation, etc. Fission gas accumulates during irradiation, stabilising intragranular defects and forming intergranular bubbles. Intergranular bubbles coarsen, interlink, and eventually and may vent to the fuel periphery (White and Tucker 1983, Rest 1984, Kogai 1997, White 2004, Pastore et al. 2013, Tonks 2018, Prudil 2020). However, bubbles focus elastic stresses leading to crack initiation and can form intergranular crack pathways.

The fracture of unirradiated polygranular UO_2 has been explored experimentally by various researchers [Evans 1969, Roberts 1972, Solomon 1972, Igata 2973, Radford 1979, Oguma 1982]. The primary conclusion is that UO_2 experiences brittle fracture at low temperature, with a ductile to brittle transition at about 1200°C [Evans 1969, Roberts 1972]. Various studies have shown that grain size has a minor impact on the fracture strength [Evans 1969, Igata 1973, Radford 1979, Oguma 1982], with most finding that the fracture strength varies with the inverse square root of the grain size. Porosity has been shown to have a much more significant effect [Roberts 1972, Radford 1979, Oguma 1982], though there is disagreement on the best means of quantifying the impact. Impurities have also been shown to impact the fracture strength [Solomon 1972].

There is little experimental data quantifying the change in fracture strength of irradiated fuels, due to the difficulty in carrying out mechanical testing on radioactive samples. However, there have been a number of efforts looking at the fragmentation of irradiated fuel during reactor transients and accident conditions [Cronenberg 1979, Kulacsy 2015, Jernkvist 2020]. Some efforts have been made to include embrittlement

of the fuel with burnup in fuel performance codes [Gatt 2015], but typically fuel embrittlement with burnup is not included.

A complimentary approach to quantifying the impact of changes in the fuel microstructure on its fracture strength during reactor operation is prediction through mechanistic, micro-mechanical simulations, as discussed in this section. These simulations employ the results of the lower length scale calculations in Sec. 2.2 and progress from the mesoscale, through grain-scale, and to a full macroscopic treatment. In order to perform such a multiscale investigation, the criteria for fracture must first be clarified.

4.1 Fracture criteria

A multiscale micro-mechanical rupture model must include the effects of irradiation, pressurized bubbles, and grain boundaries or a range of sizes from nanometers up to micrometers. The results may then be incorporated into macroscale treatments, e.g., for other inelastic strains in the fuel via a smeared crack approach (see for instance (Jernkvist 1997, Michel et al. 2018).

The multiscale model should also reconcile with ongoing experiments at the macro and micro-scale. Available rupture stress experimental values of fuel are mainly derived from macroscopic tests with bending specimen size of a few millimetres whereas recent experimental works include SEM in-situ rupture test and microscopic specimen characterization (Henry et al. 2019). Reconciliation of macro- and microscale data, and incorporation into a multiscale modelling treatment leads to the question of scale transition of the rupture properties.

Fragile rupture in a homogeneous elastic material can be described by two parameters, the maximal stress and the dissipated energy per unit surface, related to fracture initiation and crack extension respectively. The rupture stress criterion and the elastic energy release rate, or Griffith criterion are described by equations (21) and (22) respectively.

$$\sigma_I > \sigma_R \tag{21}$$

where σ_I is the maximal principal stress for mode I failure and σ_R is the rupture stress.

The elastic energy release rate, or Griffith criterion is ,

$$G > G_C \tag{22}$$

where G is the elastic energy release rate per unit surface and G_C is the critical value past which it is energetically favourable for the crack to grow.

The rupture stress criterion in Eq (21) is size-dependent because it characterizes both the material toughness and the statistical distribution of defects. Consequently, experimental measurement of the rupture stress have to be done on a test specimen with a size representative of the scale addressed in the stress computation to be used in the rupture criterion. If it's not possible to have a representative size a scale transition factor can be derived from the defect statistical distribution as it is proposed for instance in a Weibull model [Weibull51]. However, extrapolation of a scale transition factor for a large range of sizes is fraught with uncertainty.

The Griffith criterion in Eq. (22) is scale-independent and can predict the size effect, but to compute the elastic energy release rate a description of the geometrical stress singularity at the origin of the crack

extension induced by material defects is needed. The energy release rate is related to the dissipation of the stress at and around the crack tip compared to the creation of surface, as described by the stress intensity factor, K.

For this reason, the micro-scale tests have been devoted to measuring the material toughness with a notched bending specimen as shown in Figure 26b. Due to the specimen size and geometry finite element modelling has been used to assess the material toughness with experimental measurement of the rupture load P_R. One first computes an equivalent elastic rupture stress based on the analytical solution of a smooth bending cantilever shown in Figure 26,

$$\sigma_R^{elastic} = \frac{P_R . L . z}{I_G} \tag{23}$$

where I_G is the inertia moment, z is the maximal distance to the neutral fiber in the cross section, P_R the rupture loading measured during test and L is the length of sample.

Then the toughness is given by,

$$K_c = A(x)\sqrt{d}\sigma_R^{elastic} \tag{24}$$

$$A(x) = \frac{\sqrt{x}[1.99 - x(1-x)(2.15 - 3.93x + 2.7x^2)]}{(1+2x)(1-x)^{3/2}} \tag{25}$$

where $x = \frac{d}{t}$ and d is the notch size, t the specimen thickness, K_c is the critical value of the Mode I stress intensity factor, and $A(x)$ is a shape function (Anderson 2017) derived from the stress intensity factor computation for a Single Edge Notch Bending specimen. An example of the Finite Element mesh used in (Henry 2019) to verify equation (24) is shown in Figure 26a.

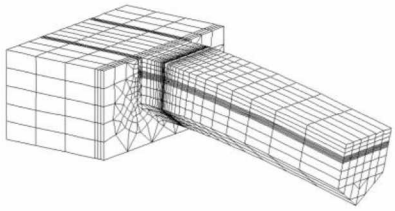

a) Finite element computational mesh

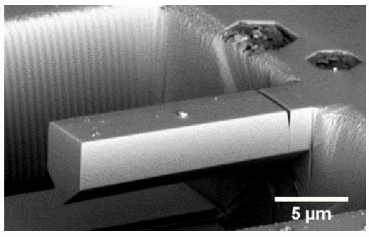

b) SEM image - Microscopic notched cantilever of fresh UO_2

Figure 26 : Micro bending test specimen for small-scale fuel rupture properties characterization.

The critical stress intensity factor has been evaluated on notched microscopic sample and is consistent with the macroscopic testing (Gatt 2015). At microscopic scale, the size of the sample being smaller than the grain size, tests in different crystalline plane orientations have been performed. These tests give the critical stress intensity factor for the differrent crystalline plane targeted. These results compared with macroscopic bending tests confirm that the material toughness is scale independent and can be used at both scales through the Griffith criterion.

4.2 Crack initiation induced in bubbles pressurized by fission gases

Considering SEM micrographs of bubbles induced by irradiation in fuels (see Figure 27) it seems obvious that the geometry is anything but spherical. The radius of curvature varies significantly along the gas-solid interface, which motivates a systematic study of the effects of bubble geometry on facture criteria.

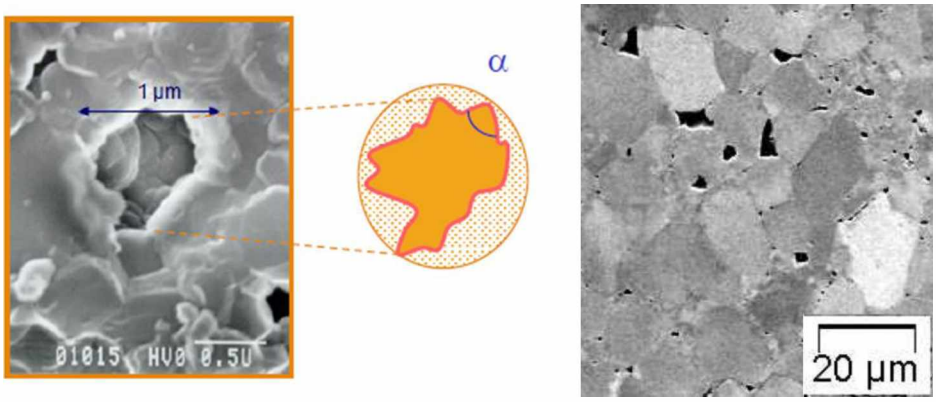

A) B)

Figure 27 : Sample SEM micrograph of intergranular bubbles in iraddiated fuels : A) in the restructured HBS zone (Baron et al. 2003) and B) in the initial microstructure (Noirot et al.2004).

4.2.1 Geometrical description of intergranular bubbles

A study of the effect of fission gas bubble pressure on grain boundary cracking and separation using finite element (FE) modelling at the scale of fuel grains was performed in (Chakraborty et al. 2014). In particular, a criterion for the onset of unstable crack growth from a grain-boundary bubble was sought. First, the role of grain misorientation, which can affect the grain boundary fracture behavior through elastic anisotropy and surface and grain boundary energies was addressed through explicit 3D crack growth FE simulations using the cohesive zone model. Results demonstrated that elastic anisotropy had a negligible effect on the critical bubble pressure for crack initiation. Following this observation, subsequent analyses were performed considering isotropy and axial symmetry. Specifically, 2D FE simulations using the J-integral approach (Rice 1968) of Mode-I crack growth along the grain boundary plane ahead of a lenticular bubble were carried out. Through the simulations, a functional form that relates the stress intensity factor to the bubble pressure, the bubble size and the fractional grain-boundary bubble coverage (fractional coverage) was derived. On this basis, an expression was obtained for the critical bubble pressure for crack initiation, which can be used in engineering-scale models to evaluate grain boundary separation and the associated fission gas release. Both cases of (a) gas pressure acting on the cracked faces and (b) pressure-free cracked faces were considered. In the following, the main results focusing on situation (a) are summarized.

A schematic of the axisymmetric FE model is shown in Figure 28. A constant bubble semi-dihedral angle of 50° was considered. A condition of zero displacement parallel to the grain boundary was prescribed on the far boundary to consider the effect of adjacent bubbles. Through the calculations, a functional relationship between a non-dimensional stress intensity factor (similar to Newmann 1971, Tada et al. 2000) which includes the geometric effect, F, and the crack length, a, was evaluated. Then, F at crack initiation, F_c, was obtained by extrapolation to a=0. By varying the box-size, W, to consider different values for the fractional coverage, A_f, a correlation between F_c and A_f was derived. The effect of the hydrostatic stress in the fuel was accounted for by modifying the stress intensity factor using the principle of superposition (Tada et al. 2000) for the configurations of (i) a pressurized bubble in a stress-free medium and (ii) a pressure-free bubble in presence of hydrostatic stress. Then, the critical bubble pressure for crack initiation was obtained as

$$p_c = \frac{K_c}{F_i\sqrt{\pi R}} + \sigma_h \tag{26}$$

where p_i is the critical bubble pressure, R the bubble projected radius on the grain boundary, σ_h the hydrostatic stress (positive if the medium is under compression), and

$$K_c = \sqrt{\frac{G_c E}{1-\nu^2}} \tag{27}$$

Here, G_c is the critical energy release rate or grain boundary cohesive energy, E the Young's modulus and ν the Poisson's ratio. For E=385 GPa, ν=0.23, G_c=1 J/m^2 (Govers et al. 2007) and σ_h=0, the bubble pressure for crack initiation as a function of the fractional coverage is obtained as illustrated in Figure 29. The comparison between the constrained far boundary assumption and an infinite boundary assumption (e.g., Newmann 1971, Tada et al. 2000) is also shown in Figure 29. More details and results for situation (b) can be found in (Chakraborty et al. 2014).

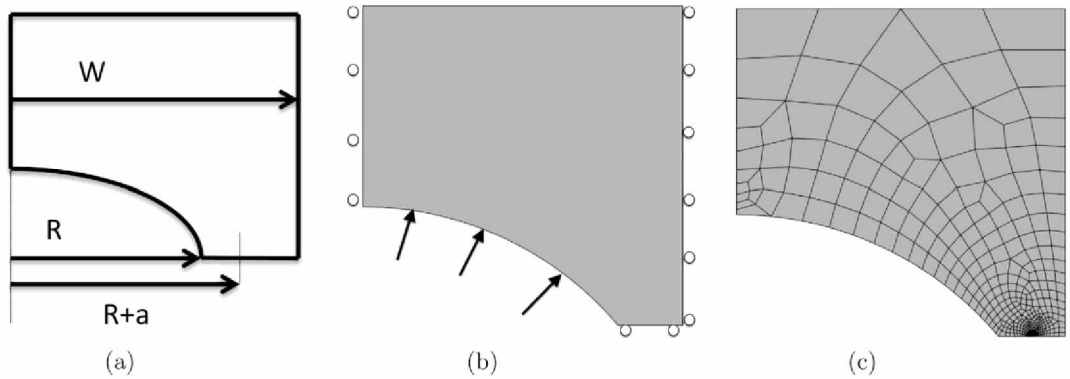

Figure 28: Axisymmetric model of pressurized lenticular bubble: (a) geometric parameters, (b) loading and boundary condition, (c) FE mesh. Figure taken from (Chakraborty et al. 2014).

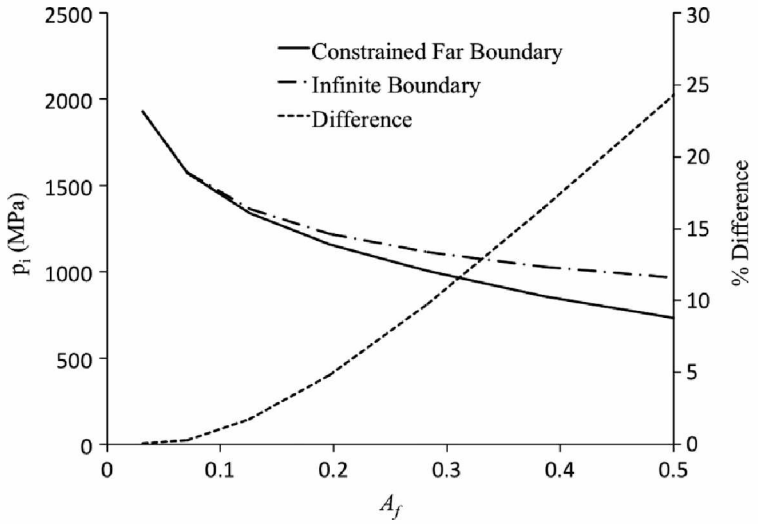

Figure 29: Bubble pressure at crack initiation, p_i, as a function of the fractional grain-boundary bubble coverage, A_f. Comparison with the result obtained using an infinite boundary assumption is included. Figure taken from (Chakraborty et al., 2014).

4.2.2 Sensitivity of rupture criterion to bubble shape

A complementary approach to that of Sec. 4.2.1 considers the nonspherical bubble and the crack geometry slightly differently. Another treatment of the geometric effects of representative bubbles strives to generalize to the 3D case. In the 3D finite element simulation of the porous microstructure presented in 4.4, it is computationally intractable to have a mesh refinement consistent with the method presented here to compute the elastic energy restitution rate for all the bubbles. Then to be able to simulate crack initiation in a 3D finite element mesh with spherical bubbles, an effective rupture stress is derived from a simpler model.

The shape singularity, associated to the bubble's non-spherical geometry, can be analysed through the simplified model proposed in Figure 30a. This model considers that the bubble shape is a cone defined with two parameters r_b and α. In order to be able to compute the elastic energy restitution rate associated to the shape singularity, an initial crack of size a is added at point B [Chakraborty2014]. The fission gas pressure loading is prescribed through a stress boundary condition on the bubble surface. Then the equivalent elastic energy restitution rate of the singular bubble is derived from the asymptotic result obtained when the crack size a tends toward zero [Chakraborty2014].

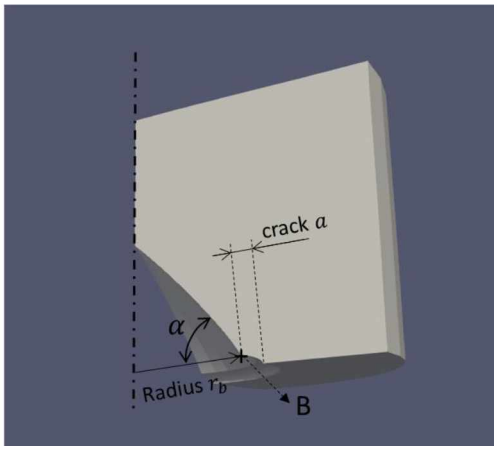

a

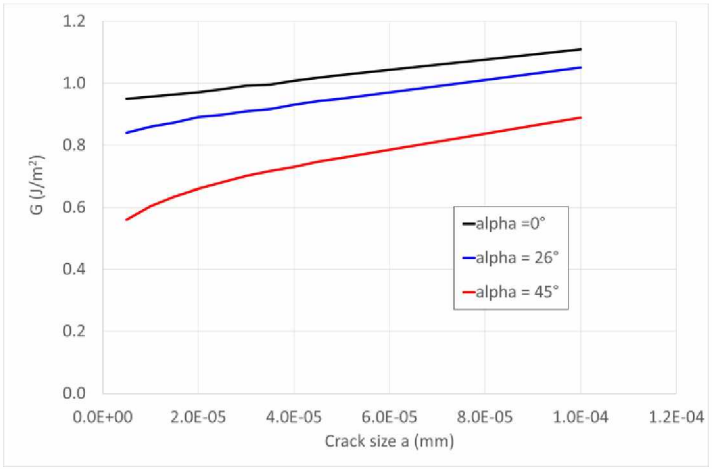

b

Figure 30 : a) Geometrical model of the bubble shape singularity, b) Computation of the elastic energy restitution rate with the Cast3M finite element code $(singular\ bubble\ r_b = 1\ \mu m, presure = 400\ MPa)$.

The elastic energy release rate is computed with the Cast3M finite element code (Cast3M) and a 2D axisymmetric mesh of the singular bubble of Figure 30a. The contour integral G is assessed with the virtual extension method (Moran&Shih 1987) through the G_THETA procedure of the Cast3M code. An example of the results obtained for a bubble radius $r_b = 1\ \mu m$ and an internal pressure of 400 MPa are given in Figure 30b. The asymptotic value of G is greater than 0 when the parameter a tends towards a small value, which confirms that the proposed bubble shape leads to a stress singularity near the point B. Values of G are respectively estimated at 0.5, 0.8 and 0.95 for $\alpha = 45$, 26 and 0. The geometry for $\alpha = 0°$ is

similar to a real crack, so it is concluded that the stress intensification for a real crack is twice higher than for a singular bubble with $\alpha = 45°$.

In equation (29) an analytical solution has been proposed to compute the internal bubble pressure at crack initiation for a singular bubble shape. This solution is derived from the equation (28) (analytical solution given by (William 1957) for a penny shape crack and the superposition elastic principle) and equation (27).

$$K_C = \frac{2}{\pi}.\,p_c.\sqrt{\pi.r_b} \tag{28}$$

with

$$p_c = \frac{1}{2}\sqrt{\frac{G_c \pi E}{r_b f(\alpha)(1-\nu^2)}} \tag{29}$$

where r_b is the penny shape crack radius (similar to the bubble radius), p_c the internal bubble pressure at crack initiation and $f(\alpha)$ is a shape function of the singular bubble. Eq. (29) is comparable to Eq. (26) for the different bubble geometry.

The expression of the effective rupture stress, needed to assess crack initiation when the singular bubble shape is simplified with a spherical shape assumption, can then be derived from the maximal tangential stress in a spherical bubble submitted to a pressure p_c,

$$\sigma_R^{eff} = \frac{p_c}{2} \tag{30}$$

This prediction of Eq (29) is in good agreement with finite element results as shown in Table 8 alongside the values of the effective rupture stress from Eq. (30) for a critical elastic energy restitution rate of 1 J/m^2. One can observe that this effective rupture stress includes a size and a shape effect, consistent with the Griffith criterion, which can be used to improve the results in the case of a spherical bubble shape assumption. This solution can be easily used in a fuel performance code to assess crack initiation induced by pressurized bubbles according a Griffith criterion.

The comparison of this effective rupture stress to the one measured at macroscopic scale in a bending test has to consider a material with the same critical elastic energy restitution rate. This kind of comparison can be useful to understand the defects size effect, needed to transpose the rupture stress parameter from the macroscopic scale to the microstructure scale.

$r_b\ (\mu m)$	$G_c\ (J/m^2)$	α	$f(\alpha)$	$p_{c_{EF}}\ (MPa)$	$p_{c_{analytic}}\ (MPa)$ equation (29)	$\sigma_R^{eff}\ (MPa)$
1	1	45	5.42E-01	5.61E+02	5.64E+02	2.82E+02
1	1	26	8.87E-01	4.38E+02	4.41E+02	2.21E+02
1	1	0	1	4.13E+02	4.15E+02	2.08E+02
2	1	0	1	2.92E+02	2.94E+02	1.47E+02

Table 8 : Internal bubble pressure at crack initiation for a singular shape: comparison between finite element computation and analytical solution.

4.3 UO_2 fracture strength as a function of porosity and grain size: phase-field rupture approach

Various computational approaches have been applied to model discrete crack propagation in polygranular UO_2, including cohesive element models [Gatt2015,Williamson2009], the discrete element method

[Huang2014], the extended finite element method [Jiang 2020], and peridynamics [Oterkus2017,Wang 2018], but they have been primarily applied at the pellet scale. The phase-field fracture method has been applied to model UO_2 fracture at the mesoscale, including the impact of grain structure and porosity [Chakraborty2016, Jiang2020]. This section summarizes efforts to apply the phase-field fracture model to quantify the impact of fission gas porosity on the fracture strength of UO_2 in 2D and then in 3D.

In the phase-field fracture method, cracks are represented by the values of a continuous variable field, often called d. When $d = 1$, the material is cracked and when $d = 0$ the material is intact. The field smoothly transitions between these values, such that $0 < d < 1$ represents damaged material that has not fully cracked. This smooth transition between values causes the cracks to have a finite width. The variable field is evolved to minimize the stored energy in the material. Phase field fracture models were first introduced about twenty years ago [Grancfort 1998, Bourdin 2000, Bourdin 2008], and have continued to grow in popularity.

In phase-field fracture models, the total energy of the material F results from mechanical deformation and from the surface energy of cracks according to the equation

$$F = \int_V \left(f_{def}(d) + f_{crack}(d, \nabla d) \right) dV \tag{31}$$

where,

$$f_{def} = ((1-d)^2 + k)\psi^+ + \psi^- \tag{32}$$

is the deformation energy density, and

$$f_{crack} = g_c \left(\frac{d^2}{2l} + \frac{l}{2} |\nabla d|^2 \right) \tag{33}$$

is the crack energy density, ψ^+ is the portion of the deformation energy density that contributed to fracture, ψ^- is the portion that does not, k is a small scalar constant that improved numerical performance, g_c is the energy release rate of the material, and l is a model parameter that defines the finite width of the cracks [Chakraborty2016, Jiang2020]. The parameter g_c is related to G_c the dependence of which may be probed parametrically and through lower length scales. The method used to define ψ^+ and ψ^- varies in the various models.

As deformation is applied to the material, the stress divergence equation is used to determine the stress and strain, resulting in the deformation energy. The damage field d is evolved with time according to an Allen-Cahn equation,

$$\frac{\partial d}{\partial t} = -\frac{1}{\eta} \left(\frac{\delta F}{\delta d} \right) \tag{34}$$

where η is a kinetic parameter that defines the rate of evolution.

4.3.1 2D PF fracture simulation

The first work to apply the phase-field fracture method to UO_2 was Chakraborty et al. [Chakraborty2016]. They applied the method to investigate the impact of grain boundary porosity on the fracture strength of the material using 2D fracture simulations. To parameterize the phase-field method specifically for UO_2, the authors simulated fracture in UO_2 using molecular dynamics (MD) and then calibrated the value of g_c along the grain boundaries by comparing the stress-strain behavior from the phase-field fracture model to that from the MD simulation. The value of g_c within the grains was set to be five times that of the calibrated value on the grain boundaries, in order to ensure intergranular fracture. They implemented the

phase-field fracture model using the finite element method (FEM) with the Mulitphysics Object-Oriented Simulation Environment (MOOSE) [Gaston2009].

The calibrated model was then used to investigate the impact of interegranular porosity on the fracture strength, as illustrated in Figure 31. Square 2D polycrystalline structures with a 40 μm side length were created with an 8 μm average grain size (Figure 31a) and circular bubbles along the grain boundaries. Various grain structures and porosities were used and the polycrystals were deformed until fracture. The resultant stress-strain curves were recovered, as shown in Figure 31b. The fracture stress was shown to decrease with porosity with a power law relationship (Figure 31c). The fracture stresses predicted by the model were significantly larger than those obtained in experiments [Oguma 1982]. This was likely due to the use of MD simulations to calibrate the phase-field model; the MD simulations used idealized crystal structures are stronger than actual materials with are weakened by defects and impurities. The usage of circular bubbles instead of lenticular may also account for this discrepancy as discussed in Sec. 4.2.2. In addition, the change in the relative fracture strength with porosity was larger than what was seen in experiments.

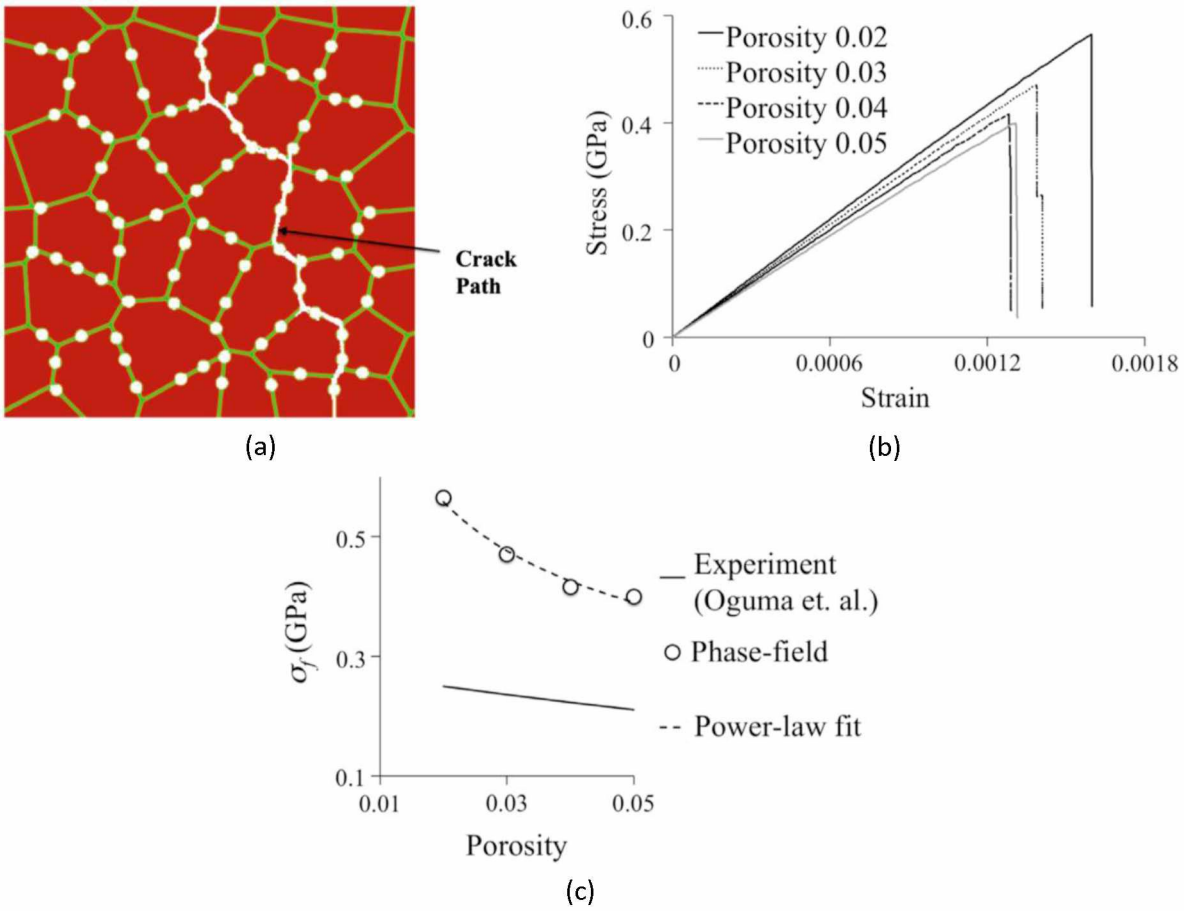

Figure 31: 2D phase field fracture results taken from [Chakraborty2016]. (a) shows the crack path predicted by the phase field fracture method in a 40 μm × 40 μm polycrystalline microstructure with a porosity of 4% and a bubble radius of 1 micron; (b) shows a comparison of the stress-strain evolution from simulations with different porosity; (c) shows the variation of the predicted fracture strength as a function of porosity compared with experimental data from [Oguma 1982].

4.3.2 3D PF fracture simulation

In reference (Jiang, 2020), the authors built on the work from (Chakraborty2016), but modeled the fracture of UO_2 polycrystals in 3D. They used the same phase field model implemented using FEM with MOOSE. They also used the same model parameters, including the g_c value calibrated by comparing with MD simulation results.

While Chakraborty et al. assumed that the grain boundary bubbles were spherical, Jiang et al. investigated the impact of the bubble shape on the fracture behavior. Actual grain boundary bubbles take on a lenticular shape, elongated parallel to the grain boundary. Jiang et al. compared the fracture behavior from three simulations of a 3D bicrystal with a single bubble. In one simulation the bubble was spherical, in one it was lenticular with a dihedral angle of 142.6°, and in one it was lenticular with a dihedral angle of 96.6°. They found that the bubble shape does significantly impact the crack behavior, with the spherical bubble resulting in the largest fracture strength and the lenticular bubble with a dihedral angle of 96.6° having the smallest, which is qualitatively in agreement with the results discussed in Sec. 4.2.2

They then ran 3D polycrystalline fracture simulations with increasing amounts of lenticular grain boundary bubbles, as shown in Figure 32, where the bubbles had a dihedral angle of 128° and a max cross-sectional radius of 3 μm. The 3D polycrystal domains were cubic, with a 40 μm side length and an average grain size of 9.4 μm. An example of the result from one simulation is shown in Figure 32a. The resultant stress-strain curves were recovered, as shown in Figure 32b, and the fracture strength was shown to decrease with porosity (Figure 31c)). The 3D simulations predicted a smaller decrease in the fracture strength with porosity than what was predicted by the 2D simulations from Chakraborty et al. The predicted decrease was also slower than what was found in the experiments by Oguta, but it was much closer than the 2D simulations. The 3D simulation results and the experimental data varied by about 5%. They also found that multiple loading directions resulted in an earlier crack nucleation and growth.

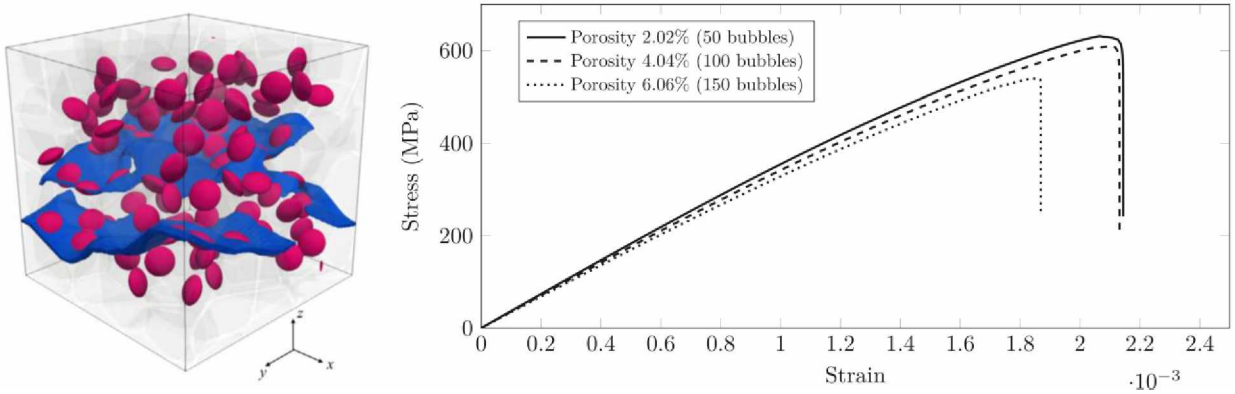

(a) (b)

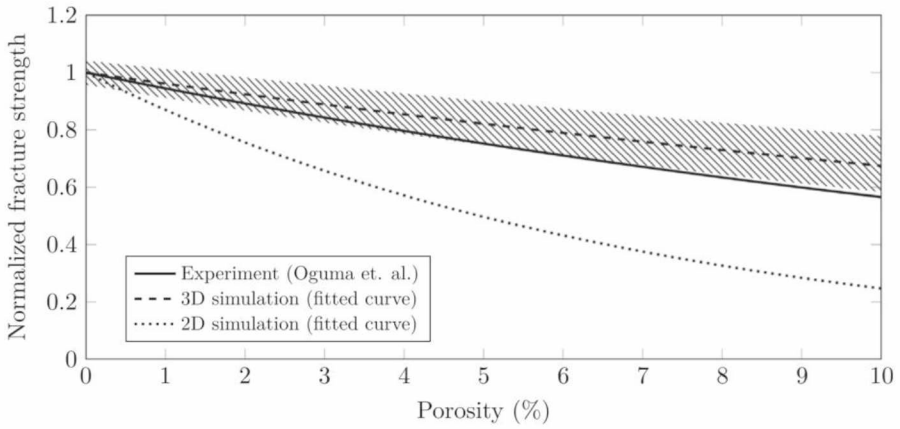

(c)

Figure 32: 3D phase field fracture results taken from Jiang et al. (Jiang2020). (a) shows the crack path predicted by the phase field fracture method in a $40\ \mu m \times 40\ \mu m \times 40\ \mu m$ polycrystalline microstructure with a porosity of 4.04%. The bubbles were lenticular, with a dihedral angle of 128° and a max cross-sectional radius of 3 μm. The bubbles are shown in red and the crack surface in blue. (b) shows a comparison of the stress-strain evolution from three simulations with different porosity. (c) shows the variation of the predicted fracture strength as a function of porosity compared with the 2D simulation results from Chakraborty et al. (Chakraborty2016) (Figure 31) and with experimental data from Oguma (Oguma 1982).

4.4 Fragmentation of a HBS Representative Volume Element: continuum local damage approach

The finite element approach has also been used to address the question of fission gas release and fuel fragmentation in the HBS zone of the pellet (Michel et al. 2016). Compare to the results of section 4.3 based on a phase-field model for the rupture process, this work uses a continuum local damage approach with a regularization technique to avoid mesh dependancy. The objective of this simulation is to assess the loading conditions leading to crack initiation around bubbles over pressurized by gaseous fission products, but also to explain the fragmentation mechanism at the microstructure scale.

The first step is to build and mesh a Representative Volume Element for a porous HBS. Bubble sizes statistical distribution is defined with post irradiation micrographic examinations, and bubble spatial localization statistical distribution is derived from a Random Sequential Addition algorithm (Widom 1966). An illustration of the methodology developed in reference (Esnoul 2018) is given in Figure 33. The finite element mesh is done through the Netgen 1D-2D-3D algorithm provided in the mesh module of the SALOME platform. In order to use periodic boundary conditions, and then improve the local assessment of strain and stress near the boundary, a specific algorithm has been developed for the geometrical model and the finite element mesh (Largenton et al. 2014).

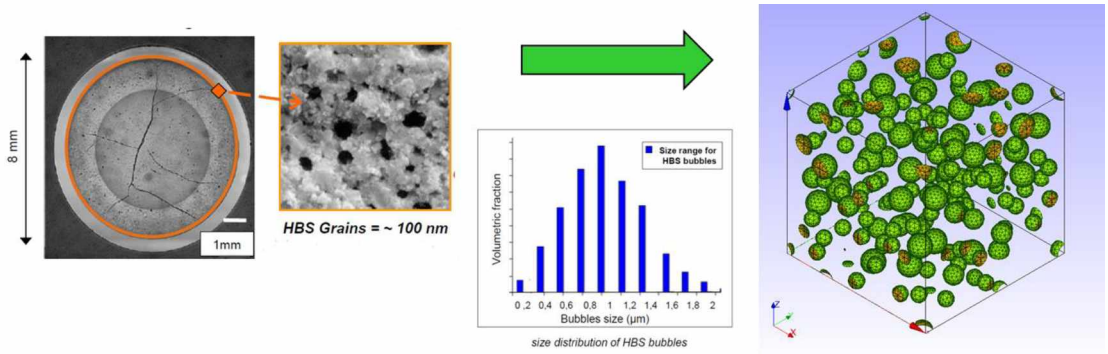

Figure 33 Numerical representative volume element of a porous HBS

Simulation of crack initiation and growth is achieved with a smeared crack model based on a continuum local damage approach (Michel et al. 2008). Regularization of the local model and computational scheme needed to simulate unstable crack growth in a brittle material are described in reference (Michel and al 2018). The material parameters of the smeared crack model are the rupture stress σ_R and the critical energy restitution rate G_C. The rupture stress, defined for spherical bubbles as the effective rupture stress given in equation (30), has been fitted through a reverse engineering method with experimental results coming from thermal annealing tests on fuel discs composed of a 100% HBS material (Noirot et al. 2014). The fit is based on the simulation results presented in the Figure 34. In the latter, the normalized loading is proportional to the experimental temperature in the annealing test and the first pressure drop at a normalized loading of 0.4 corresponds to the first gas released observed in the experiment. The pressure as a function of the annealing temperature in HBS bubbles is derived from the fission gas inventory at the end of irradiation as computed with the fission gas model MARGARET (Noirot 2011). In this case, the rupture stress has been fitted in order to have the first pressure drop at the temperature corresponding to the first gas release.

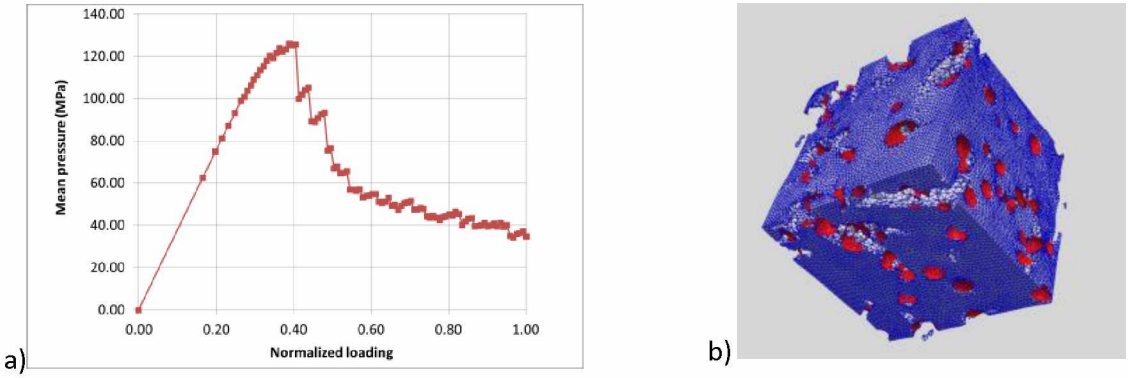

Figure 34: Full field simulation of a thermal annealing test for a HBS material showing a) Mean pressure of fission gases in HBS bubbles, and b) fuel fragmentation at normalized loading =0.4.

The rupture stress value, derived from the thermal annealing test, can be used to assess the critical energy restitution rate of the HBS material with equations (29) and (30). According the numerical application given in Table 9, G_C is equal to $0.12\ J/m^2$ which is much lower than the $20\ J/m^2$ measured with Vickers indentation method in reference (Matzke&Spino 1997). Given the differences observed in these comparisons, it is clear that the question of the toughness of the HBS material is still open.

$r_b\ (\mu m)$	$\sigma_R^{eff}\ (MPa)$	$f(\alpha)$	$G_C\ (\mathrm{J}/m^2)$

1	100	0.5	1.2E-01

Table 9 : Critical energy restitution rate derived from the fitted effective rupture stress

Among technical aspects of the full field simulation presented in this section, specific developments where needed regarding pressure loading in HBS bubbles and crack propagation. For the first point the pressure loading was replaced by a fictive free strain prescribed by the gas in the bubble. This has been done in order to ensure the convergence of the quasistatic mechanical equilibrium after crack initiation (Michel et al. 2018). Indeed, a Neumann boundary condition is not acceptable to have a static equilibrium with a softening material law. For the second aspect, crack propagation, the definition of the critical energy restitution rate used in the smeared crack model has been modified. Strictly, the value of G_C equal to $0.12\,J/m^2$ should have been used in order to be consistent with the rupture stress fitted on thermal annealing tests. However, the full field simulation is not able to represent rigorously the pressure loading induced by the gas transfer through the crack network after fragmentation initiation. Based on single bubble computation results presented in Figure 30b it is assumed that crack extension is unstable due to the fact that the elastic energy restitution rate increase when the crack size increase. Then in order to ensure an unstable crack extension in the full field simulation it is proposed to use an effective critical energy release rate, which represents the difference between the material critical energy release rate and the supplementary energy due to the pressure prescribed on the crack surface (see equation (35)). An assessment of $\Delta E_{Scrack}^{pressure}$ leads to conclude that $\mathrm{G_C^{eff}} \ll 1$.

$$\mathrm{G_C^{eff}} = G_C - \Delta E_{Scrack}^{pressure} \tag{35}$$

5 Open questions and suggested further research

Open questions focus on modelling or simulation and absolutely have to be associated to an experimental program in order to be able to achieve an essential separate effects validation at each scale. In this section, open questions resulting from the state of the art of fuel mechanical multi-scale modelling are summarized in order to give an overview of possible further research.

The impact of chemistry, including fission products and oxygen to metal ratio, point defects, fission gases and temperature on fuel elastic properties should be investigated with DFT simulations in order to provide reference values needed to justify or to derive more accurate interatomic potentials. The same data could also provide valuable input to multi-scale models of mechanical performance on its own. It is envioned that this information would be used to supplement targeted experiments. The simulations are able to investigate a braod range of defects and chemistries, some of which would be quite challenging to study by experimental techaniques alone. For instance, the high-temperature softening has only been investigated using semi-empirical potentials. UO_2 is also known to exhibit a complex temperature dependence of the elastic constants at low temperature, with softening and even diverging as the Néel temperature is approached. This is related to the complex electronic and magnetic structure of UO_2. This behavior is not yet fully understood and, certainly, there has been no attempt to capture it by DFT calculations.

Analysis of the crack initiation process at the atomic scale with an empirical potential gives valuable understanding of the atomic separation mechanisms. However, it is still difficult to derive some reference values for physical properties due to the scatter of the results in link with modelling assumptions. Further

progress could be expected from the definition of the loading conditions or from DFT simulation in order to make sure to derive intrinsic material properties.

The results obtained for the atomistic simulation of the fission gas bubble/matrix interface should be confirmed using variable charge potentials such that SMTB-Q as proposed to compute the physical parameters associated with thermally activated dislocation glide mobility (Sec. 2.3.1). In addition, kinetic aspects probably play a very important role in the behavior of nanometric bubbles, and should be elucidated.

In order to make the phase-field crystal methodology a truly mesoscale theory, there is an ongoing effort through coarse-graining methods, so-called amplitude expansions. Working in this direction would help to provide new tools for the multi-scale modelling addressing every phenomena of nonlinear mechanics coupled with multi-physics aspects.

For UO_2 creep behavior controlled by dislocation mobility, a complementary work is needed to have a multi-scale model with only physically based parameter. In particular, a single crystal model with continuous description between thermally activated plasticity and recovery creep should be obtained through a detailed understanding of cross-slip, combined slip, dislocation interactions and complex dislocation mobility involving climbing induced by void diffusion. To achieve the scale transfer up to the engineering law with polycrystalline microstructure, the separate effect validation should be completed. This validation is a key point to reach the objective of a predictive simulation, which can explain the scatter of experimental results. For this, one point currently under investigation concerns the Geometrically Necessary Dislocations to explain the sub-boundaries formation in initial UO_2 grains after a creep test.

To achieve the scale transfer of rupture properties more work is also needed, in particular to define an engineering rupture stress to address the effect of microstructural defects and their statistical distribution in the irradiated material. In link with this, small-scale rupture experiments in SEM should be completed to measure toughness on irradiated UO_2, in particular to characterize grain boundaries and HBS material.

Another general improvement will be to focus on the link between the different length scales, in order to ensure the coherence of the physical properties, and to couple with experimental investigations.

6 Conclusions

The state-of-the-art knowledge about the micromechanical modelling of the fuel pellet has been presented. It addresses all the loading conditions encountered in the reactor with elasticity, plasticity, creep and fracture behavior. This work follows a multiscale paradigm building up in spatio-temporal scale.

Atomistic-scale modelling review reveals mechanisms and physical parameters for elasticity of fresh and irradiated fuel, rupture, dislocation gliding and internal stresses induced by pressurized bubble with fission gases. Modelling techniques proposed at this scale are Density Functional Theory, Molecular Dynamic with empirical potential, Dislocation Dynamic and Phase Field Crystal methodology. Based on these approaches it can be concluded that some reference values can be proposed for the crystal elastic constants of stoichiometric UO_2 or $(U,Pu)O_2$ as a function of the temperature. MD results give also a new insight to understand and evaluate the impact of irradiation defects on the crystal configuration and its elastic properties. A detailed analysis of rupture at the atomic scale is now possible through MD simulations in order to understand the energy balance involved in the free surface creation process. The extraction of rupture properties, such as toughness or rupture stress, from these MD simulations is still a challenging question with an important on going activity. Regarding thermally activated plasticity, it is

now possible to simulate dislocation gliding in UO_2 for different temperature up to the a-thermal transition. The physical properties associated to gliding induced by a double kink mechanism, such as the Peierls Stress or the activation energy, can also be derived from simulations at 0K with atomic potentials. With DD the interaction matrix, needed to assess the material hardening associated to dislocation interaction, has been computed for UO_2. The upscaling of these properties for a creep model at engineering scale is still difficult and some supplementary empirical parameters are needed for the simulation of the strain-stress curve. One possible explanation is the lack of knowledge of elementary mechanisms where dislocation climbing is involved. Finally, the Phase Field Crystal methodology brings new methods to derive in a single continuum constitutive equation formalism for many mechanical mechanisms involved at very low scales.

State of the art of the micromechanical models for the viscoplastic shows that it is possible to describe the material behavior as a continuum from a single crystal to polycrystal systems and the interplay with irradiation and porosity. Crystal plasticity models, involving the dislocation motion and associated elementary mechanisms, are now available and validated for UO_2. These single crystal models, based on gliding systems and dislocation density, can give naturally the effect of the crystal orientation or of the grain size. They make possible and prepare the upscaling of the physical properties derived from atomic simulation. Some significant progress have also been done to derive, with homogenisation techniques, engineering elasto-plastic law for porous UO_2. Thanks to these tools, it is possible to have a physically based description of the coupling between mechanics and fission gases behavior, or to have a mechanical assessment of a material with a changing microstructure such as bubble coalescence under thermal gradient. To complete this, numerical experiments can be achieved with FE or FFT full field mechanical simulations for UO_2 polycristalline microstructure. These tools contribute to the upscaling process up to the engineering mechanical law needed in the fuel performance code.

The case of fuel rupture properties under irradiation was also discussed. A first conclusion is that post irradiation examinations and their interpretation at macroscopic scale give a quite complete empirical description of the fuel fragmentation process under different type of loading conditions. To complete this understanding, the multi-scale modelling of rupture is now possible and can bring some physically based assessment methods. The parameters of the smeared crack models used in fuel performance codes can be measured at the microstructure scale with SEM in situ bending tests. These low scale experiments coupled with micromechanical modelling are the keys for the multi-scale characterization of the fuel rupture properties including complex microstructures with porosities and grain boundaries. Associated to this, it is also possible for rupture to achieve the upscaling process with the interpretation of thermal annealing tests for a HBS material with a FE model of a Representative Volume Element of an irradiated microstructure.

In conclusion, it appears that the multiscale fuel micromechanical modelling starts to be possible with many significant progresses obtained thanks to computational effort and model developments. Further works have to go deeper in the scale transfer of the physical properties with an approach coupling experiments and simulations.

7 Acknowledgments

The authors would like to acknowledge the OECD Nuclear Energy Agency Working Party on Multi-Scale Modelling of Fuels and Structural Materials for Nuclear Systems (WPMM) for fostering this collaboration

8 Reference

Alamo A., Lefebvre J.M., Soulard J., *Déformation plastique du bioxyde d'uranium : observation des sous-structures de dislocations*, J. of Nucl. Mater., Vol.75(1), p.145-153, 1978.

Amodeo J., Devincre B., Carrez P., Cordier P., *Dislocation reactions, Plastic anisotropy and forest strengthening in MgO at high temperature*, Mech. Mater., Vol.71, p.62-73, 2014.

Andersson D.A., Lezama J., Uberuaga B.P., Deo C., and Conradson S.D., *Cooperativity among defect sites in AO2+x and A4O9 (A=U,Np,Pu): Density functional calculations*, Phys. Rev. B, Vol.79, 024110, 2009.

Anderson T.L., *Fracture mechanics Fundamental and Applications*, Fourth Edition. CRC Press, 2017.

Aoyagi, Y. et al., *Modeling and simulation on ultrafine-graining based on multiscale crystal plasticity considering dislocation patterning*, International Journal of Plasticity, vol. 47, pp. 13–28, Aug. 2013.

Arayro J., Tréglia G., and Ribeiro F., *Atomistic modelling of residual stress at UO_2 surfaces*, J. Phys.: Condens. Matter., Vol.28, 015006, 2015.

Arayro J., Tréglia G. and Ribeiro F., *Theoretical study of xenon adsorption on UO_2 surfaces*, J. of Physics Communications, Vol.2, 035041, 2018.

Arima T., Yamasaki S., Inagaki Y., Idemitsu K., *Evaluation of thermal properties of UO_2 and PuO_2 by equilibrium molecular dynamics simulations from 300 to 2000 K*, J. Alloys Compd., Vol.400, p.43-50, 2005.

Balboa H., Van Brutzel L., Chartier A., Le Bouar Y., *Assessment of empirical potential for MOX nuclear fuels and thermomechanical properties*, J. Nucl. Mater., Vol.495, p.67-77, 2017.

Balboa H.,Van Brutzel L., Chartier A., Le Bouar Y., *Damage characterization of $(U,Pu)O_2$ under irradiation by molecular dynamics simulations*, J. Nucl. Mater., Vol.512, p.440-449, 2018.

Barani, T., Bruschi, E., Pizzocri, D., Pastore, G., Van Uffelen, P., Williamson, R.L., Luzzi, L., *Analysis of transient fission gas behavior in oxide fuel using BISON and TRANSURANUS*, J. Nucl. Mater., Vol.486, p.96-110, 2017.

Barbe, F., Decker, L., Jeulin, D., and Cailletaud, G., *Intergranular and intragranular behavior of polycrystalline aggregates. Part 1&2*, International Journal of Plasticity, vol. 17, no. 4, pp. 513–536, Jan. 2001.

Baron D., Kinoshita M., Thevenin P. and Largenton R. Final report. International project HBRP 1994-2001, 2003.

Basak C.B., Sengupta A.K., and Kamath H.S., *Classical molecular dynamics simulation of UO_2 to predict thermophysical properties,* J. Alloys Compd., Vol.360, p.210-216, 2003.

Becquart C., Domain C.,Fivel M., Perez M. et Thuinet L., Chapter 7: Modeling Tools: From the Atom to the Macroscopic Scale, publié dans Mechanics - Microstructure - Corrosion Coupling Concepts, Experiments, Modeling and Cases, Editors : Christine Blanc et Isabelle Aubert, ISBN : 978-1-785-483-097, ISTE Press Elsevier, (2019).

Benedict U., Dabos S., Dufour C., and Spirlet J.C., *Neptunium compounds under high pressure*, J. Less Common Met., Vol.121, p.461-468, 1986.

Ben Saada, N. Gey, B. Beausir, X. Iltis, H. Mansour, and N. Maloufi, *Sub-boundaries induced by dislocational creep in uranium dioxide analyzed by advanced diffraction and channeling electron microscopy*, Materials Characterization, vol. 133, pp. 112–121, Nov. 2017, https://doi.org/10.1016/j.matchar.2017.09.023

Berry, J,. Provatas, N., Rottler, J., and Sinclair, C. W., *Phase Field Crystal Modeling as a Unified Atomistic Approach to Defect Dynamics*, Physical Review B - Condensed Matter and Materials Physics, Vol.89(21), p.1-13, 2014.
https://doi.org/10.1103/PhysRevB.89.214117

Berry, J., Elder, K. R., and Grant, M., *Simulation of an Atomistic Dynamic Field Theory for Monatomic Liquids: Freezing and Glass Formation*, Phys. Rev. E, Vol.77(6), p.1-7, 2008.
https://doi.org/10.1103/PhysRevE.77.061506

Berry J., Provatas N., Rottler J., and Sinclair C.W., *Defect Stability in Phase-Field Crystal Models: Stacking Faults and Partial Dislocations*, Phys. Rev. B, Vol.86(22), p.1-12, 2012.
https://doi.org/10.1103/PhysRevB.86.224112

Boittin G., Vincent P.G., Moulinec H., Garajeu M., *Numerical simulations and modeling of the effective plastic flow surface of a biporous material with pressurized intergranular voids*, Computer Methods in Applied Mechanics and Engineering, Vol.323, p.174-201, 2017.

Bourasseau E., Mouret A., Fantou P., Iltis X., Belin R., "Experimental and Simulation Study of GB in UO2", Journal of Nuclear Material, vol 517 p. 286-295, 2019.

Bourdin, B., Francfort, G.A., Marigo, J.-J., *Numerical experiments in revisited brittle fracture*, J. Mech. Phys. Solids., Vol.48, p.797-826, 2000.
https://doi.org/10.1016/S0022-5096(99)00028-9

Bourdin, B., Francfort, G.A., Marigo, J.-J., *The Variational Approach to Fracture*, J. Elast., Vol.91, p.5-148, 2008.
https://doi.org/10.1007/s10659-007-9107-3.

Brandt O.G. and Walker C.T., *Ultrasonic Attenuation and Elastic Constants for Uranium Dioxide*, Phys. Rev., Vol.170, p.528-541, 1968.

Brisard, S., Dormieux, L., Kondo, D., *Hashin–Shtrikman bounds on the bulk modulus of a nanocomposite with spherical inclusions and interface effects*. Comput. Mater. Sci., Vol.48(3), p.589–596, 2010.

Burn R., Murray G.T., *Plasticity and dislocation etch pits in CaF_2*, Journal of the American Ceramic Society, Vol.45, No.5, p.251-252, 1962.

Byron, *The yield and flox of single crystals of uranium dioxide*, J. Nucl. Mater., Vol.28(1), p.110-114, 1968.

Carlo A., Barone V. "Toward reliable density functional methods without adjustable parameters: The PBE0 model". The Journal of Chemical Physics. 110 (13): 6158–6170 (1999).

Carroll, R.M., Morgan, J.G., Perez, R.B., Sisman, O., *Fission density, burnup, and temperature effects on fission-gas release from UO_2*, Nucl. Sci. Eng., Vol.38, p.143-155, 1969.

Cast3M, Finite Element Software, URL: http://www-cast3m.cea.fr

Chakraborty, P, Zhang, Y., Tonks, M.R., *Multi-scale modeling of microstructure dependent intergranular brittle fracture using a quantitative phase-field based method*, Comput. Mater. Sci., Vol.113, p.38-52, 2016.
https://doi.org/10.1016/j.commatsci.2015.11.010

Chakraborty, P., Tonks, M.R., Pastore, G., *Modeling the influence of bubble pressure on grain boundary separation and fission gas release*, J. Nucl. Mater., Vol.452, p.95-101, 2014.

Chartier A., Meis C., Crocombette J-P., Weber W.J., and Corrales L.R., *Molecular dynamic simulation of disorder induced amorphization in pyrochlore*, Phys. Rev. Lett., Vol.94, 25505, 2005.

Chartier A., Van Brutzel L., Freyss M., Atomistic study of stability of xenon nanoclusters in uranium oxide, Phys. Rev. B 81 2010.

Chartier A., Onofri C., Van Brutzel L., Sabathier C., Dorosh O., and Jagielski J., *Early stages of irradiation induced dislocations in urania*, Appl. Phys. Lett., Vol.109, 181902, 2016.

Colbert, M. *Etude du comportement de gaz rares dans une matrice céramique à haute température : modélisation par approches semi-empiriques* (2012) Ph.D. thesis, Université d'Aix-Marseille.

Colbert M., Ribeiro F., and Tréglia G., *Atomistic study of porosity impact on phonon driven thermal conductivity: Application to uranium dioxide*, J. of Applied Physics, Vol.115, 034902, 2014-1.

Colbert M., Tréglia G., and Ribeiro F., *Theoretical study of xenon adsorption in UO_2 nanoporous matrices*, J. Phys.: Condens. Matter., Vol.26, 485015, 2014-2.

Cooper M.W.D., Rushton M.J.D., and Grimes R.W., *A many-body potential approach to modelling the thermomechanical properties of actinide oxides*, J. Phys.: Condens. Matter., Vol.26, 105401, 2014.

Crocombette J-P., Jollet F., Thien Nga L., and Petit T., *Plane-wave pseudopotential study of point defects in uranium dioxide*, Phys. Rev. B, Vol.64, 104107, 2001.

Crocombette J-P., Chartier A., and Weber W.J., *Atomistic simulation of amorphization thermokinetics in lanthanum pyrozirconate*, Appl. Phys. Lett., Vol.88, 51912, 2006.

Cronenberg, A.W., Yackle, T.R., *Intergranular fracture of unrestructed UO_2 fuel, during film-boiling operation*, J. Nucl. Mater., Vol.84, p.295-318, 1979.
https://doi.org/10.1016/0022-3115(79)90170-3.

Delaire, F. et al., *Plastic heterogeneities of a copper multicrystal deformed in uniaxial tension: experimental study and finite element simulations*, Acta Materialia, vol. 48, no. 5, pp. 1075–1087, Mar. 2000.

Desai T.G., Millett P.C., Wolf D., *Molecular dynamics study of diffusional creep in nanocrystalline UO_2*, Acta Materialia, Vol.56, p.4489-4497, 2008.

Desai T.G., Uberuaga B.P., *Stress-induced phase transformation in nanocrystalline UO_2*, Scripta Materialia, Vol.60, p.878-881, 2009.

Devey A.J., J. Nucl. Mater., *First principles calculation of the elastic constants and phonon modes of UO_2 using GGA + U with orbital occupancy control*, Vol.412, p.301-307, 2011.

Devincre B., Hoc T., Kubin L., *Colinear superjogs and the low-stress response of fcc crystals*, Scripta Materialia, Vol.57, p.905-908, 2007.

Dorado B., Amadon B., Freyss M., and Bertolus M., *DFT+U calculations of the ground state and metastable states of uranium dioxide*, Phys. Rev. B, Vol.79, 235125, 2009.

Dorado B. and Garcia Ph., *First-principles DFT+U modeling of actinide-based alloys: Application to paramagnetic phases of UO_2 and (U,Pu) mixed oxides*, Phys. Rev. B, Vol.87, 195139, 2013.

Dormieux, L. and Kondo, D., An extension of Gurson model incorporating interface stresses effects, International Journal of Engineering Science, 48(6):575–581, 2010

Duan, H. , Wang, J. , Huang, Z. , Karihaloo, B., *Eshelby formalism for nano- inhomogeneities*, Proc. R. Soc. A: Math., Phys. Eng. Sci., Vol.461, p.3335-3353, 2005.

Dudarev S.L., Botton G.A., Savrasov S.Y., Szotek Z., Temmerman W.M., and Sutton A.P., *Electronic Structure and Elastic Properties of Strongly Correlated Metal Oxides from First Principles: LSDA + U, SIC-LSDA and EELS Study of UO_2 and NiO*, Phys. Status Solidi A, Vol.166, p.429-443, 1998.

Edington J.W., M.J. Klein, *Slip and fracture in single crystals of thoria*, Journal of Applied Physics, Vol.37(10), p.3906-3908, 1966.

Elder, K. R., and Grant M., *Modeling Elastic and Plastic Deformations in Nonequilibrium Processing Using Phase Field Crystals*, Physical Review E, Vol.70(5), 18, 2004.
https://doi.org/10.1103/PhysRevE.70.051605

Elder, K. R., Katakowski M., Haataja M., and Grant M. *Modeling Elasticity in Crystal Growth*. Phys. Rev. Lett., Vol.88(24), 2457011-14, 2002.
https://doi.org/10.1103/PhysRevLett.88.245701

Elder, K. R., Provatas N., Berry J., Stefanovic P., and Grant M. *Phase-Field Crystal Modeling and Classical Density Functional Theory of Freezing*, Phys. Rev. B, Vol.75(6), 064107, 2007.
https://doi.org/10.1103/PhysRevB.75.064107

Eli A., Montiel D., Thornton K., and Voorhees P.W., *Simulating Complex Crystal Structures Using the Phase-Field Crystal Model*. Physical Review Materials, Vol.1(6), 2017.
https://doi.org/10.1103/PhysRevMaterials.1.060801

Esnoul C., *Comportement à rupture du combustible des Réacteurs à Eau Pressurisée, par une approche micro-mécanique, en conditions accidentelles*. Ph-D rapport, 2018.

Evans A.G., Roy C., and Pratt P.L., *The role of grain boundaries in the plastic deformation of calcium fluoride*, Proceedings of British Ceramic Society, Vol.6 , p.173-189, 1966.

Evans A.G., Davidge R.W., *The strength and fracture of stoichiometric polycrystalline UO_2*, J. Nucl. Mater., Vol.33, p.249-260, 1969.
https://doi.org/10.1016/0022-3115(69)90019-1.

Fossati P., Van Brutzel L., Chartier A., Crocombette J-P., *Simulation of uranium dioxide polymorphs and their phase transitions*, Phys. Rev. B, Vol.88, 214112, 2013.

Francfort, G.A., Marigo, J.-J., *Revisiting brittle fracture as an energy minimization problem*, J. Mech. Phys. Solids., Vol.46, p.1319-1342, 1998.
https://doi.org/10.1016/S0022-5096(98)00034-9.

Franciosi P., Berveiller M., Zaoui A., *Latent hardening in copper and aluminium single crystals*, Acta Metallurgica, Vol.28, p.273-283, 1980.

Frazer B.C., Shirane G., and Cox D.E., *First-Order Magnetic Transition in UO_2*, J. App. Phys., Vol.37, p.1386, 1966.

Freyss M., Petit T., and Crocombette J-P., *Point defects in uranium dioxide: Ab initio pseudopotential approach in the generalized gradient approximation*, J. Nucl. Mater., Vol.347, p.44-51, 2005.

Fritz I.J., *Elastic properties of UO_2 at high pressure*, J. Appl. Phys., Vol.47, p.4353-4358, 1976.

Frost H.J. and Ashby M.F., *Deformation-mechanism maps : the plasticity and creep of metals and ceramics*. Pergamon Press, 1982.

Gaston D., Newman C., Hansen G., Lebrun-Grandié D., *MOOSE: A parallel computational framework for coupled systems of nonlinear equations*, Nucl. Eng. Des., Vol.239, p.1768-1778, 2009.
https://doi.org/10.1016/j.nucengdes.2009.05.021

Gatt, J.-M., Sercombe, J., Aubrun, I., Ménard, J.-C., *Experimental and numerical study of fracture mechanisms in UO2 nuclear fuel*, Eng. Fail. Anal., Vol.47, p.299-311, 2015.
https://doi.org/10.1016/j.engfailanal.2014.07.019.

Geng H.Y., Chen Y., Kaneta Y., and Kinoshita M., *Structural behavior of uranium dioxide under pressure by LSDA+U calculations*, Phys. Rev. B, Vol.75, 054111, 2007.

Gilbert A., *Deformation and fracture of thoria*, Pilosophical Magazine, Vol.12(15), p.139-144, 1965.

Gologanu M., Leblond, J., Devaux, J., 1994. *Approximate models for ductile metals containing non-spherical voids-case of axisymmetric oblate ellipsoidal cavities*. ASME J. Eng. Mater. Technol., Vol.116, p.290–297.

Govers, K., Lemehov, S., Hou, M., Verwerft, M., *Comparison of interatomic potentials for UO_2. Part I: Static calculations*, J. Nucl. Mater., Vol.366, p.161–177, 2007.

Greenwood, M., Provatas, N., and Rottler, J., *Free Energy Functionals for Efficient Phase Field Crystal Modeling of Structural Phase Transformations.* Phys. Rev. Lett., Vol.105(4), p1-4, 2010. https://doi.org/10.1103/PhysRevLett.105.045702.

Gryaznov D., Heifets E., and Kotomin E., *Ab initio DFT+U study of He atom incorporation into UO_2 crystals*, Phys. Chem. Chem. Phys., Vol.11, p.7241-7247, 2009.

Gupta F., Brillant G., and Pasturel A., *Correlation effects and energetics of point defects in uranium dioxide: a first principle investigation*, Philos. Mag., Vol.87, p.2561-2569, 2007.

Gurson A., *Continuum theory of ductile rupture by void nucleation and growth: Part I - Yield criteria and flow rules for porous ductile media*, J. Eng. Mat. Tech., Vol.99, p.1-15, 1977.

Gurtin, M. , Murdoch, A., *A continuum theory of elastic material surfaces*. Arch. Ration. Mech. Anal., Vol.57 (4), p.291-323, 1975.

Haller, X. *Modélisation du comportement élastique des matériaux nanoporeux : application au combustible UO_2* (2015) Ph.D. thesis, Université de Montpellier.

Haller, X., Monerie, Y., Pagano, S., Vincent, P.-G. *Elastic behavior of porous media with spherical nanovoids*, International Journal of Solids and Structures, Vol.84, p.99-109, 2016.

Hastings, I.J., Smith, A.D., Fehrenbach, P.J., Carter, T.J., *Fission gas release from power-ramped UO_2 fuel*, J. Nucl. Mater., Vol.139, p.531-543, 1969.

Helfer T., *Introducing the open-source mfront code generator: Application to mechanical behaviors and material knowledge management within the PLEIADES fuel element modelling platform*, Computers and Mathematics with Applications, Vol.70(5), p.994-1023, 2015.

Henry R., T. Blay, T. Douillard, A. Deschamps-Mandine, I. Zacharie-Aubrun, J-M Gatt, C. Langlois, S. Meille, *Local fracture toughness measurements in polycrystalline cubic zirconia using micro-cantilever bending tests*, Mech. of Mat., Vol.136, 103086, 2019.

Hering, W., *The KWU fission gas release model for LWR fuel rods*, J. Nucl. Mater., Vol.114, p.41-49, 1982.

Heyd J., Scuseria G.; Ernzerhof M. "Hybrid functionals based on a screened Coulomb potential". J. Chem. Phys. 118 (18): 8207 (2003).

Hu, S., Chen Z., Peng Y. Y., Liu Y. J., and Guo L. Y.,.*Modeling and Simulation of Microcrack Propagation Behavior under Shear Stress Using Phase-Field-Crystal*. Computational Materials Science, Vol.121, p.143-50, 2016.
https://doi.org/10.1016/j.commatsci.2016.04.035

Huang, H., Spencer, B., Hales, J., *Discrete element method for simulation of early-life thermal fracturing behavior in ceramic nuclear fuel pellets*, Nucl. Eng. Des., Vol.278, p.515-528, 2014.

https://doi.org/10.1016/j.nucengdes.2014.05.049

Hutchings M.T., *High-temperature studies of UO_2 and ThO_2 using neutron scattering techniques*, J. Chem. Soc., Faraday Trans., Vol.83, p.1083-1103, 1987.

Idiri M., Le Bihan T., Heathman S., and Rebizant J., *Behavior of actinide dioxides under pressure*, Phys. Rev. B, Vol.70, 014113, 2004.

Igata, N., Domoto, K., *Fracture stress and elastic modulus of uranium dioxide including excess oxygen*, J. Nucl. Mater., Vol.45, p.317-322, 1973.
https://doi.org/10.1016/0022-3115(73)90165-7

Jelea, A., Colbert M., Ribeiro F., Tréglia G., Pellenq R.-M., *An atomistic modelling of the porosity impact on UO_2 matrix macroscopic properties*. J. Nucl. Mater., Vol.415 (2), p.210–216, 2011.

Jelea A., Pellenq R.-M., Ribeiro F., *An atomistic modeling of the xenon bubble behavior in the UO_2 matrix*, J. Nucl. Mater., Vol.444, p.153–60, 2014.

Jernkvist L. O., *A continuum model for cracked UO_2 fuel*, Nuclear Engineering and Design, Vol.176(3), p.273-284, 1997.

Jernkvist L.O., *A review of analytical criteria for fission gas induced fragmentation of oxide fuel in accident conditions*, Prog. Nucl. Energy., Vol.119, 103188, 2020.
https://doi.org/10.1016/j.pnucene.2019.103188

Jiang W., Hu T., Aagesen L.K., Zhang Y., *Three-dimensional phase-field modeling of porosity dependent intergranular fracture in UO_2*, Comput. Mater. Sci., Vol.171, 109269, 2020.
https://doi.org/10.1016/j.commatsci.2019.109269

Jiang W., Spencer B.W., Dolbow J.E., *Ceramic nuclear fuel fracture modeling with the extended finite element method*, Eng. Fract. Mech., Vol.223, 106713, 2020.
https://doi.org/10.1016/j.engfracmech.2019.106713.Jollet F., Jomard G., Amadon B., Crocombette J-P., and Torumba D., *Hybrid functional for correlated electrons in the projector augmented-wave formalism: Study of multiple minima for actinide oxides*, Phys. Rev. B, Vol.80, 235109, 2009.

Julien J., Gărăjeu M., Michel J.-C., A semi-analytical model for the behavior of saturated viscoplastic materials containing two populations of voids of different sizes, International Journal of Solids and Structures, Volume 48, Issue 10, 2011, Pages 1485-1498, https://doi.org/10.1016/j.ijsolstr.2011.01.031

Keig G.A. and R.L. Coble, *Mobility of edge dislocations in single crystal calcium Fluoride*, Journal of Applied Physics, Vol.39(13), p.6090, 1968.

Keller R.J., Mitchell T.E., Heuer A.H., *Plastic deformation in nonstoichiometric UO_{2+x} single crystals – I and II. Deformation at low temperatures*, Acta metallica, Vol.36(4), p.1061-1083, 1988.

Kocher G., and Provatas N., *New Density Functional Approach for Solid-Liquid-Vapor Transitions in Pure Materials*, Phys. Rev. Lett., Vol.114(15) p.1-5, 2015.
https://doi.org/10.1103/PhysRevLett.114.155501

Kogai T., *Modelling of fission gas release and gaseous swelling of light water reactor fuels*, J. Nucl. Mater. Vol.244, p.131-140, 1997.

Koizumi H., Kirchner H.O.K., and Suzuki T., *Kink pair nucleation and critical shear stress,* Acta Metallurgica et Materialia., Vol.41, p.3483-3493, 1993.

Kong, L. Y., Gao, Y.J., Deng, Q.Q., Luo, Z. R., and Lu, Y.J., A Study of Strain-Driven Nucleation and Extension of Deformed Grain: Phase Field Crystal and Continuum Modeling. Materials, Vol.11(10), 1805, 2018.

https://doi.org/10.3390/ma11101805

Koo Y.H., Lee B.H., Sohn D.S., *COSMOS: a computer code to analyze LWR UO_2 and MOX fuel to high burnup*, Ann. Nucl. Energy, Vol.26, p.47-67, 1999.

Kulacsy, K., *Mechanistic model for the fragmentation of the high-burnup structure during LOCA*, J. Nucl. Mater. 466, pp. 409-416, 2015.

Largenton R., Michel J.-C., and Suquet P., *Extension of the Nonuniform Transformation Field Analysis to linear viscoelastic composites in the presence of aging and swelling*, Mechanics of Materials, Vol.73, p.76-100, 2014.

Lefebvre J.M., *Contribution à l'étude de la déformation plastique d'une céramique de strucuture fluorite : le bioxyde d'uranium*, PhD thesis, faculté des sciences de Poitiers, 1976.

Liu T.S., C.H. Li, *Plasticity and of barium fluoride single crystals*, Journal of Applied Physics, Vol.35(11), p. 3325-3330, 1964.

Liu X.-Y., Andersson D.A., Molecular dynamics study of fission gas bubble nucleation in UO2, J. of Nucl. Mater. 462 8-14 2015.

Madec R., Devincre B., Kubin L., *On the nature of attractive dislocation crossed states*, R. Computational Materials Science, Vol.23(1), p.219-224, 2002.

Madec R., Devincre B., Kubin L., Hoc T., Rodney D., *The role of colinear interaction in dislocation-induced hardening*, Science, Vol.301(5641), p.1879-1882, 2003.

Madec R. and Kubin L., *Dislocation strengthening in FCC metals and in BCC metals at high temperatures*, Acta Materialia, Vol.126, p.166‑173, 2017.

Matzke H. and J. Spino, *Formation of the rim structure in high burnup fuel*, J. Nucl. Mater., Vol.248, p.170-179, 1997.

Michel B. and al., *A new numerical methodology for simulation of unstable crack growth in time independent brittle materials*, Engineering Fracture Mechanics, Vol.188, p.126-150, 2018.

Michel B., J. Sercombe, G. Thouvenin, *A new phenomenological criterion for pellet–cladding interaction rupture*, Nuclear Engineering and Design, Vol.238(7), p.1612-1628, 2008.

Michel B., Sercombe J., Thouvenin G., and Chatelet R., *3D fuel cracking modelling in pellet cladding mechanical interaction*, Engineering Fracture Mechanics, Vol.5(11), p.3581-3598, 2008.

Michel B., Nonon C., Sercombe J., Michel F., Marelle V., *Simulation of the Pellet Cladding Interaction phenomenon with the PLEIADES fuel performance software environment*, Nuclear Technology, Vol.182(2), p.124-137, 2013.

Michel B., T. Helfer, I. Ramiere, and C. Esnoul, *3D continuum damage approach for simulation of crack initiation and growth in ceramic materials*, Key Engineering Materials, Vol.713, p.155-158, 2016.

Millett P.C., Wolf D., Desai T., and Yamakov V., *Time scale for point-defect equilibration in nanostructures*, Applied Phys. Lett., Vol.93, 161902, 2008.

Monchiet V. and Bonnet G., Interfacial models in viscoplastic composites materials, International Journal of Engineering Science, 48(12):1762–1768, 2010.

Moran B. and Shih C.F., *A general treatment of crack tip contour integrals*, Int J Fract, Vol.35(4), p.295-310, 1987.

Morelon N., Delaye J.M., Ghaleb D., Van Brutzel L., *A new empirical potential for simulating the formation of defects and their mobility in uranium dioxide*. Philosophical Magazine, Vol.83, p.1533-1550, 2003.

Moulinec H. and Suquet P., C.R., Acad. Sci. Paris II, Vol.318, p.1417, 1994.

Murphy S.T., Chartier A., Van Brutzel L., Crocombette J.P., "*Free energy of Xe incorporation at point defects and in nanovoids and bubbles in UO_2*" Phys. Rev. B 85, 2012.

Nadeau J.S., *Dependence of flow stress on nonstoichiometriy in oxygen-rich uranium dioxide at high temperature*, Journal of the American ceramic society, Vol.52(1), p.1-7, 1969.

Nakamura, J., Suzuki, M., Uetsuka, H. (1999), *Re-irradiation tests of LWR spent fuel at JMTR*, in: Enlarged Halden Programme Group Meeting, Loen, Norway, May 24-29.

Newmann J.C. (1971), *An Improved Method of Collocation for the Stress Analysis of Cracked Plates with Various Shaped Boundaries*, Technical Report, NASA, Washington, DC, USA.

Noirot J., Noirot L., Desgranges L. et al., *Fission gas inventory in PWR high burnup fuel. Experimental characterisation and modelling*. Proceedings of the 2004 International Meeting on LWR Fuel Performance. Orlando, FL, 2004.

Noirot J., Pontillon Y., Yagnik S., Turnbull J.A., and Tverberg T., *Fission gas release behavior of a 103GWd/tHM fuel disc during a 1200°C annealing test*, J. Nucl. Mater., Vol.446(1), p.163-171, 2014.

Noirot L., *MARGARET: A comprehensive code for the description of fission gas behavior*, Nuclear Engineering and Design, Vol.241(6), p.2099-2118, 2011.

Notley, M.J.F., MacEwan, J.R., *Stepwise release of fission gas from UO_2 fuel*, Nucl. Appl., Vol.2, p.477, 1966.

Ofori-Opoku N., Fallah V., Greenwood M., Esmaeili S., and Provatas N., *Multicomponent Phase-Field Crystal Model for Structural Transformations in Metal Alloys*. Phys. Rev. B, Vol.87(13), 134105, 2013. https://doi.org/10.1103/PhysRevB.87.134105

Ofori-Opoku N., Stolle J., Huang Z.F., and Provatas N. *Complex Order Parameter Phase-Field Models Derived from Structural Phase-Field-Crystal Models*. Phys. Rev. B, Vol.88, 104106, 2013. https://doi.org/10.1103/PhysRevB.88.104106

Oguma M., *Microstructure Effects on Fracture Strength of $U0_2$ Fuel Pellets*, J. Nucl. Sci. Technol., Vol.19, p.1005-1014, 1982. https://doi.org/10.1080/18811248.1982.9734249

Oterkus S., Madenci W., *Peridynamic modeling of fuel pellet cracking*, Eng. Fract. Mech., Vol.176, p.23-37, 2017. https://doi.org/10.1016/j.engfracmech.2017.02.014

Pastore G., Luzzi L., Di Marcello V., Van Uffelen P., *Physics-based modelling of fission gas swelling and release in UO2 applied to integral fuel rod analysis*, Nucl. Eng. Des., Vol.256, p.75-86, 2013.

Petit L., Svane A., Szotek Z., Temmerman W.M., and Stocks G.M., *Electronic structure and ionicity of actinide oxides from first principles*, Phys. Rev. B, Vol.81, 045108, 2010.

Phillips W.L., *Deformation and fracture processes in calcium fluoride single crystals*, Journal of the American Ceramic Society, Vol.44(10), p.499-506, 1961.

Ponte Castañeda, P., *The effective mechanical properties of nonlinear isotropic composites*. J. Mech. Phys. Solids, Vol.39, p.45-71, 1991.

Portelette L. et al., *Crystal viscoplastic modeling of UO_2 single crystal*, J. Nucl. Mater., Vol.510, p.635-643, 2018.

Portelette L., et al. *Numerical simulation of the UO2 viscoplasticity at the polycrystal scale: microscopic validation*, In 16th European Mechanics of Materials Conference, Nantes, March 26th-28th, 2018, 2018.

Portelette L., Amodeo J., Michel B., Madec R., *Athermal dislocation strengthening in uranium dioxide*, J. Nucl. Mater., Vol.538, p.152-157, 2020.

Portelette L., Vincent P.-G., Moulinec H., Gărăjeu M., *Viscoplastic behavior of a porous polycrystal with similar pore and grain sizes: Application to nuclear MOX fuel materials*, International Journal of Solids and Structures, Vol.236–237, 111316, 2022. https://doi.org/10.1016/j.ijsolstr.2021.111316

Potashnikov S.I., Boyarchenkov A.S., Nekrasov K.A., Kupryazhkin A.Ya., *Highprecision molecular dynamics simulation of UO_2-PuO_2: pair potentials comparison in UO_2*, J. Nucl. Mater., Vol.419, p.217-225, 2011.

Prodan I.D., Scuseria G.E., and Martin R.L., *Assessment of metageneralized gradient approximation and screened Coulomb hybrid density functionals on bulk actinide oxides*, Phys. Rev. B, Vol.73, 045104, 2006.

Provatas N., Dantzig J.A., Athreya B., Chan P., Stefanovic P., Goldenfeld N., and Elder K. R. *Using the Phase-Field Crystal Method in the Multi-Scale Modeling of Microstructure Evolution*. JOM-The Journal of The Minerals, Vol.59(7) p.83-90, 2007.
https://doi.org/10.1007/s11837-007-0095-3.

Prudil, A.A. Colins, K.D. Thomas, E.S. Welland, M.J., *Intra- and intergranular fission gas transport on large irregular hexagonal grain networks by an included phase model*, J. Nucl. Mater., Vol.542, 152456, 2020.

Raabe, D. et al., *Micromechanical and macromechanical effects in grain scale polycrystal plasticity experimentation and simulation*, Acta Materialia, vol. 49, no. 17, pp. 3433–3441, Oct. 2001.

Radford, K.C., *Effect of fabrication parameters and microstructure on the mechanical strength of UO_2 fuel pellets*, J. Nucl. Mater., Vol.84, p.222-236, 1979.
https://doi.org/10.1016/0022-3115(79)90165-X

Rapperport E.J. and Huntress A.M., *Deformation modes of single crystals uranium dioxide from 700°C to 1900°C*, Nuclear Metals, Inc. Concord, Massachisetts, 1960.

Rest, J., *An improved model for fission product behavior in nuclear fuel under normal and accident conditions*, J. Nucl. Mater., Vol.120, p.195-212, 1984.

Rice J.R., *A Path Independent Integral and the Approximate Analysis of Strain Concentration by Notches and Cracks*, J. Appl. Mech., Vol.35, p.379-386, 1968.

Roberts J.T.A., Ueda Y., *Influence of Porosity on Deformation and Fracture of UO_2*, J. Am. Ceram. Soc., Vol.55, p.117-124, 972.
https://doi.org/10.1111/j.1151-2916.1972.tb11233.x

Rothwell, E., *The release of Kr85 from irradiated uranium dioxide on post-irradiation annealing*, J. Nucl. Mater., Vol.5, p.241-249, 1962.

Sachtleber, M., et al., *Experimental investigation of plastic grain interaction*, Materials Science and Engineering: A, vol. 336, no. 1, pp. 81–87, Oct. 2002.

Salvalaglio M, Voigt A., and Elder K.R., *Closing the Gap between Atomic-Scale Lattice Deformations and Continuum Elasticity*. Npj Computational Materials, Vol.5, p1-8, 2019.
https://doi.org/10.1038/s41524-019-0185-0

Salvalaglio M., Backofen R., Voigt A., and Elder K.R., *Controlling the Energy of Defects and Interfaces in the Amplitude Expansion of the Phase-Field Crystal Model*. Phys. Rev. E, Vol.96(2), 023301,2017. https://doi.org/10.1103/PhysRevE.96.023301.

Sanati M., Albers R.C., Lookman T., and Saxena A., *Elastic constants, phonon density of states, and thermal properties of UO_2*, Phys. Rev. B, Vol.84, 014116, 2011.

Sattonnay G. and Tetot R., *Bulk surface and point defect properties in UO_2 from a tight-binding variable-charge model,* Journal of Physics-Condensed Matter., Vol.25, p.10, 2010.

Sawbridge P.T. and E.C. Sykes, *Dislocation glide in UO_2 single crystals at 1600 K*, Philosophical Magazine, Vol.24, p.33-53, 1971.

Schwalbach E. J., Warren J. A., Wu K.A., and Voorhees P.W., *Phase-Field Crystal Model with a Vapor Phase*. Phys. Rev. E, Vol.88(2), p.1-14, 2013.
https://doi.org/10.1103/PhysRevE.88.023306

Schwartz, J. et al., *Numerical approach of cyclic behavior of 316LN stainless steel based on a polycrystal modelling including strain gradients*, International Journal of Fatigue, vol. 55, pp. 202–212, Oct. 2013.

Seltzer M.S, Clauer C.L., Wilcox B.A., *The influence of stoichiometry on compression creep of uranium dioxide single crystals*, J. Nucl. Mater., Vol.44(1), p.43-56, 1972.

Smith N., and Provatas N., *Generalization of the Binary Structural Phase Field Crystal Model*. Physical Review Materials, Vol.1(5), 053407, 2017.
https://doi.org/10.1103/PhysRevMaterials.1.053407

Solomon A.A., *Influence of Impurity Particles on the Fracture of UO_2*, J. Am. Ceram. Soc., Vol.55, p.622-627, 1972.
https://doi.org/10.1111/j.1151-2916.1972.tb13456.x

Stan M., Multi-scale models and simulations of nuclear fuels, Nuclear engineering and technology 41.1 (2009): 39-52

Stolz, C. , Zaoui, A., *Analyse morphologique et approches variationnelles du comportement d'un milieu élastique hétérogène*. Comptes Rendus de l'Académie des Sci., Vol.312, p.143-150, 1991.

Tada H., Paris P.C., Irwin G.R., *The Stress Analysis of Cracks Handbook*, third ed., ASME, NY, USA, 2000.

Thomason P., *Three-dimensional models for the plastic limit-loads at incipient failure of the intervoid matrix in ductile porous solids*. Acta Metall., Vol.33(6), p.1079-1085, 1985.

Thompson A.E. and C. Wolverton C., *First-principles study of noble gas impurities and defects in UO_2*, Phys. Rev. B, Vol.84, 134111, 2011.

Thompson A.E., Meredig B., Stan M., and Wolverton C., *Interatomic potential for accurate phonons and defects in UO_2*, J. Nucl. Mater., Vol.446, p.155-162, 2014.

Tian X., Gao T., Jiang G., He D., and Xiao H., *The incorporation and solution of krypton in uranium dioxide: Density functional theory calculations*, Comput. Mater. Sci., Vol.54, p.188-194, 2012.

Tian X., Ge L., Yu Y., Wang Y., You Z., Li L., *Atomistic simulation of fracture in UO_2 under tensile loading*, J. Alloys and Compounds, Vol.803, p.42-50, 2019.

Tonks M., et al., *Unit mechanisms of fission gas release: Current understanding and future needs*, J. Nucl. Mat. 504, pp 300-317, 2018.

Tonks M. et al., Mechanistic materials modeling for nuclear fuel performance, Annals of nuclear energy 105 (2017): 11-24.

Tvergaard, V., *Influence of voids on shear band instabilities under plane strain conditions*. International Journal of Fracture, Vol.17(4), p.389-407, 1981.

Tvergaard V. and Needleman A., *Analysis of the cup-cone fracture in a round tensile bar*. Acta Metallurgica, Vol.32(1), p157-169, 1984.

Une, K., Kashibe, S., *Fission gas release during post irradiation annealing of BWR fuels*, J. Nucl. Sci. Technol., Vol.27, p.1002-1016, 1990.

Van Uffelen P., Schubert A., van de Laar J., Győri C., *Development of a transient fission gas release model for TRANSURANUS*, in: Water Reactor Fuel Performance Meeting, Seoul, Korea, October 19-23, 2008.

Vazhappilly T. and Pathaka A.K., *A first principle based study on the mechanical and thermal properties of UO_2: Effect of La and Dy fission product concentrations*, Comp. Mater. Sci., Vol.185, 109933, 2020.

Veschunov M. S. et al., Development of the advanced mechanistic fuel performance and safety code using the multi-scale approach, Nuclear Engineering and Design 295 (2015): 116-126.

Vincent P.G., P. Suquet, Y. Monerie, H. Moulinec, *Effective flow surface of porous materials with two populations of voids under internal pressure: I. A GTN model*, Int. J. Plast., Vol.56, p.45-73, 2014-a.

Vincent P.-G., Suquet P., Monerie Y., Moulinec H., *Effective flow surface of porous materials with two populations of voids under internal pressure: II. Full-field simulations*, Int. J. Plast., Vol.56, p.74–98, 2014-b.

Vincent, P.-G., Monerie, Y., Suquet, P., *Porous materials with two populations of voids under internal pressure. I: Instantaneous constitutive relations*. Int. J. Solids Struct., Vol.46, p.480-506; 2009-a.

Vincent, P.-G., Monerie, Y., Suquet, P., *Porous materials with two populations of voids under internal pressure. II: Growth and coalescence of voids*. Int. J. Solids Struct., Vol.46, p.507-526, 2009-b.

Walker C.T., Knappik P., Mogensen M., *Fission gas release from power-ramped UO_2 fuel*, J. Nucl. Mater., Vol.161, p.10-23, 1988.

Wang B.-T., Zhang P., Lizarraga R., Di Marco I., and Eriksson O., *Phonon spectrum, thermodynamic properties, and pressure-temperature phase diagram of uranium dioxide*, Phys. Rev. B, Vol.88, 104107, 2013.

Wang, Y., Zhou, X., Kou, M., *Peridynamic investigation on thermal fracturing behavior of ceramic nuclear fuel pellets under power cycles*, Ceram. Int., Vol.44, p.11512-11542, 2018. https://doi.org/10.1016/j.ceramint.2018.03.214.

Wachtman J.B., Wheat M.L., Anderson H.J., and Bates J.L., *Elastic constants of single crystal UO_2 at 25° C*, J. Nucl. Mater., Vol.16, p.39-41 ,1965.

White R.J., *The development of grain-face porosity in irradiated oxide fuel*, J. Nucl. Mater., Vol.325, p.61-77, 2004.

White R.J., Tucker M.O., *A new fission-gas release model*, J. Nucl. Mater., Vol.118, p.1-38, 1983.

Widom W., *Random sequential addition of hard spheres to a volume*. J. Chem. Phys., Vol.88, p.6540-6546, 1966.

William M.L., *On the stress distribution at the base of a stationary crack*, Journal of Applied Mechanics, Vol.24, p.109-114, 1957.

Williamson R.L., K.A. Gamble, D.M. Perez, S.R. Novascone, G. Pastore, *Validating the BISON fuel performance code to integral LWR experiments*, Vol.301, p.232-244, 2008.

Williamson, R.L., *Simulating Dynamic Fracture in Oxide Fuel Pellets Using Cohesive Zone Models, in: Idaho National Laboratory (United States)*. Funding organisation: DOE - NE (United States), Espoo (Finland), 2009.
http://inis.iaea.org/Search/search.aspx?orig_q=RN:40108244 (accessed June 5, 2020)

Wojtacki K., Vincent P.-G., Suquet P., Moulinec H., Boittin G., *A micromechanical model for the secondary creep of elasto-viscoplastic porous materials with two rate-sensitivity exponents: Application to a mixed oxide fuel*, International Journal of Solids and Structures, Volume 184, 2020, Pages 99-113, https://doi.org/10.1016/j.ijsolstr.2018.12.026

Yeon D. H., Huang Z.F., Elder K. R., and Thornton K., *Density-Amplitude Formulation of the Phase-Field Crystal Model for Two-Phase Coexistence in Two and Three Dimensions*. Philosophical Magazine, Vol.90 (1–4), p.237-63, 2010.
https://doi.org/10.1080/14786430903164572

Yingjun G., Zhirong L., Lilin H., Hong M., Chuanggao H., and Kui L., *Phase Field Crystal Study of Nano-Crack Growth and Branch in Materials*. Modelling and Simulation in Materials Science and Engineering Vol.24(5), 055010, 2016.
https://doi.org/10.1088/0965-0393/24/5/055010.

Yu J., Devanathan R., and Weber W.J., *First-principles study of defects and phase transition in UO_2*, J. Phys.: Condens. Matter., Vol.21, 435401, 2009.

Yust C.S. and McHargue C.J., *Dislocation sbstructures in deformed uranium dioxide single crystals*, Journal of Nuclear Materials, Vol.31, No.2, p.121-137, 1969.

Zhang Y., Liu X.Y., Millett P.C., Tonks M., Andersson D.A., Biner B., *Crack tip plasticity in single crystal UO_2: Atomistic simulations*, J. Nucl. Mater., Vol.430, p.96-105, 2012.

Zhang Y., Millett P.C., Tonks M.R., Bai X.M., Biner S.B., *Intergranular fracture in UO_2: deviation of traction-separation law from atomistic simulations*, INL Report INL/CON-13-29027, for Conference: GLOBAL 2013.